

## ABSTRACT

Title of dissertation:      Intercalation Chemistry of  
Tetrahedral Transition  
Metal Chalcogenides

Xiuquan Zhou  
Doctor of Philosophy, 2018

Dissertation directed by: Professor Efrain Rodriguez  
Department of Chemistry and Biochemistry

Tetrahedral transition metal chalcogenides (TTMCs), which have a common layered structural motif that could carry novel functionalities on account of the *d*-orbital filling. These metal chalcogenide layers can be held together either by pure van der Waals forces, ionic forces, or even hydrogen bonding, depending on the guest species intercalated in between the layers. Unlike transition metal dichalcogenides (TMDs), TTMCs have been less explored with respect to their synthesis, chemical reactivity, and physical properties. Structurally, TTMCs contain the transition metal in a square lattice and typically crystallize in tetragonal or orthorhombic structures on account of the square lattice. Some extraordinary properties they exhibit include superconductivity, metallic conductivity, and itinerant ferromagnetism.

In this dissertation work, we demonstrate that using kinetically controlled soft-chemistry routes, single crystal form of FeS is prepared for the first time. Furthermore, using similar route, we expand the binary TTMC family from Fe to Co, preparing the anti-PbO type of CoSe and CoS for the first time. Using these binary compounds, we demon-

strate that TTMCs can serve as excellent hosts for intercalation chemistry by preparing alkali bases intercalated iron chalcogenides. Upon intercalation, the new compounds show vastly different properties from the host, such as enhanced superconductivity or coexistence of superconductivity and long-range magnetic ordering. This work provides a framework for designing new binary and heterolyared TTMCs.

# Intercalation Chemistry of Tetrahedral Transition Metal Chalcogenides

by

Xiuquan Zhou

Dissertation submitted to the Faculty of the Graduate School of the  
University of Maryland, College Park in partial fulfillment  
of the requirements for the degree of  
Doctor of Philosophy  
2018

Advisory Committee:

Professor Efrain Rodriguez, Chair/Advisor

Professor Bryan Eichhorn

Professor Sang-Bok Lee

Professor Johnpierre Paglione

Professor Andrei Vedernikov

© Copyright by  
Xiuquan Zhou  
2018



## Dedication

To my adviser Efrain Rodriguez for introducing me to the field of Fe-based superconductors.

## Acknowledgments

I would like to thank my adviser Professor Efrain Rodriguez for guidance and support for this dissertation work. I would also like to thank my other committee members, Professors Byran Eichhorn, Andrei Vedernikov, Sang-Bok Lee, and Johnpierre Paglione for their time to review this dissertation and valuable advice to improve this work. I want to thank Dr. Jeffrey Lynn from NCNR, as this work was initiated by him asking for a deuterated LiOHFeSe sample exhibiting coexistence of superconductivity and ferromagnetism. During this quest we found the hydrothermal method was much more powerful than we originally expected, and we discovered many more compounds using it.

I want to thank the present and past members of the Rodriguez group for their assistance with experiments and pleasant company. It has been my great pleasure to work with Brandon Wilfong and Hector Vivanco. It would have been impossible to be as productive for the past years without them. To measure the physical properties of the samples presented in this work, I have received great help from Professor Paglione and his group. Here I would like to thank the Paglione group, especially Dr. Shanta Saha, for their help and collaborative works and Center for Nanophysics and Advanced Materials (CNAM) for providing essential instruments.

I would like to thank Drs. Peter Zavalij, Karen Gaskell and Sz-Chian Liou at the University of Maryland user facilities for their assistance with structural and microscopy analysis. I would also like to thank Drs. Craig Brown, Jeffrey Lynn and Jose Rodriguez for their assistance with neutron scattering. I would also like to thank Dr. Igor Pekov at Lomonosov Moscow State University for discussions with mineral ferrotchilinite. I am

grateful for the Department of Chemistry at the University of Maryland, National Science Foundation (DMR-1455118) and the Ann G. Wylie Dissertation Fellowship for providing financial support for me.

Research at the University of Maryland was supported by the NSF Career DMR-1455118, AFOSR Grant No. FA9550-14-10332, and the Gordon and Betty Moore Foundation Grant No. GBMF4419. We also acknowledge support from the Maryland Nanocenter and Center for Nanophysics and Advanced Materials. We acknowledge the support of the National Institute of Standards and Technology, U. S. Department of Commerce, in providing the neutron research facilities used in this work. The use of the Advanced Photon Source at Argonne National Laboratory was supported by the U. S. Department of Energy, Office of Science, Office of Basic Energy Sciences, under Contract No. DE-AC02-06CH11357. We thank S. Lapidus for his assistance with the 11-BM measurements. We acknowledge the University of Maryland supercomputing resources (<http://www.it.umd.edu/hpcc>) made available for conducting the research reported in this work.

# Contents

Dedication	ii
Acknowledgements	iii
List of Tables	viii
List of Figures	ix
List of Abbreviations	xii
1 Introduction	1
1.1 Fe-based Superconductors and inspirations	1
1.2 Intercalation Chemistry for Tetragonal Layered Chalcogenides	4
1.3 Objectives and Outline	8
2 Methods	12
2.1 Synthetic Methods	12
2.1.1 Bottom-up Approach	12
2.1.2 Top-down Approach	14
2.2 Characterization Methods	15
2.2.1 Powder X-ray Diffraction	15
2.2.2 Neutron Powder Diffraction	16
2.2.3 Magnetic Susceptibility	16
2.2.4 Resistivity and Heat Capacity	17
2.2.5 Thermogravimetric Analysis	18
2.2.6 Electron Microscopy	18
2.2.7 ICP-AES	18
2.2.8 Computational methods	19
3 Tetrahedral Superconducting FeS Single Crystals	20
3.1 Introduction	20
3.2 Experimental	23
3.2.1 Hydrothermal synthesis of FeS single crystals	23
3.2.2 X-ray diffraction and thermal stability analysis	24
3.2.3 Magnetic susceptibility, electrical transport and heat capacity	25
3.3 Results: Synthesis, thermal stability and structural characterization	26

3.3.1	Single crystal preparation by reductive deintercalation . . . . .	26
3.3.2	X-ray diffraction and crystal structure . . . . .	28
3.3.3	Thermal stability of FeS single crystals . . . . .	30
3.4	Results: Physical properties . . . . .	34
3.4.1	Magnetic susceptibility . . . . .	34
3.4.2	Heat capacity . . . . .	36
3.4.3	Magnetoelectric transport . . . . .	37
3.5	Discussion . . . . .	41
3.5.1	Strongly anisotropic electronic properties . . . . .	41
3.5.2	True ground and normal state properties of FeS . . . . .	43
3.5.3	Structural trends concerning $T_c$ . . . . .	44
3.6	Conclusions . . . . .	46
4	Metastable Layered Cobalt Chalcogenides from Topochemical Deintercalation . . . . .	52
4.1	Introduction . . . . .	52
4.2	Experimental . . . . .	55
4.2.1	Sample synthesis . . . . .	55
4.2.2	Characterization methods . . . . .	56
4.2.3	Computational methods . . . . .	57
4.3	Results . . . . .	58
4.3.1	Topochemical De-intercalation . . . . .	58
4.3.2	Crystallography, chemical composition, and thermal stability . . . . .	63
4.3.3	Magnetic properties . . . . .	67
4.3.4	Electrical Resistivity . . . . .	73
4.4	Discussion . . . . .	75
4.4.1	De-intercalation chemistry of late transition metal chalcogenides . . . . .	75
4.4.2	Intercalation chemistry of late transition metal chalcogenides . . . . .	76
4.4.3	Relationship to FeSe and DFT Predicted Stability . . . . .	79
4.5	Conclusions . . . . .	86
5	The Preparation and Phase Diagrams of $(\text{}^7\text{Li}_{1-x}\text{Fe}_x\text{OD})\text{FeSe}$ and $(\text{Li}_{1-x}\text{Fe}_x\text{OH})\text{FeSe}$ Superconductors . . . . .	88
5.1	Introduction . . . . .	88
5.2	Experimental . . . . .	90
5.2.1	Sample preparation . . . . .	90
5.2.2	Laboratory and synchrotron X-ray diffraction measurements . . . . .	92
5.2.3	Magnetization measurements . . . . .	93
5.2.4	Neutron powder diffraction measurements . . . . .	93
5.3	Results . . . . .	94
5.3.1	Crystallography and phase diagram . . . . .	94
5.3.2	Magnetization results and the phase diagrams . . . . .	97
5.3.3	Neutron results . . . . .	100
5.4	Discussion . . . . .	101
5.4.1	Relation between structural parameters and superconductivity . . . . .	101
5.4.2	Relation between magnetism and superconductivity . . . . .	102

5.5	Conclusions . . . . .	106
6	Superconductivity and Magnetism in Iron Sulfides Intercalated by Metal Hydroxides . . . . .	107
6.1	Introduction . . . . .	107
6.2	Experimental . . . . .	108
6.2.1	Synthesis . . . . .	108
6.2.2	Characterizations . . . . .	111
6.3	Results and discussions . . . . .	112
6.3.1	Li-intercalated phases . . . . .	112
6.3.2	Na-intercalated phases . . . . .	119
6.3.3	K-intercalated phases . . . . .	129
6.4	Conclusions . . . . .	131
7	Conclusions and Future Work . . . . .	132
7.1	Conclusions . . . . .	132
7.2	Future Work . . . . .	134
7.2.1	Mechanisms of the Hydrothermal Process . . . . .	134
7.2.2	From the Bulk to Nanosheets . . . . .	136
7.2.3	Heterolayered Structures by Design . . . . .	137
7.2.4	Pressure Studies . . . . .	139
	Bibliography . . . . .	141

## List of Tables

3.1	Structural parameters for ground single crystals of $K_xFe_{2-y}S_2$ and FeS . . .	31
4.1	Structural parameters for ground single crystals of $KCo_2Se_2$ and CoSe . . .	63
4.2	Elemental analysis of newly synthesized anti-PbO type CoSe and CoS . . .	64
4.3	Structural parameters for ground polycrystalline material of $Co_9Se_8$ . . . .	78
5.1	Rietveld refinement of synchrotron PXRD data collected at 7 K for a superconducting sample of $(^7Li_{1-x}Fe_xOD)FeSe$ and a non-superconducting sample . . . . .	95
6.1	List of $Li_{1-x}Fe_xOH)FeS$ samples. . . . .	118
6.2	Lattice and structural parameters obtained from Rietveld refinement with synchrotron PXRD data collected at room temperature for $(Li_{1-x}Fe_xOH)FeS$	120

## List of Figures

1.1	Crystal structures of three layered iron selenides: $K_{0.8}Fe_{1.6}Se_2$ (left) FeSe (centre) and $(Li_{1-x}Fe_xOH)FeSe$ (right) . . . . .	2
1.2	Band structure of FeSe showing the high-symmetry path for M- $\Gamma$ -X . . . . .	5
2.1	Molecules of (a) $Fe_4S_4(OH_2)_4$ and (b) $[Fe_4S_4(SH_4)_4]_4^-$ clusters . . . . .	14
3.1	Rietveld refinement with XRD powder diffraction . . . . .	22
3.2	Magnetic susceptibility of $K_xFe_{2-y}S_2$ starting material . . . . .	27
3.3	Temperature correlations between XRD patterns and DSC measurements . . . . .	28
3.4	Rietveld refinement of XRD pattern of powder FeS . . . . .	29
3.5	Temperature-dependent XRD patterns of single crystal FeS orientated along the 00l direction . . . . .	32
3.6	XRD patterns of ground FeS crystals before and after DSC measurement . . . . .	33
3.7	Elemental analysis of surface of FeS single crystal . . . . .	33
3.8	Magnetic susceptibility of an FeS single crystal . . . . .	35
3.9	Low temperature specific heat of single crystal FeS . . . . .	37
3.10	Electrical resistivity measurements of different crystals of FeS . . . . .	38
3.11	Anisotropy electrical resistivity of single crystalline FeS . . . . .	39
3.12	Constant temperature scans of magnetoresistance (MR) of FeS as a function of field angle . . . . .	48
3.13	Superconducting transition of FeS single crystal as a function of magnetic field applied along different angles . . . . .	49
3.14	Angular dependence of the superconducting upper critical field $H_{c2}$ at 1.8 K . . . . .	50
3.15	Applied pressure dependence of the superconducting transition temperature of an FeS crystal . . . . .	51
4.1	Reaction schemes for the manipulation of cobalt chalcogenides . . . . .	53
4.2	Diagram for experimental set-up of a hydrogen trap during the de-intercalation reaction of $K_{1-x}Co_{2-y}Se_2$ . . . . .	59
4.3	Volume of hydrogen generated during a de-intercalation reaction of $KCo_2Se_2$ . . . . .	61
4.4	Powder X-ray and neutron diffraction patterns of $KCo_2Se_2$ and CoSe . . . . .	62
4.5	Powder X-ray diffraction patterns of $KCo_2S_2$ and CoS . . . . .	65
4.6	Temperature evolution of the x-ray powder diffraction of ground single crystals of CoSe . . . . .	66
4.7	Magnetic susceptibility of $KCo_2Se_2$ and CoSe . . . . .	68
4.8	Isothermal magnetization vs. applied field $H$ for $KCo_2Se_2$ and CoSe at 1.8 K . . . . .	69

4.9	Isothermal magnetization vs. applied field $H$ for CoSe at $T = 2$ K, 60 K, and 150 K . . . . .	71
4.10	Magnetic susceptibility of CoS . . . . .	72
4.11	Temperature dependent electrical resistivity of CoSe measured on a single crystal . . . . .	73
4.12	Temperature dependent electrical resistivity of $\text{KCo}_2\text{Se}_2$ measured on a single crystal . . . . .	74
4.13	Powder X-ray diffraction patterns of ground polycrystalline $\text{Li}(\text{C}_2\text{H}_8\text{N}_2)\text{CoSe}$ collected at room temperature . . . . .	77
4.14	Rietveld refinements with x-ray powder diffraction on ground polycrystalline material of $\text{Co}_9\text{Se}_8$ collected at room temperature . . . . .	78
4.15	The spin-polarized electronic density of states (DOS) of FeSe and CoSe . . . . .	80
4.16	Band structure along three different directions and the corresponding partial DOS of $3d$ states for FeSe and CoSe . . . . .	81
4.17	Density functional theory (DFT) calculations of FeS and CoS . . . . .	82
4.18	Density functional theory (DFT) calculations of NiSe and NiS . . . . .	83
4.19	Fermi surface plots on the $\Gamma$ -M-X plane for a) FeSe, b) CoSe, c) FeS and d) CoS. . . . .	84
4.20	Band structure and partial DOS of $3d$ orbitals of FeS and CoS . . . . .	85
5.1	X-ray and neutron powder diffraction for non-superconducting ( ${}^7\text{Li}_{1-x}\text{Fe}_x\text{OD}$ )FeSe with $x = 0.166$ . . . . .	94
5.2	Synchrotron powder X-ray diffraction patterns for a superconducting single crystal sample of $(\text{Li}_{1-x}\text{Fe}_x\text{OD})\text{FeSe}$ . . . . .	96
5.3	Magnetic susceptibility of samples prepared by powder routes and single crystal routes of deuterioxide series $(\text{Li}_{1-x}\text{Fe}_x\text{OD})\text{FeSe}$ . . . . .	97
5.4	Superconducting phase diagrams of $(\text{Li}_{1-x}\text{Fe}_x\text{OH})\text{FeSe}$ as comparison for that of single crystal ( ${}^7\text{Li}_{1-x}\text{Fe}_x\text{OD}$ )FeSe and powder samples and $(\text{Li}_{1-x}\text{Fe}_x\text{OD})\text{FeSe}$ . . . . .	98
5.5	The NPD pattern of non-superconducting phase of ( ${}^7\text{Li}_{1-x}\text{Fe}_x\text{OD}$ )FeSe at 150 K and 4 K . . . . .	100
5.6	Comparison between the powder XRD patterns and magnetic susceptibility for $\text{Fe}_3\text{O}_4$ and $(\text{Li}_{1-x}\text{Fe}_x\text{OH})\text{FeSe}$ . . . . .	103
6.1	Synthetic scheme for the intercalation chemistry of FeS with metal hydroxides and $\text{K}^+$ cations via hydrothermal preparations. . . . .	109
6.2	Temperature dependent electrical resistivity of superconducting $(\text{Li}_{1-x}\text{Fe}_x\text{OH})\text{FeS}$ 113	
6.3	Magnetic susceptibility measurements of superconducting $(\text{Li}_{1-x}\text{Fe}_x\text{OH})\text{FeS}$ 113	
6.4	Specific heat measurements of (a) LiOH-intercalate FeS and (b) <i>inc</i> -Natochilinite. . . . .	114
6.5	Field dependence of electrical resistance for a superconducting $(\text{Li}_{1-x}\text{Fe}_x\text{OH})\text{FeS}$ sample ( $T_c = 3.5$ K) at 1.8 K . . . . .	115
6.6	Temperature dependence of electrical resistivity for superconducting $(\text{Li}_{1-x}\text{Fe}_x\text{OH})\text{FeS}$ samples . . . . .	116
6.7	Synchrotron XRD patterns of $(\text{Li}_{1-x}\text{Fe}_x\text{OH})\text{FeS}$ . . . . .	117

6.8	XRD patterns of mixtures of disordered NaOH intercalated FeS and tetragonal FeS . . . . .	121
6.9	Magnetic susceptibility of <i>inc</i> -Na-tochilinite, $[(\text{Na}_{1-x}\text{Fe}_x)(\text{OH})_2]$ . . . . .	122
6.10	Temperature dependent magnetic susceptibility measurement of <i>inc</i> -Na-tochilinite with tetragonal FeS as a major phase . . . . .	123
6.11	Magnetization versus field measurements of <i>inc</i> -Na-tochilinite . . . . .	124
6.12	Electrical resistance of <i>inc</i> -Na-tochilinite . . . . .	125
6.13	PXRD patterns of Na-tochilinite and $\text{K}_x\text{Fe}_{2-y}\text{S}_2$ . . . . .	126
6.14	Electron diffraction patterns of FeS and Na-tochilinite . . . . .	127
6.15	Magnetic susceptibility measurements of Na-tochilinite and $\text{K}_x\text{Fe}_{2-y}\text{S}_2$ . . . . .	128
7.1	XRD pattern of a crystalline tetragonal FeS sample hydrothermally prepared under basic conditions using ferrocene as the Fe source. . . . .	135
7.2	Atomic force microscopy image of a thinlayered CoSe sheet deposited on a mica substrate . . . . .	137

## List of Abbreviations

122-type	
ThCr <sub>2</sub> Si <sub>2</sub> -type 2D	two-dimensional
AFM	antiferromagnetic
APS	Advanced Photon Source
ARPES	angle-resolved photoemission spectroscopy
BCS	Bardeen-Cooper-Schrieffer
<i>Ch</i>	chalcogenide
COHP	crystal orbital Hamilton populations
CNAM	the Center for Nanophysics and Advanced Materials
DOS	density of state
DSC	differential scanning calorimetry
EDA	ethylenediamine
EDS	energy dispersive X-ray spectroscopy
DFT	density functional theory
FC	field-cooled
FM	ferromagnetic
GGA	generalized gradient approximation
HMDA	hexamethylenediamine
ICP-AES	inductively coupled plasma atomic emission spectroscopy
ICSD	Inorganic Crystallographic Structural Database
LOBSTER	Local-Orbital Basis Suite Towards Electronic-Structure Reconstruction
MPMS	magnetic properties measurement system
NCNR	NIST Center for Neutron Research
NPD	neutron powder diffraction
PAW	projector augmented wave
<i>Pn</i>	pnictide
PPMS	physical property measurement system
PSD	position sensitive detector
SANS	small angle neutron scattering
SEM	scanning electron microscope
STO	SrTiO <sub>3</sub>
SQUID	superconducting quantum interference device
$T_c$	Critical Temperature
TEM	transmission electron microscope
TGA	thermogravimetric analysis
TMD	transition metal dichalcogenide
TTMC	tetragonal transition metal chalcogenide
VASP	the Vienna Ab-initio Simulation Package
XRD	X-ray diffraction
ZFC	zero field-cooled

## Chapter 1: Introduction

### 1.1 Fe-based Superconductors and inspirations

Ever since Heike Kamerlingh Onnes discovered superconductivity, which describes a phenomenon of zero electrical resistance in materials cooled below a critical temperature ( $T_c$ ), in 1911,<sup>1</sup> the term has been associated with cryogenic physics. Indeed, superconductivity was a side product of the 1913 Nobel laureate's epic quest to achieve ultra-low temperature in order to liquefy helium. The  $T_c$  of the first known superconductor, mercury, is merely 4.2 K.<sup>1</sup> Despite the low  $T_c$ 's of early superconductors, the concept of superconductivity has held great potential to revolutionize the entire energy industry since its inception.<sup>2-5</sup> For the past 100 years, the excitement for searching high-temperature superconductors has never diminished.

There have been several milestones in the field of superconductivity since Onnes's discovery, such as the BCS theory<sup>6</sup> and the high- $T_c$  cuprate superconductors,<sup>7</sup> which both received the Nobel prize. Hosono *et al.*'s discovery of the high- $T_c$  Fe-based superconductors,  $\text{LaFeAsO}_{1-x}\text{F}_x$  ( $T_c$  up to 43 K), in 2008 marked the greatest breakthrough since the discovery of the cuprate superconductors.<sup>8,9</sup> In the family of iron pnictide (FePn) superconductors, the common crystal structure assumes a two-dimensional (2D) layered motif consisting of alternating anionic (FePn)<sup>-</sup> layers and cationic layers, such as (LaO)<sup>+</sup> and

Ba<sup>2+</sup>, held by ionic interactions. In addition to unconventional superconductivity, the FePn superconductors are fascinating for exhibiting a close relationship between magnetism and superconductivity. In the FePn systems, superconductivity emerges after suppression of the parent antiferromagnetic (AFM) phase.<sup>10-12</sup>

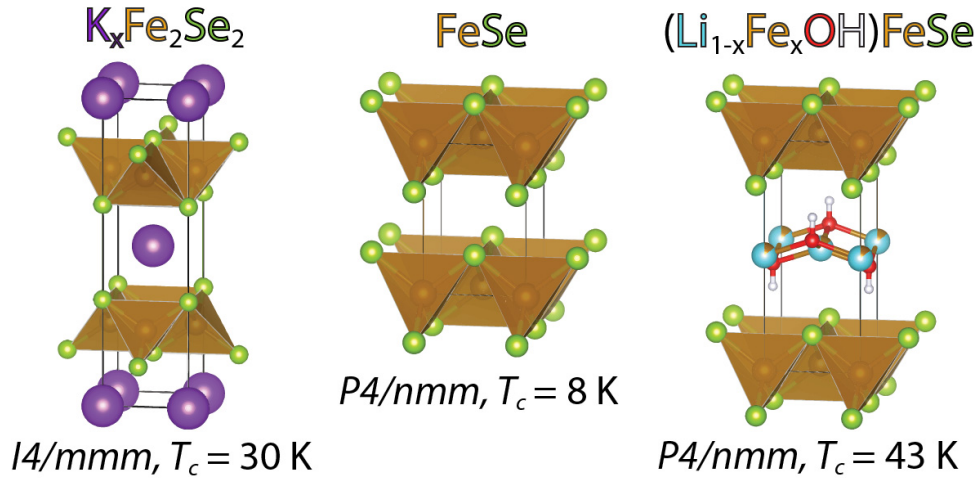


Figure 1.1: Crystal structures of three layered iron selenides:  $K_{0.8}Fe_{1.6}Se_2$  (left) FeSe (centre) and  $(Li_{1-x}Fe_xOH)FeSe$  (right)

Following the landmark discovery of FePn superconductors lead by Hosono *et al.*<sup>8,9</sup>, superconductivity was discovered in another layer Fe-based compound, FeSe, and soon it attracted incredible amount of attention.<sup>13-18</sup> Unlike FeAs, which is not a superconductor itself, the layered  $\beta$ -FeSe exhibits a  $T_c$  of 8 K under ambient conditions, and its  $T_c$  can be further raised to 37 K by externally applied pressure.<sup>19</sup> The tetragonal anti-PbO type ( $P4/nmm$ )  $\beta$ -FeSe (Fig. 1.1 center) consists of sheets of edge-sharing FeSe<sub>4</sub> tetrahedra held together by van der Waals interactions. Because of weak interlayer interactions in FeSe, its van der Waals layers are more prone to chemical manipulations compared to much more strongly bound ionic layers in the iron pnictides. Hence FeSe is an ideal host for intercalation chemistry.

Indeed, both ionic and molecule species have been inserted into FeSe layers, and more interestingly up on intercalation, the  $T_c$  of FeSe could be significantly enhanced up to 42-44 K.<sup>20-26</sup> After insertion of ions or molecules, the products usually crystallize into two types of structures: the  $\text{ThCr}_2\text{Si}_2$ -type (122-type) body-centered tetragonal ( $I4/mmm$ ) structure, such as  $\text{K}_x\text{Fe}_{1-y}\text{Se}_2$  (Fig. 1.1 left) or the primitive tetragonal ( $P4/nmm$ ) structure, such as  $(\text{Li}_{1-x}\text{Fe}_x\text{OH})\text{FeSe}$  (Fig. 1.1 right), respectively. Besides serving as a host for intercalation, FeSe can be broken down to single layers to fabricate heterolayered structures. Ge *et al.*<sup>27</sup> have achieved an astonishingly high  $T_c$  above 100 K for FeSe monolayers grown on  $\text{SrTiO}_3$  (STO) substrates. This has a great implication that the Fe-based superconductors can break the liquid nitrogen temperature threshold. However, it is still unclear why the  $T_c$  is significantly enhanced for monolayer FeSe. It is suggested that the heterolayer interface between FeSe and STO results in significant amount of strain to the FeSe monolayer, which is essential to the high  $T_c$  of monolayer FeSe.<sup>27-29</sup>

All these results indicate that it is possible to further improve the  $T_c$  of FeSe by forming heterolayered structures with appropriate spacers. There are a variety of layered compounds that can be used to fabricate heterolayered structure with FeSe, such as brucite-type  $(\text{Mg}(\text{OH})_2)$  layered hydroxide and transition metal dichalcogenides (TMDs). These adduct layers can be insulating, semiconducting, metallic or superconducting, and they can even be magnetic, such as  $\text{Ni}(\text{OH})_2$ .<sup>30</sup> Therefore, besides discovering new superconductors, investigating the emergent properties of the heterolayered structures stacked from layers with distinct different behaviors can reveal recipes for designing novel functional materials. This is the greatest inspiration for us to explore heterolayered structures of iron-chalcogenides. Since intercalation chemistry remains the most effective means to

achieve this, we will introduce it in the next section.

## 1.2 Intercalation Chemistry for Tetragonal Layered Chalcogenides

Intercalation chemistry has been a longstanding technique for the manipulation of layered materials such as graphite and chalcogenides.<sup>31–33</sup> Like transition metal dichalcogenides (TMDs), layered tetragonal FeCh can be hosts for intercalation chemistry due to their van der Waals gaps. Ever since Geballe and coworkers<sup>34–37</sup> raised  $T_c$  of TMDs by inserting various bases, intercalation has been an effective method for studying superconductivity and related phenomena in layered materials. Here, we distinguish the intercalation chemistry from the solid-state methods used for 122-type TTMCs. The 122-type tetragonal transition metal chalcogenides (TTMCs) are usually formed from melts, and the formation of  $K_xFe_{1-y}Se_2$  with a large number of Fe vacancies coexists with several impurity phases.<sup>22,38,39</sup> Therefore, our discussion will be focused on intercalation chemistry via *chimie douce* or soft chemical methods, where no drastic change occurs in the host materials.

Clarke *et al.*<sup>20,23</sup> successfully intercalated alkali metals ( $Li^+$ ,  $Na^+$  and  $K^+$ ) into pre-made FeSe powders using solutions of these metals in liquid ammonia. Interestingly, not only are the alkali metal cations inserted between the layers but also ammonia and metal amide moieties. Like  $A_xFe_{1-y}Se_2$ , these new compounds also assume the  $ThCr_2Si_2$ -type structure. However, unlike in the  $A_xFe_{1-y}Se_2$  phases prepared by high-temperature techniques, in the  $Li_{0.6}(ND_2)_{0.2}(ND_3)_{0.8}Fe_2Se_2$  superconductors the amine occupies the A site while alkali cations the interstitial sites. Most interesting of all, upon intercalation,

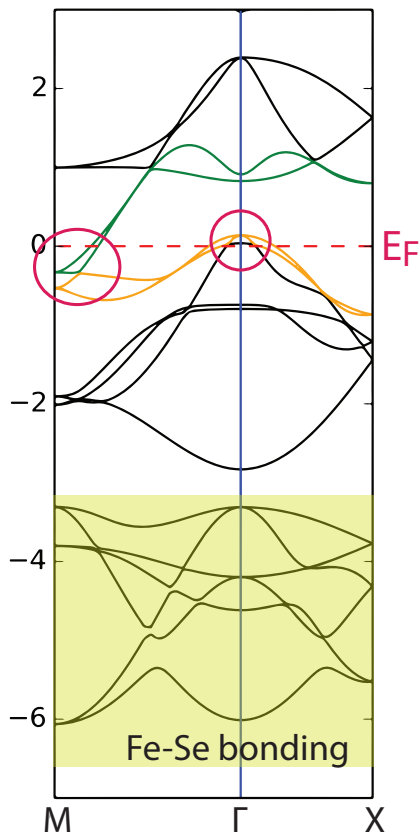


Figure 1.2: Band structure of FeSe showing the high-symmetry path for M- $\Gamma$ -X. The  $\Gamma$ -point corresponds to the most antibonding configuration, and the M-point to the most bonding one.

the  $T_c$  of FeSe increased from 8 K<sup>13</sup> to 42-44 K. This drastic rise in the  $T_c$  has been attributed to partial electron doping of the FeSe layer,<sup>23,40?,41</sup> which is key towards filling in the M-points of the band diagram (Fig. 1.2). Using a similar liquid ammonia route, alkaline earth metals can also be intercalated into FeSe, despite achieving a slightly lower  $T_c$  than the alkali metals. For Sr and Ba intercalation, the  $T_c$  is found to be 35 K<sup>42,43</sup> and 36 K<sup>44</sup>, respectively. Nonetheless, the compounds are quite remarkable considering that they cannot be prepared by conventional solid-state methods, such as direct elemental reaction at high temperature.

Other than liquid ammonia, organic amines such as traditional coordination ligands can also be utilized for cation insertion into FeSe.<sup>45-48</sup> Ethylenediamine (EDA) is the most commonly used amine for this purpose, and Li- and Na-EDA intercalated FeSe also can raise  $T_c$  to 42-44 K.<sup>45,48</sup> Even higher-order amines, such as hexamethylenediamine (HMDA) can co-intercalate along with  $\text{Li}^+$  ions to form large spacers between FeSe layers, increasing the interlayer distance from 5.52 Å<sup>16</sup> up to 16.23 Å.<sup>46</sup> Although the as-synthesized product only raised the  $T_c$  of FeSe to 38 K, post-synthetic annealing can further enhance the  $T_c$  to 41 K.<sup>49</sup> Other than linear-chained amines, aromatic amines such as pyridine, can also serve as a solvent for alkali metal intercalation, and the  $T_c$  can be enhanced up to 45 K.<sup>47</sup> Interestingly, although the distance between FeSe layers are increased to about 10.37 Å to 16.23 Å by varying the amine adducts, the maximum enhanced  $T_c$ 's are fairly close. It is suggested that the optimal electron doping is more important than interlayer distances once a certain spacer threshold is met.<sup>50</sup>

In addition to polar basic solvents such as liquid ammonia and organic amines, water can also be utilized as a solvent for the preparation of intercalated TTMCs. Although not intuitively desirable for the intercalation of chalcogenides due to possible decomposition and oxidation in water, metal chalcogenides can be stabilized as long as the aqueous reactions are carried out under strongly basic conditions.<sup>51</sup> Utilizing an excess of LiOH under hydrothermal conditions, Lu *et al.*<sup>24</sup> managed to intercalate FeSe with neutral Li hydroxide layers. Remarkably, the  $T_c$  of FeSe was raised to 42 K, comparable to the intercalation of  $\text{Li}^+$  cations in liquid ammonia. Extensive high-resolution neutron and synchrotron X-ray diffraction studies later revealed that the correct stoichiometry of the hydroxide-intercalated superconductor is  $(\text{Li}_{1-x}\text{Fe}_x\text{OH})\text{FeSe}$ . The hydrogen position was

also determined by the neutron studies, which support hydrogen bonding as the mechanism holding these new phases together.<sup>26,52-54</sup> Furthermore, the  $\text{Fe}^{2+}$  cations substituting for  $\text{Li}^+$  in the hydroxide layer is crucial to the enhanced superconductivity as it charge dopes the FeSe layer by approximately 15 to 18 % per formula unit, consistent with intercalation of alkali cations in liquid ammonia and amines.

In addition to its high- $T_c$  superconductivity,  $(\text{Li}_{1-x}\text{Fe}_x\text{OH})\text{FeSe}$  attracted significant attention for its magnetic properties as well. Lu *et al.*<sup>52</sup> reported coexistence of antiferromagnetism and superconductivity from nuclear magnetic resonance (NMR) studies, although no long-range magnetic ordering was observed in their neutron diffraction data. Pachmayr *et al.*<sup>25</sup> reported coexistence of ferromagnetic ordering and superconductivity in  $(\text{Li}_{1-x}\text{Fe}_x\text{OH})\text{FeSe}$ , alleging that this should lead to a spontaneous vortex lattice from the proximity of the two types of layers. The vortex lattice was observed later by small angle neutron scattering (SANS) results by Lynn *et al.*,<sup>54</sup> where a ferromagnetic ordering below 12.5 K was observed albeit for a small applied field. Although long-range magnetic ordering in  $(\text{Li}_{1-x}\text{Fe}_x\text{OH})\text{FeSe}$  has yet to be found, it is suggested that the magnetic anomalies arise from the  $\text{Fe}^{2+}$  in LiOH layer, which may be tunable by synthetic conditions.<sup>26,53,55,56</sup>

Similar to FeSe, FeS can also act as a host for guest species such as alkali cations with non-aqueous solvents. Guo *et al.*<sup>57</sup> recently intercalated FeS with  $\text{K}^+$  in EDA. Unlike its Se analogues, however, the EDA-intercalated sulfide is not superconducting. Rather it is a semiconductor exhibiting weak ferrimagnetism below 50 K. For intercalation under aqueous conditions, only LiOH intercalated FeS was reported prior to our work.<sup>58-60</sup>  $(\text{Li}_{1-x}\text{Fe}_x\text{OH})\text{FeS}$  can be prepared using a similar route for its Se analogue. However, un-

like its selenide counterpart or pure FeS, it has been reported to be non-superconducting by several groups.<sup>58–60</sup> Notwithstanding these earlier works, it is possible that a superconducting phase diagram exists for the  $(\text{Li}_{1-x}\text{Fe}_x\text{OH})\text{FeS}$  system, like its selenide analogue, and optimal electron doping is required to induce superconductivity in this system.

Unfortunately, the intercalation chemistry for binary TTMCs ends with FeSe and FeS, although the anti-PbO type  $\text{Fe}_{1+x}\text{Te}$  can be another candidate. However, its ability for chemical manipulation may be significantly hindered by excess Fe in the lattice, as they cannot be completely removed.<sup>61,62</sup> Hence, there is no report for successfully inserting an adduct into the binary FeTe system. Outside the iron family, there was no reported binary TTMC of other transition metal prior to our work.

### 1.3 Objectives and Outline

In order to provide more combinations for TTMC-based heterolayered structures, it is necessary to explore other anti-PbO type layered chalcogenides in addition to FeSe. The tetragonal structured FeS, a lighter analogue to the superconducting FeSe, has recently been found to be a superconductor below 5 K.<sup>63</sup> The new addition of FeS to the FeCh based superconductors has brought great potentials to this superconducting family, as the same intercalation chemistry that has been applied to FeSe are likely to be successful with FeS, due to their structural similarities. Hence, the first objective was to optimize the synthetic pathway for pristine FeS samples, especially in single crystal form, and study its chemical stability and physical properties (Chapter 3). Furthermore, we hope to use a similar modified synthetic route to explore the possibility of obtaining binary

TTMCs of other transition metals (Chapter 4). Any new addition to the TTMC family will significantly broaden the types of heterolayered structures. We will then synthesize new heterolayered structures and investigate their properties based on existing TTMC precursors (Chapter 5 and 6). This section provides an overview for each chapter.

In Chapter 2, we introduce the synthetic and characterization methods used throughout the entire dissertation work.

In Chapter 3, we describe the novel synthesis of single crystals of tetragonal iron sulfide (FeS) through hydrothermal de-intercalation of  $K_xFe_{2-y}S_2$  single crystals. The silver, plate-like product is highly crystalline with a superconducting transition temperature ( $T_c^{onset}$ ) of 3.5 K found from electrical resistivity measurements. Further characterizations of the physical properties of FeS are described therein.

In Chapter 4, we describe a general strategy to synthesize metastable layered materials via topochemical de-intercalation of thermodynamically stable phases. Through kinetic control of the de-intercalation reaction, we have prepared two hypothesized metastable compounds, CoSe and CoS, with the anti-PbO type structure from the starting compounds  $KCo_2Se_2$  and  $KCo_2S_2$ , respectively. Thermal stability, crystal structure from X-ray and neutron diffraction, magnetic susceptibility, magnetization, and electrical resistivity are studied for these new layered chalcogenides. Both CoSe and CoS are found to be weak itinerant ferromagnets with Curie temperatures close to 10 K. Due to the weak van der Waals forces between the layers, CoSe is found to be a suitable host for further intercalation of guest species such as Li-ethylenediamine. From first-principles calculations, we explain why the Co chalcogenides are ferromagnets instead of superconductors as in their iron analogues. Bonding analysis of the calculated electronic density of states both

explains their phase stability and predicts the limits of our de-intercalation technique. Our results have broad implications for the rational design of new two-dimensional building blocks for functional materials.

In Chapter 5, We describe the phase diagram for the deuterated superconducting system ( ${}^7\text{Li}_{1-x}\text{Fe}_x\text{OD}$ )FeSe and contrast it with that of  $(\text{Li}_{1-x}\text{Fe}_x\text{OH})\text{FeSe}$  both in single crystal and powder forms. Samples were prepared via hydrothermal methods and characterized with laboratory and synchrotron X-ray diffraction, high-resolution neutron powder diffraction (NPD), and high intensity NPD. We find a correlation between the tetragonality of the unit cell parameters and the critical temperature,  $T_c$ , which is indicative of the effects of charge doping on the lattice and formation of iron vacancies in the FeSe layer. We observe no appreciable isotope effect on the maximum  $T_c$  in substituting H by D. The NPD measurements definitively rule out an antiferromagnetic ordering in the non-superconducting  $(\text{Li}_{1-x}\text{Fe}_x\text{OD})\text{FeSe}$  samples below 120 K, which has been reported in non-superconducting  $(\text{Li}_{1-x}\text{Fe}_x\text{OH})\text{FeSe}$ .<sup>1</sup> A likely explanation for the observed antiferromagnetic transition in  $(\text{Li}_{1-x}\text{Fe}_x\text{OH})\text{FeSe}$  samples is the formation of impurities during their preparation such as  $\text{Fe}_3\text{O}_4$  and  $\text{Li}_x\text{FeO}_2$ , which express a charge ordering transition known as the Verwey transition near 120 K. The concentration of these oxide impurities is found to be dependent on the concentration of the lithium hydroxide reagent and the use of  $\text{H}_2\text{O}$  vs.  $\text{D}_2\text{O}$  as the solvent during synthesis. We also describe the reaction conditions that lead to some of our superconducting samples to exhibit ferromagnetism below  $T_c$ .

In Chapter 6, we present a new family of iron-based superconductors. A metastable form of FeS known as the mineral mackinawite forms two-dimensional sheets that can be readily intercalated by various cationic guest species. Under hydrothermal conditions

using alkali metal hydroxides, we prepare three different cation and metal hydroxide-intercalated FeS phases including  $(\text{Li}_{1-x}\text{Fe}_x\text{OH})\text{FeS}$ ,  $[(\text{Na}_{1-x}\text{Fe}_x)(\text{OH})_2]\text{FeS}$ , and  $\text{K}_x\text{Fe}_{2-y}\text{S}_2$ . Upon successful intercalation of the FeS layer, the superconducting critical temperature  $T_c$  of mackinawite is enhanced from 5 K to 8 K for the  $(\text{Li}_{1-x}\text{Fe}_x\text{OH})^{\delta+}$  intercalate. Layered heterostructures of  $[(\text{Na}_{1-x}\text{Fe}_x)(\text{OH})_2]\text{FeS}$  resemble the natural mineral tochilinite, which contains an iron square lattice interleaved with a hexagonal hydroxide lattice. While heterostructured  $[(\text{Na}_{1-x}\text{Fe}_x)(\text{OH})_2]\text{FeS}$  displays long-range magnetic ordering near 15 K,  $\text{K}_x\text{Fe}_{2-y}\text{S}_2$  displays short range antiferromagnetism.

In Chapter 7, we summarize the overall work presented in this dissertation, and introduce possible future directions based on the outcome of this work.

## Chapter 2: Methods

### 2.1 Synthetic Methods

Here we will only discuss generic approaches to tetragonal transition metal chalcogenides (TTMCs), including both simple binaries and heterolayered structures. More specific synthetic details are described in experimental sections of respective chapters.

#### 2.1.1 Bottom-up Approach

Both simple binary and heterolayered iron chalcogenides can be prepared using a hydrothermal based bottom-up approach with some variation of synthetic conditions. For a typical reaction, Fe powder, a chalcogen source (*e.g.* selenourea, thiourea,  $\text{Li}_2\text{S}$ ), and a base, such as  $\text{LiOH}\cdot\text{H}_2\text{O}$  and NaOH, will be mixed with water in a stainless steel autoclave, and heated to 120-200 °C for 3-8 d. For the synthesis of LiOH intercalated  $\text{FeCh}$ , usually a large amount of  $\text{LiOH}\cdot\text{H}_2\text{O}$  was used to form a saturated solution, which ensures complete intercalation of LiOH. While for the synthesis of simple binary  $\text{FeS}$ , only a small amount of NaOH was used to avoid the intercalation of NaOH.

Synthetic variables such as reaction time and temperature may have a more significant impact on the LiOH intercalated  $\text{FeCh}$ , while they have much less effect on the prod-

ucts of binary FeS. The reason is that there are two compositional variables,  $x$  and  $y$ , in the LiOH intercalated systems,  $(\text{Li}_{1-x}\text{Fe}_x\text{OH})\text{Fe}_{1-y}\text{Ch}$ , while the composition of FeS can be considered a constant. We have found that the variables  $x$  and  $y$  in  $(\text{Li}_{1-x}\text{Fe}_x\text{OH})\text{Fe}_{1-y}\text{Ch}$  affected the lattice constants and  $T_c$  of the products and they were correlated to reaction time and temperature. Therefore, we were able to obtain a superconducting phase diagram of  $(\text{Li}_{1-x}\text{Fe}_x\text{OH})\text{Fe}_{1-y}\text{Ch}$  by fine tuning these synthetic variables. Through such a comprehensive study, we have gained better understanding for both the chemical process and the physical properties of these systems.

Although a lot of efforts have been devoted to tuning the synthetic conditions, the microscopic chemical mechanism remains unclear due to the black-box nature of the hydrothermal process. Notwithstanding great difficulties, we have found that the presence of a strong base and Fe powders were critical. When an  $\text{Fe}^{2+}$  salt was used, the precipitation of  $\text{Fe}(\text{OH})_2$  occurred immediately upon mixing, and the final product was mainly iron oxides.

One of the crucial processes for the synthesis of TTMCs is the oxidation of Fe powder to  $\text{Fe}^{2+}$ . According to the Pourbaix diagram for Fe, under highly basic conditions, neutral Fe is not stable and will be oxidized, which is also known as caustic corrosion.<sup>51,64</sup> Under highly basic conditions, the dominant form of S and Se in aqueous solutions are  $\text{HS}^-$  and  $\text{HSe}^-$ , respectively. Fig 2.1a and 2.1b illustrate two forms of Fe- $\text{HS}^-$  clusters in aqueous and nonaqueous solutions, respectively.<sup>65</sup> It is reasonable to assume similar tetrahedrally coordinated Fe clusters are the building blocks of the extended FeCh layers via a condensation process. This may be the reason that the as-recovered products via such hydrothermal route always yield tetrahedrally coordinated  $\text{Fe}_4\text{Ch}_4$  layers instead of

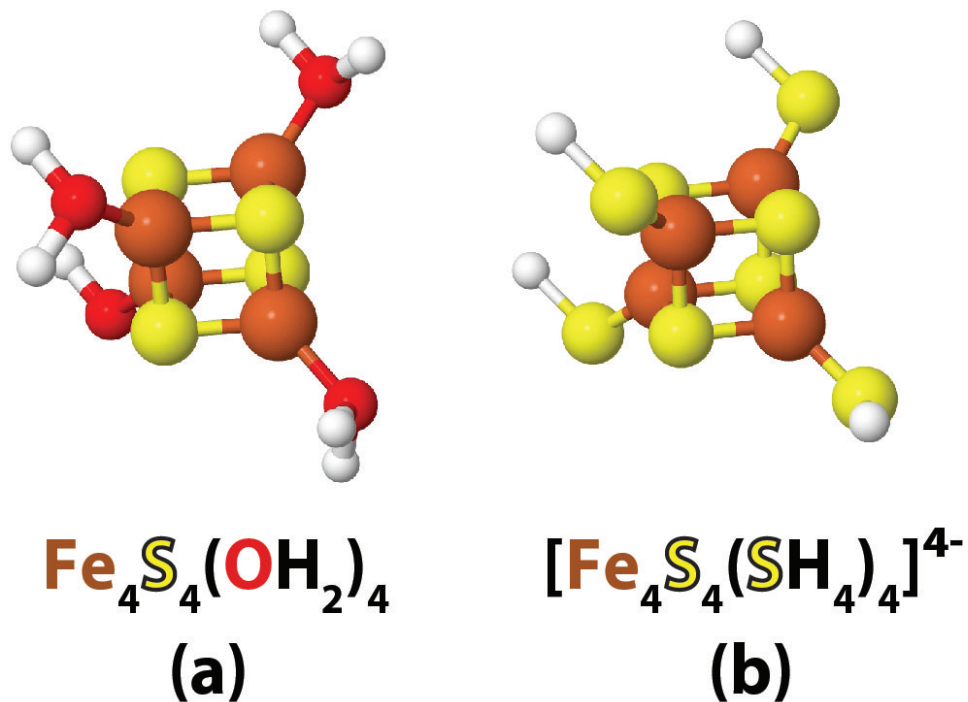


Figure 2.1: Molecules of (a)  $\text{Fe}_4\text{S}_4(\text{OH}_2)_4$  and (b)  $[\text{Fe}_4\text{S}_4(\text{SH}_4)_4]^{4-}$  clusters

the more thermodynamically stable octahedrally coordinated  $\text{Fe}_6\text{Ch}_6$  network. Besides this template effect, the hydrogen generated during the corrosion of Fe powder provides a reducing atmosphere to prevent  $\text{Fe}^{2+}$  from further oxidation to  $\text{Fe}^{3+}$ .

### 2.1.2 Top-down Approach

Although pure FeS and  $(\text{Li}_{1-x}\text{Fe}_x\text{OH})\text{Fe}_{1-y}\text{Ch}$  samples can be obtained using the aforementioned bottom-up approach, the as-recovered products are in powder forms. In order to obtain their simple crystal forms, we employ a top-down topochemical approach using single crystal templates. The template crystals consisting of existing tetragonal *MCh* layers, such as  $\text{K}_x\text{Fe}_{2-y}\text{Ch}_2$ , are grown using high-temperature solid-state routes. The crystal precursors are then reacted under hydrothermal conditions for topochemical

deintercalation or ion-exchange. The high-temperature grown crystals usually consists of high Fe vacancies. Therefore, Fe powders are always necessary for the crystal conversion as  $\text{Fe}^{2+}$  ions are formed under hydrothermal conditions and refill the Fe vacancies in the  $\text{FeCh}$  layers of the single crystals.

## **2.2 Characterization Methods**

### **2.2.1 Powder X-ray Diffraction**

Room temperature powder X-ray diffraction (PXRD) data were collected on a Bruker D8 X-ray diffractometer (Cu  $K\alpha$  radiation,  $\lambda = 1.5418 \text{ \AA}$ ) at the University of Maryland X-ray Crystallographic Center (XCC). For a routine measurement, data were collected with a step size of  $0.02^\circ$  between  $5^\circ$  and  $70^\circ$ . Temperature dependent X-ray diffraction measurements were performed using a Bruker C2 diffractometer with a Vantec500 2D detector,  $\lambda = 1.5418 \text{ \AA}$  (step size =  $0.05^\circ$ , with  $2\theta$  ranging from  $11^\circ - 80^\circ$ ). The sample was heated using an Anton Paar DHS 1100 graphite-dome hot stage.

Mail-in high-resolution synchrotron X-ray diffraction were carried out at Beamline 11-BM at the Advanced Photon Source (APS) at Argonne National Laboratory (ANL). Diffraction data were collected between  $0.5^\circ$  and  $46^\circ$  with a step size of  $0.0001^\circ$  using a constant wavelength with an energy of approximately 30 keV (exact wavelength depends on the beamline cycle).

In order to find any possible crystallographic phase transitions that are coupled to either the superconducting or magnetization order parameters, temperature dependent (5-300 K) high-resolution synchrotron X-ray diffraction was carried out for powders of

ground single crystals at Beamline 11-BM at the Advanced Photon Source (APS). An Oxford helium cryostat (closed flow system) was used to reach a temperature that is close to liquid helium ( $\approx 4$  K). Ground powders of single crystals were packed in 0.4 mm Kapton capillaries tubes and sealed with epoxy. Diffraction data were collected between  $0.5^\circ$  and  $46^\circ$  with a step size of  $0.0001^\circ$  using a constant wavelength.

All diffraction data were either fit with Pawley routine to extract lattice constants or Rietveld refinement to obtain better structural parameters using TOPAS academic 4.2.<sup>66</sup>

### **2.2.2 Neutron Powder Diffraction**

Neutron powder diffraction (NPD) diffraction data were collected on the BT-1 high-resolution neutron powder diffractometer with either the Cu(311) monochromator ( $\lambda = 1.540$  Å) or the Ge(311) monochromator ( $\lambda = 2.0790$  Å) at the NIST (National Institute of Standards and Technology) Center for Neutron Research (NCNR). The samples were loaded into He-filled vanadium cans and subsequently into a closed cycle refrigerator for low temperature measurements (3-300 K).

High-intensity and coarse-resolution diffraction measurements were carried out on the BT-7 spectrometer ( $\lambda = 2.359$  Å) using the position sensitive detector (PSD) to search for magnetic Bragg peaks from base temperature up to 150 K.<sup>67</sup>

### **2.2.3 Magnetic Susceptibility**

Most physical property measurements were carried out at the Center for Nanophysics and Advanced Materials (CNAM). Magnetic susceptibility measurements were performed

using a Quantum Design magnetic properties measurement System (MPMS), which is also called superconducting quantum interference device (SQUID). Both field-cooled (FC) and zero field-cooled (ZFC) measurements were taken from 2 K to 300 K in direct current mode with an applied magnetic field of 10 Oe – 300 Oe. Hysteresis measurements were carried out at different temperatures with applied magnetic field between  $H = \pm 7$  T.

Magnetic susceptibility measurements under hydrostatic pressure were performed using a BeCu piston-cylinder clamp cell employing n-pentane:isoamyl alcohol as a pressure-transmitting medium. Pressures produced on the single crystal sample at low temperatures were calibrated by measuring the Meissner effect of a small piece of Pb, placed in the pressure cell. The known pressure dependences of the superconducting transition temperature of Pb<sup>68</sup> were used for this purpose.

## 2.2.4 Resistivity and Heat Capacity

Routine electrical transport measurements were performed using either 9 T or 14 T Quantum Design physical property measurement system (PPMS) provided by CNAM. Single crystals were mounted on a Quantum Design DC resistivity puck. Thin gold wires were attached to the crystal to form electrical contacts via silver paste. An applied current of 0.1 mA with frequencies near 10 Hz was utilized.

Heat capacity measurements were performed in a 14 T Quantum Design Dynacool PPMS System. Single crystal samples or pellets pressed using ground powders were measured using the relaxation method with field applied perpendicular to the basal plane.<sup>69–71</sup>

### **2.2.5 Thermogravimetric Analysis**

Differential scanning calorimetry (DSC) was conducted on a Mettler-Toledo TGA/DSC 3+ thermogravimetric analyzer with high temperature furnace. Samples were heated from room temperature to 800 °C.

### **2.2.6 Electron Microscopy**

Electron microscopy characterizations were carried out at the Advanced Imaging and Microscopy Laboratory (AIM Lab) of the Maryland Nanocenter. Microscopic images were examined on a Hitachi SU-70 field emission scanning electron microscope (SEM), and their elemental compositions were determined by energy dispersive X-ray spectroscopy (EDS) using a BRUKER EDS detector. EDS analysis was carried out at 15 keV. Electron diffraction patterns were obtained using a JEM 2100 LaB<sub>6</sub> transmission electron microscope (TEM) at an acceleration voltage of 200 KeV.

### **2.2.7 ICP-AES**

Inductively coupled plasma atomic emission spectroscopy (ICP-AES) data were collected using a Shimadzu ICPE-9000 spectrometer. Standards with concentrations of 20, 10, 5, 2, 1, 0.5, 0.2 ppm used for ICP-AES were diluted from 1000 ppm of respective elements purchased from FLUKA. Samples measured with ICP-AES were dissolved in concentrated nitric acid and then diluted to concentrations between 1-10 ppm in a volumetric flask.

## 2.2.8 Computational methods

All density functional theory (DFT)<sup>72,73</sup> calculations were performed by using the Vienna Ab-initio Simulation Package (VASP)<sup>74-77</sup> software package with potentials using the projector augmented wave (PAW)<sup>78</sup> method. The exchange and correlation functional were treated by the generalized gradient approximation (PBE-GGA).<sup>79</sup> The cut-off energy, 450 eV, was applied to the valence electronic wave functions expanded in a plane-wave basis set for all chalcogenides. A Monkhorst-Pack<sup>80</sup> generated  $23 \times 23 \times 17$  k-point grid was used for the Brillouin-zone integration to obtain accurate electronic structures. Crystal orbital Hamilton populations (COHP) were extracted using the program Local-Orbital Basis Suite Towards Electronic-Structure Reconstruction (LOBSTER) developed by Dronskowski et al<sup>81-84</sup>. COHP provides an intuitive chemical bonding analysis to the calculated electronic structures.

## Chapter 3: Tetrahedral Superconducting FeS Single Crystals

The work described within this chapter was published in *Physical Review B* **2015**, *93*, pg. 094522. Christopher K. H. Borg, Christopher Eckberg, Daniel Campbell, Shanta Saha, Johnpierre Paglione and Efrain Rodriguez were contributing authors of the manuscript. X.Z. contributed to crystal growth, X.Z. and C.K.H.B. collected XRD and MPMS data, C.K.H.B, C.E. and D.C. collected the resistivity data, S.S. collected MPMS measurements using a pressure cell.

### 3.1 Introduction

While the field of iron-based superconductors has focused primarily on selenides, tellurides, and arsenides,<sup>11,85,86</sup> recent developments show that sulfides are a possible new avenue for high- $T_c$  superconductors. The first iron-sulfide superconductor,  $\text{BaFe}_2\text{S}_3$ , has been reported to have a superconducting critical temperature ( $T_c$ ) = 14 K at a high pressure of 11 GPa.<sup>87</sup> An even simpler sulfide,  $\text{H}_2\text{S}$ , under high pressure (90 GPa), has been found to exhibit superconductivity as high as 203 K, which is the highest reported  $T_c$  thus far.<sup>88</sup> Sulfides in general therefore merit closer inspection for exploring high temperature superconductivity, and iron sulfides in particular could point the way towards new superconducting compounds.

Recently, Lai *et al.* found that the simple binary compound, FeS, in its tetragonal polymorph known as mackinawite is a superconductor with a  $T_c = 5$  K.<sup>63</sup> Similar to the superconducting  $\beta$ -form of iron selenide, mackinawite also adopts the anti-PbO structure where FeS<sub>4</sub> tetrahedra edge-share to form two-dimensional (2D) layers (Figure 3.1b inset).<sup>89-91</sup> Unlike its heavier analogues, FeSe and FeTe, however, mackinawite is metastable and therefore cannot be synthesized from their respective elements using solid state methods, unless it is alloyed with significant amounts of Co, Ni or Cu.<sup>92,93</sup> Due to the thermodynamic limitations in its preparation, single crystal growth of mackinawite is a challenge. Growing single crystals of FeS is imperative, however, towards understanding its true physical properties.

Before the report by Lai *et al.* on superconductivity, several studies had found FeS to be a ferrimagnetic semiconductor.<sup>94,95</sup> The conflicting reports on the properties of polycrystalline FeS by different groups may be due to impurities not observed through powder X-ray diffraction, especially since iron provides a high background from fluorescence with Cu K- $\alpha$  radiation. Powder FeS samples prepared through aqueous methods may form small crystallites as indicated by the broad Bragg reflections in the diffraction patterns of past studies.<sup>96</sup> The small particle size and polycrystalline nature of these samples impede accurate electrical resistivity and magnetization measurements due to grain boundary effects and the facile oxidation of surfaces of small particles.<sup>90,94</sup> Despite their ground-breaking work on polycrystalline FeS, Lai *et al.* also called for high quality single crystal data for definitive determination of the physical properties of FeS.

We found a method for the preparation of high quality single crystals of mackinawite FeS. Since FeS is metastable,<sup>97,98</sup> single crystal growth through slow cooling of

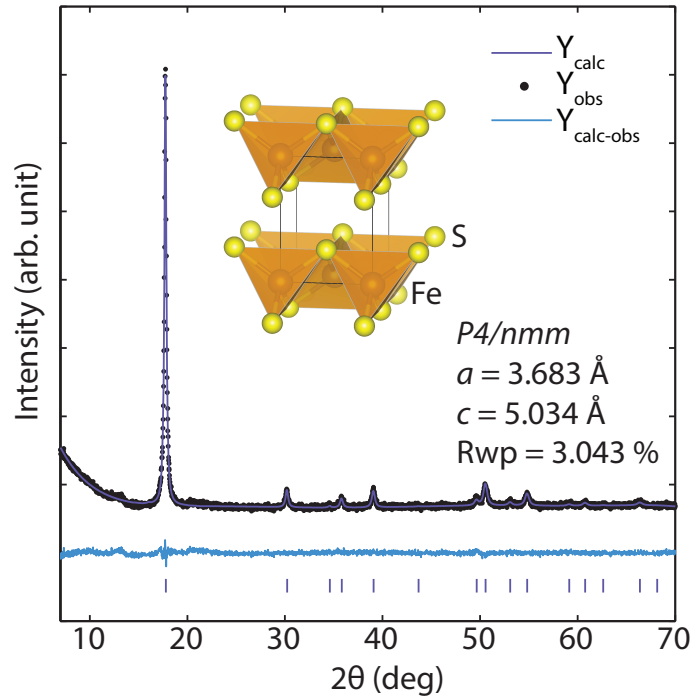


Figure 3.1: Rietveld refinement with XRD powder diffraction on ground single crystal samples. (a) Refinement of  $K_xFe_{2-y}S_2$  template's body-centered tetragonal structure ( $I4/mmm$ ). (b) Refinement of the FeS product's structure with a primitive tetragonal model ( $P4/nmm$ ). Fe (orange) ions are tetrahedrally coordinated to S (yellow) anions, and the K (purple) cations are located between two FeS layers. Tick marks corresponding to their respective phase are shown below the difference curve.

a melt is not possible. In the case of  $FeSe_{1-y}Te_y$ <sup>99-101</sup> and  $Fe_{1+x}Te$ ,<sup>102,103</sup> large single crystals were grown through Bridgeman techniques allowing detailed transport and spectroscopic experiments. For FeSe, which has limited window of phase stability, chemical vapor transport methods at elevated temperatures is the only technique that has been reported.<sup>104,105</sup> We present a general technique for the de-intercalation of the ternary phase  $K_xFe_{2-y}S_2$  (Figure 3.1a inset), which melts congruently (uniform composition for both liquid and solid phases) and can therefore be prepared in single crystal form.<sup>106,107</sup> We link how studying the materials chemistry of layered iron sulfides is key to discovering the

underlying physics in new superconductors such as mackinawite FeS.

## 3.2 Experimental

### 3.2.1 Hydrothermal synthesis of FeS single crystals

In this work, superconducting FeS single crystals were prepared by de-intercalation of potassium cations from  $K_xFe_{2-y}S_2$  ( $x \approx 0.8$ ,  $y \approx 0.4$ ) single crystals under hydrothermal condition. The growth of  $K_xFe_{2-y}S_2$  single crystals was modified by the method described by Lei *et al.*<sup>108</sup> For a typical reaction, 1.00 g (11.4 mmol) of hexagonal FeS powder (Alfa Aesar, 99.9%) was mixed with 0.18 g (4.5 mmol) of potassium metal (Alfa Aesar, 99%) to match the nominal composition of  $K_{0.8}Fe_2S_2$ . The mixture was loaded in a quartz ampoule inside an argon-filled glovebox, and the ampoule was flame sealed under vacuum ( $10^{-3}$  Torr). In order to avoid oxidation of the sample due to the potassium-induced corrosion of quartz, the sample containing ampoule was sealed in a larger ampoule under vacuum ( $10^{-3}$  Torr).

For crystal growth of  $K_xFe_{2-y}S_2$ , the mixture was heated to 1000 °C over 10 hours and held at 1000 °C for 3 hours to form a homogeneous melt. Subsequently, the melt was slowly cooled at a rate of 6 °C/hour to 650 °C to allow crystal growth. After cooling to room temperature,  $K_xFe_{2-y}S_2$  single crystals approximately 3 mm – 8 mm in diameter and approximately 0.1 mm in thickness were recovered.

For the preparation of FeS single crystals, the  $K_xFe_{2-y}S_2$  precursor (0.2 g - 0.4 g), 0.28 g (5 mmol) Fe powder (Alfa Aesar, 99.9%), 0.84 g (5 mmol)  $Na_2S \cdot 5H_2O$  (dried from  $Na_2S \cdot 9H_2O$ , Sigma-Aldrich, 98%) and 0.20 g (5 mmol) NaOH (Sigma-Aldrich,

98%) were added to 10 mL water. The mixture was placed in a Teflon-lined stainless steel autoclave at 120 °C for 3-4 days. Silver colored FeS single crystals were recovered by washing away excess powder with water and drying under vacuum overnight. The FeS crystals retained the shapes of the  $K_xFe_{2-y}S_2$  crystals (up to 8 mm in diameter), and the yield was generally above 80%. Samples prepared in the absence of excess iron powder were not superconducting, which could be due to either oxidation of the iron or vacancy formation in the FeS layer. All others were found to be superconducting. In the crystallographic studies of layered iron selenide analogues such as FeSe<sup>16</sup> and  $(Li_xFe_{1-x}OH)FeSe$ ,<sup>26</sup> iron vacancy formation is implicated in the loss of superconducting properties.

### 3.2.2 X-ray diffraction and thermal stability analysis

Initial powder X-ray diffraction (XRD) data were collected using a Bruker D8 X-ray diffractometer with Cu  $K\alpha$  radiation,  $\lambda = 1.5418 \text{ \AA}$  (step size =  $0.025^\circ$ , with  $2\theta$  ranging from  $7^\circ - 90^\circ$ ). Temperature dependent X-ray diffraction on ground single crystals was performed using a Bruker C2 diffractometer with a Vantec500 2D detector,  $\lambda = 1.5418 \text{ \AA}$  (step size =  $0.05^\circ$ , with  $2\theta$  ranging from  $11^\circ - 80^\circ$ ). The sample was heated using an Anton Paar DHS 1100 graphite-dome hot stage. Rietveld refinements were carried out using TOPAS software.

Differential scanning calorimetry (DSC) was conducted on a Mettler-Toledo TGA/DSC 3+ thermogravimetric analyzer with high temperature furnace. Samples were heated from room temperature to 800 °C.

### 3.2.3 Magnetic susceptibility, electrical transport and heat capacity

Magnetic susceptibility measurements were performed using a Quantum Design Magnetic Properties Measurement System (MPMS). Both field-cooled (FC) and zero field-cooled (ZFC) measurements were taken from 2 K to 300 K in direct current mode with an applied magnetic field of 10 Oe – 30 Oe. Hysteresis measurements were carried out at 2 K with  $H = \pm 7$  T. Magnetic susceptibility measurements under hydrostatic pressure were performed using a BeCu piston-cylinder clamp cell employing n-pentane:isoamyl alcohol as a pressure-transmitting medium. Pressures produced on the single crystal sample at low temperatures were calibrated by measuring the Meissner effect of a small piece of Pb, placed in the pressure cell. The known pressure dependences of the superconducting transition temperature of Pb<sup>68</sup> were used for this purpose.

Electrical transport measurements were performed on a 14 T Quantum Design Dynacool Physical Properties Measurement System (PPMS). Single crystal samples were mounted on a rotator AC transport sample board and measured using the electrical transport option, applying currents between 0.1-0.5 mA and frequencies near 10 Hz.

Heat capacity measurements were performed in a 14 T Quantum Design Dynacool PPMS System. The single-crystal sample of mass 2.9 mg was measured using the relaxation method with field applied perpendicular to the basal plane.

### 3.3 Results: Synthesis, thermal stability and structural characterization

#### 3.3.1 Single crystal preparation by reductive deintercalation

Our strategy for preparing single crystals of a metastable phase can be summarized as crystal-to-crystal conversion from a thermodynamically stable phase. During the preparation of our FeS samples, we found that maintaining a reducing and basic hydrothermal environment was crucial to observing superconductivity in FeS. The deintercalation of potassium cations from  $K_xFe_{2-y}S_2$  resulted in the shift of alternating planes of FeS along the  $a$  direction of the unit cell to form the primitive layered FeS (Fig. 3.1). Note that Lei *et al.* had found  $K_xFe_{2-y}S_2$  to be non-superconducting,<sup>109</sup> so our reductive de-intercalation technique tunes this spin glassy material into a superconductor.

A similar structural transformation from a body-centered tetragonal structure to a primitive tetragonal structure has also been previously observed in the selenide analogue,  $K_xFe_{2-y}Se_2$ .<sup>38</sup> When exposed to air or moisture, oxidation of iron and formation of iron vacancies was suggested to be the driving force for the structural transition. After the structural change induced by oxidation in water, the superconducting  $K_xFe_{2-y}Se_2$  became non-superconducting.<sup>38</sup> In contrast, our reductive de-intercalation was driven by preference of potassium cations to solvate into solution under strongly basic conditions, which consequently alters the non-superconducting  $K_xFe_{2-y}S_2$  (Fig. 3.2) into superconducting FeS. Also, the reducing environment in the autoclave maintained by the presence of Fe metal as a reagent prevented oxidation of  $Fe^{2+}$  to  $Fe^{3+}$  or the formation of iron vacancies.

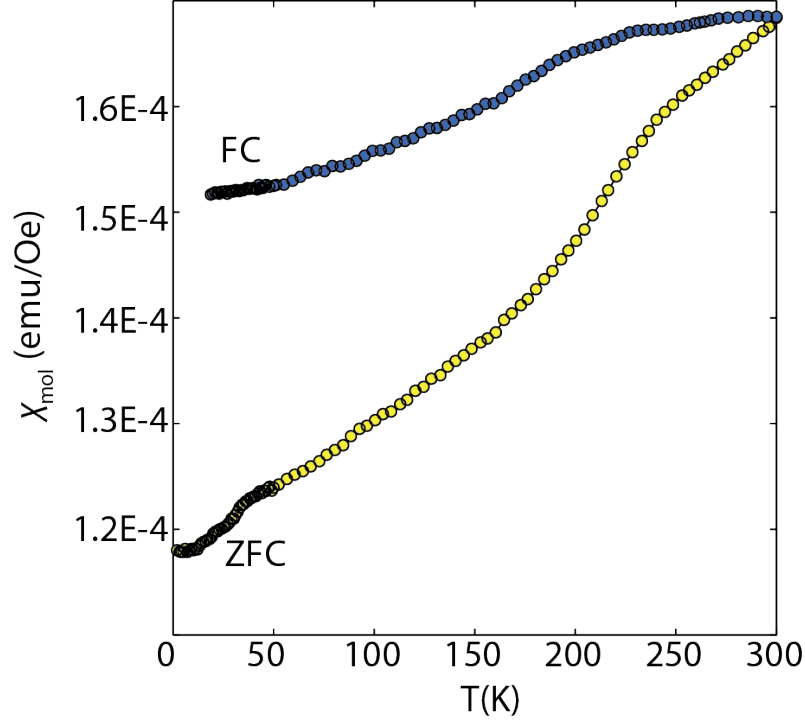


Figure 3.2: Magnetic susceptibility of  $K_xFe_{2-y}S_2$  starting material. Lack of diamagnetic transition shows that sample is non-superconducting.

A more drastic structural change could be possible under stronger oxidizing conditions. Neilson and McQueen<sup>110</sup> reported that  $KNi_2Se_2$ , a Ni analogue of the  $K_xFe_{2-y}Se_2$ , forms hexagonal NiAs-type,  $K_{1-y}Fe_{2-z}Se_2$ , by oxidative de-intercalation of  $K^+$  by  $CuI_2$  in acetonitrile. This caused a complete structural reconstruction from edge-sharing layered  $NiSe_4$  tetrahedra to corner-sharing  $NiSe_6$  octahedra. Such a reconstruction was not seen in our de-intercalation reaction of  $K_xFe_{2-y}S_2$  since we did not utilize strong oxidizing environment but rather maintained reducing conditions. We similarly found this strategy in achieving the highest  $T_c$ 's for the  $(Li_{1-x}Fe_xOH)FeSe$  and  $(Li_{1-x}Fe_xOD)FeSe$  single crystals in their single crystal-to-single crystal conversion also utilizing  $K_xFe_{2-y}Se_2$  as the template.<sup>53</sup> A similar method was used for ion exchange in the single-crystal conversion of the selenide analogues  $K_xFe_{2-y}Se_2$  to  $(Li_xFe_{1-x}OH)FeSe$ ,<sup>111</sup> which demonstrates how

powerful this technique is for exploring new layered iron chalcogenides.

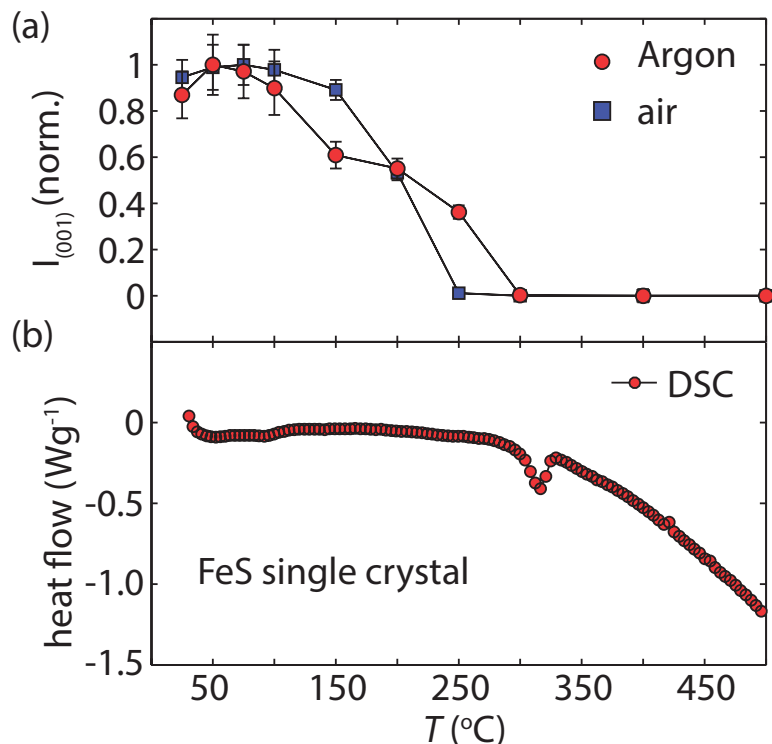


Figure 3.3: (a) Normalized integrated intensity of the (001) peak (top) from temperature dependent XRD. Under Argon (red curve), the loss of the (001) peak is gradual and is absent above 250 °C. Under air (blue curve), the loss of (001) peak is more abrupt and the peak is absent above 200 °C. (b) DSC results, plotted as heat flow as a function of temperature, for single crystal FeS. The sudden change in heat flow at 300 °C is associated with an endothermic reaction.

### 3.3.2 X-ray diffraction and crystal structure

The XRD powder pattern of ground single crystals of  $\text{K}_x\text{Fe}_{2-y}\text{S}_2$ , presented in Figure 3.1a, shows pure crystalline product before the de-intercalation reactions. The pattern for  $\text{K}_x\text{Fe}_{2-y}\text{S}_2$  was fit with a body-centered tetragonal structural model with space group  $I4/mmm$  and lattice parameters  $a = 3.745(1)$  Å and  $c = 13.627(9)$  Å (Table 3.1, Figure 3.1). Full structural parameters from the fits are presented in Table 3.1 and are in good agreement with those presented in an earlier study.<sup>109</sup> Recently, Pachmayer *et al.* found

that FeS powders prepared by hydrothermal methods remain tetragonal down to low temperatures;<sup>59</sup> while the heavier congeners, FeSe<sup>16,105,112</sup> and FeTe,<sup>62,113</sup> are known to have a crystallographic phase transitions.

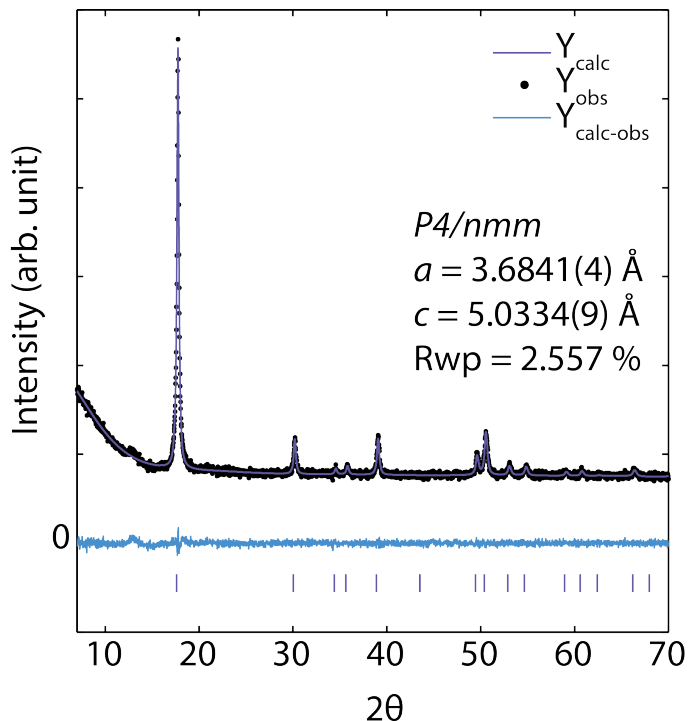


Figure 3.4: Rietveld refinement of XRD pattern of powder FeS produced from the addition of Fe and  $\text{Na}_2\text{S} \cdot 9\text{H}_2\text{O}$  during reductive de-intercalation of  $\text{K}_x\text{Fe}_{2-y}\text{S}_2$  single crystals. Powder produced from this method is produced concurrently with FeS single crystals but is structurally distinct.

After hydrothermal de-intercalation of potassium cations, the XRD pattern of the newly formed superconducting FeS crystals were fit to a primitive unit cell with space group  $P4/nmm$  and lattice parameters  $a = 3.6826(5) \text{ \AA}$  and  $c = 5.03440(9) \text{ \AA}$ . These values were consistent with values previously reported for tetragonal FeS.<sup>63,92,94</sup> Due to the layered nature of the samples, the XRD powder patterns for  $\text{K}_x\text{Fe}_{2-y}\text{S}_2$  and FeS were refined with preferred orientation along the [002] and [001] directions, respectively. Table 3.1 presents the parameters of our structural refinements for ground single crystals of

$K_xFe_{2-y}S_2$  and FeS as well as the powder samples of FeS prepared as a side reaction during the single-crystal-to-single-crystal conversion. This powder consisted primarily of the product from the reaction of the iron powder in the presence of sodium sulfide and NaOH during the hydrothermal preparation (Fig. 3.4). For comparison, we have also prepared a phase pure powder sample of FeS with a  $T_c$  of 4.5 K through a modified method employed by Lai *et al.*<sup>63</sup>

### 3.3.3 Thermal stability of FeS single crystals

To test the thermal stability of our new FeS single crystals, samples were heated under inert Argon atmosphere in steps ranging from 25 °C, 50 °C, and 100 °C. The 001 peak is visible up to 250 °C (Fig. 3.5), and its integrated intensity versus temperature under an Argon atmosphere is presented in Figure 3.3a along with a plot of the DSC. The decomposition of mackinawite FeS as determined by the integrated intensity of the (001) peak begin above 100 °C and disappeared completely above 250 °C. Due to the geometry of the XRD experiment, the (00*l*) reflections in the single crystal sample were observed while other reflections were not. Therefore, it is likely that if greigite were to form above  $T = 100$  °C, it would not have been detected in our experiment.

DSC measurements of FeS in Argon up to 600 °C, shown in Figure 3.3b, give some clues on the thermal behavior during the decomposition of mackinawite. The dip in the heat flow around 300 °C indicates an endothermic reaction that could be associated with the crystallization of a phase such as pyrrhotite not seen in our temperature dependent diffraction studies. The appearance of this transition in the DSC after the disappearance

Table 3.1: Structural parameters for ground single crystals of  $K_xFe_{2-y}S_2$  and FeS along with FeS obtained through powder methods. Rietveld refinements with XRD data are of the room temperature structures. In the FeS samples, we found full occupancy for the iron and sulfur sites. In the case of the  $K_xFe_{2-y}S_2$  single crystals we found  $x = 0.65(5)$  while  $y$  was fixed to zero. Relevant bond distances and angles are also included for each structural refinement.

FeS (298 K, ground single crystal), $P4/nmm$ , $R_{wp} = 3.042\%$					
$a = 3.6826(5)$ , $c = 5.03440(9)$					
atom	Site	x	y	z	$U_{iso}$ ( $\text{\AA}^2$ )
Fe1	2a	0	0	0	0.016(3)
S1	2c	0	0.5	0.266(2)	0.029(5)
S-Fe-S ( $^\circ$ )	S-Fe-S ( $^\circ$ )	Fe-S ( $\text{\AA}$ )	Fe-Fe ( $\text{\AA}$ )	anion height ( $\text{\AA}$ )	
108.1(2)	110.2(2)	2.275(5)	2.6040(5)	1.34(1)	
FeS (298 K, powder preparation), $P4/nmm$ , $R_{wp} = 2.557\%$					
$a = 3.6841(4)$ , $c = 5.0334(9)$					
atom	Site	x	y	z	$U_{iso}$ ( $\text{\AA}^2$ )
Fe1	2a	0	0	0	0.034(3)
S1	2c	0	0.5	0.253(2)	0.033(4)
S-Fe-S ( $^\circ$ )	S-Fe-S ( $^\circ$ )	Fe-S ( $\text{\AA}$ )	Fe-Fe ( $\text{\AA}$ )	anion height ( $\text{\AA}$ )	
110.7(4)	108.9(2)	2.239(5)	2.6051(4)	1.27(1)	
$K_xFe_{2-y}S_2$ (298 K, single crystal), $I4/mmm$ , $R_{wp} = 3.873\%$					
$a = 3.745(1)$ , $c = 13.627(9)$					
atom	Site	x	y	z	$U_{iso}$ ( $\text{\AA}^2$ )
K1	2a	0	0	0	0.006(2)
Fe1	4d	0	0.5	0.25	0.019(7)
S1	4e	0	0	0.352(2)	0.006(8)
S-Fe-S ( $^\circ$ )	S-Fe-S ( $^\circ$ )	Fe-S ( $\text{\AA}$ )	Fe-Fe ( $\text{\AA}$ )	anion height ( $\text{\AA}$ )	
110.8(3)	106.8(3)	2.33(2)	2.6481(6)	1.39(3)	

of the (001) reflection in the XRD, indicates that the two are related. XRD analysis on the residue from the DSC experiment indicated formation of hexagonal pyrrhotite (Fig. 3.6). The higher than expected thermal stability of the mackinawite compared to past studies could be due to the single crystalline nature of our samples, which have larger surface areas and are therefore less reactive than a polycrystalline product with small particle

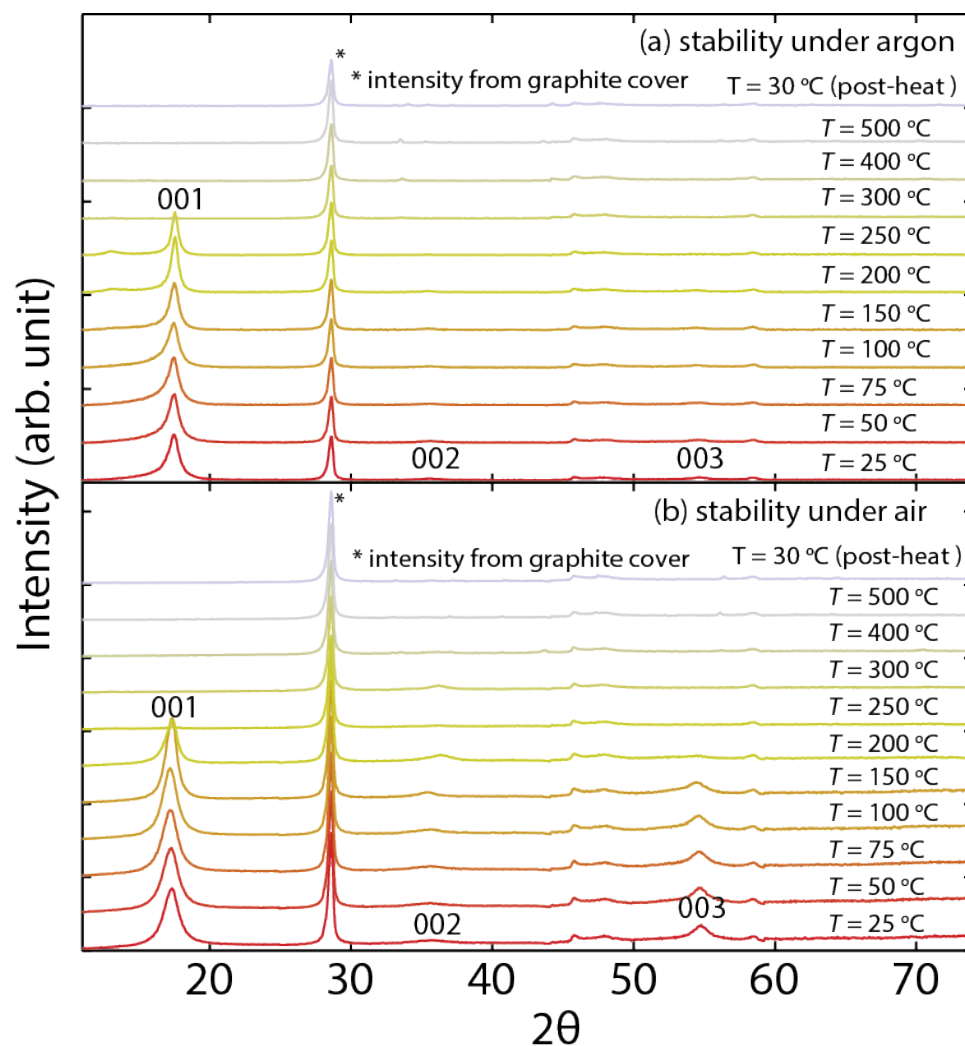


Figure 3.5: Temperature-dependent XRD patterns of single crystal FeS orientated along the 001 direction. (a) XRD under Argon, the 001 peak is visible up to 250 °C. (B) XRD under air, the 001 peak is visible up to 200 °C.

sizes.

From their high-resolution X-ray diffraction study, Lennie *et al.* reported that mackinawite begins to decompose to greigite ( $\text{Fe}_3\text{S}_4$ ) above 100 °C and that all FeS reflections disappear above  $T = 200$  °C under a He atmosphere.<sup>114</sup> Above 260 °C, greigite decomposes and hexagonal pyrrhotite begins to emerge.<sup>114</sup>

Lennie *et al.* also reported that mackinawite-FeS rapidly oxidizes under air.<sup>92</sup> To

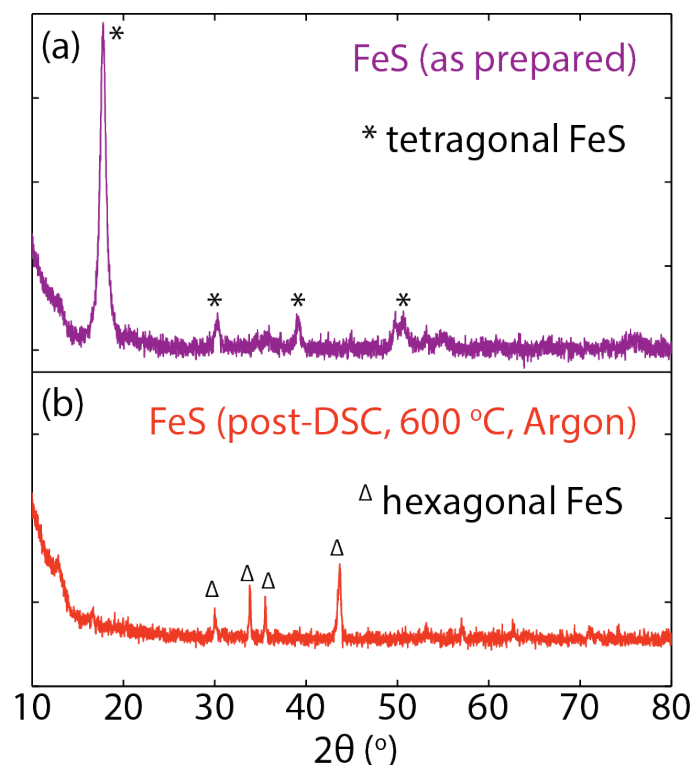


Figure 3.6: XRD patterns of ground FeS crystals before and after DSC measurement. (a) Room-temperature XRD of FeS crystals as prepared from hydrothermal synthesis. \* indicates peaks due to tetragonal FeS (mackinawite). (b) Room-temperature XRD of FeS powder post-DSC measurement. Powder was subjected to heating up to 600 °C under Argon.  $\delta$  indicates peaks due to hexagonal FeS (pyrrhotite).

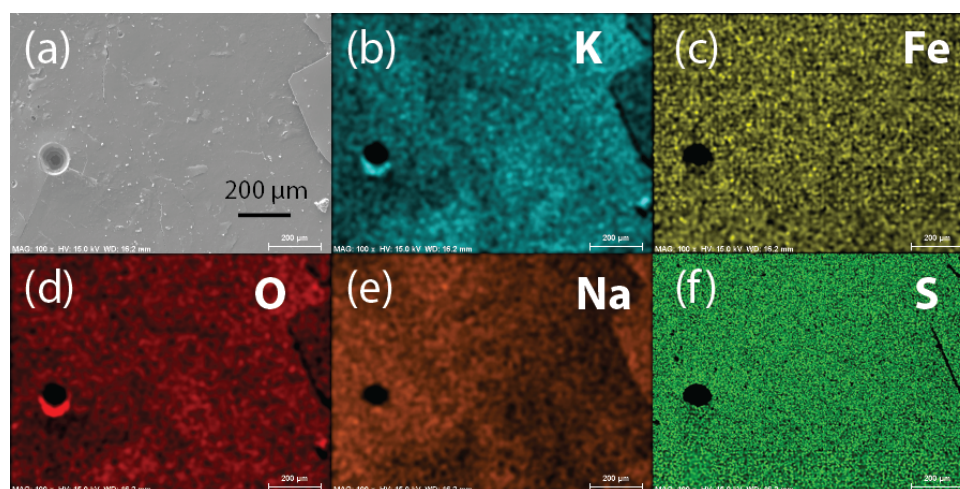


Figure 3.7: Elemental analysis of surface of FeS single crystal using EDS mapping shows up to 9 % alkali metal.

test the air stability of our single crystals, we heated samples under ambient atmosphere in steps ranging from 25 °C, 50 °C, and 100 °C. As presented in Fig 3.3b, the (001) peak is visible up to 200 °C. As this level of air stability has not been reported for mackinawite before, it could imply that there may be some alkali metal incorporation that could passivate the surface and prevent oxidation of FeS. EDS mapping on the surface of FeS single crystals shows up to 9% total alkali (K and Na) on the surface of the FeS crystals (Fig. 3.7). Due to the similarity of the  $c$ -parameter to those previously reported FeS, it is unlikely that large cations such as sodium or potassium intercalate between layers since we did not observe an increase in the (001)  $d$ -spacing. However, as indicated by the EDS measurements, it is possible that some alkali metal is incorporated to other sites in the crystals, and future studies will be pursued to find their location if indeed present.

## 3.4 Results: Physical properties

### 3.4.1 Magnetic susceptibility

The temperature-dependent FC and ZFC magnetic susceptibilities of FeS crystals measured in a constant field of 1 mT are presented in Figure 3.8, for fields applied both parallel and perpendicular to the crystallographic  $c$ -axis. The volume susceptibility  $4\pi\chi$  under ZFC conditions exhibits an onset superconducting transition at  $T_c = 3.5$  K and a shielding fraction of  $4\pi\chi \approx 60\text{-}90\%$  (without geometric factors taken into account). The significant superconducting volume fractions indicate that FeS is a bulk superconductor. In both cases of the field orientation, the ZFC and FC curves in the normal state above  $T_c$  are largely temperature independent, indicative of Pauli paramagnetism and therefore

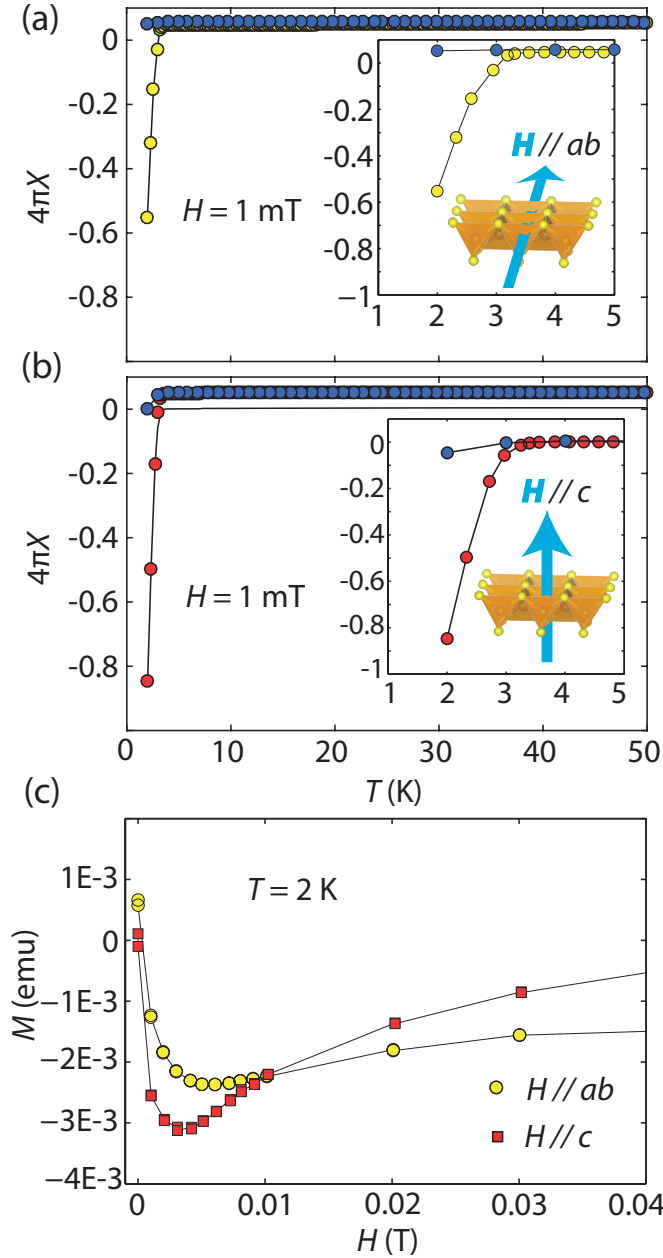


Figure 3.8: Magnetic susceptibility of an FeS single crystal. (a) Temperature-dependent volume susceptibility  $4\pi\chi$  of an FeS crystal with a  $H \parallel ab$  shows Pauli paramagnetic behavior in the normal state and transitions to the superconducting at  $T_c = 3.5$  K. (b) Susceptibility for  $H \parallel c$  with an increased diamagnetic response with a relative volume fraction increase of 30% (c) Magnetization  $M$  as a function of applied field at 2 K. The diamagnetic response weakens for fields greater than 4 mT ( $H \parallel ab$ ) and 5 mT ( $H \parallel c$ ).

metallicity in FeS.

Figure 3.8c presents magnetization ( $M$ ) as a function of applied field ( $H$ ) along two

different directions for the applied field. The  $M(H)$  isotherms indicate the values of the lower critical field  $H_{c1}$  to be 4 mT and 5 mT at 1.8 K for  $H||ab$  and  $H||c$ , respectively. One difference between our single crystal results and those of Lai *et al.* is the maximum critical temperature observed. Lai *et al.* reported the superconducting powder samples of FeS to have a  $T_c = 4.5$  K,<sup>63</sup> which is approximately 1 K greater than found for our single crystals. Magnetic susceptibility of our own prepared powder samples show  $T_c^{onset} = 4$  K.

### 3.4.2 Heat capacity

Heat capacity was measured on a large single crystal in both the superconducting (0 T) and normal (3 T) states. As shown in Figure 3.9, a 3 T field is large enough to suppress the superconducting state in the crystal, making for a good comparison with the 0 T curve.

In zero applied field, a clear signature of the superconducting transition develops at  $T_c=3.9$  K, consistent with magnetic susceptibility and resistivity (below) measurements, confirming bulk superconductivity in single crystal FeS. Fitting the 3 T data to a standard electron and phonon contribution specific heat model,  $C = \gamma T + \beta T^3$ , yields a normal state Sommerfield coefficient to be  $\gamma=5.1$  mJ/mol-K<sup>2</sup> and phonon term  $\beta=0.23$  mJ/mol-K<sup>4</sup>, the latter corresponding to a Debye temperature  $\Theta_D= 257$  K. Unlike reports for FeSe where the specific heat was fit to  $C = \gamma T + \beta_3 T^3 + \beta_5 T^5$ ,<sup>16</sup> for FeS a plot for  $C/T$  vs  $T^2$  is linear in the normal state. FeS does share some similarities with FeSe, however, as  $\gamma$  was estimated to be 5.4(3) mJ/mol-K<sup>2</sup>,<sup>16</sup> which is within error to the value we found for  $\gamma$  in FeS.

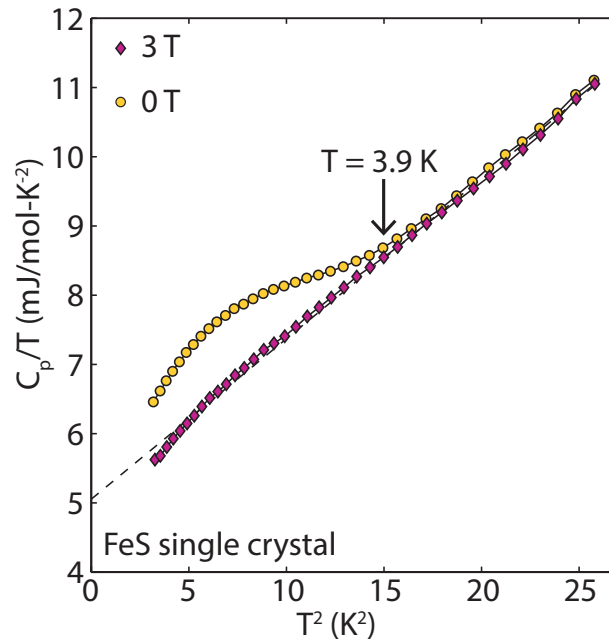


Figure 3.9: Low temperature specific heat of single crystal FeS for 0 T and 3 T applied magnetic fields. The arrow indicates the onset of a superconducting feature at  $T = 3.9$  K.

### 3.4.3 Magnetoelectric transport

Temperature dependent electrical resistivity of single-crystal FeS is presented in Figure 3.11a. The resistivity exhibits metallic character down to the superconducting state with  $T_c^{onset} = 3.5$  K and  $T_c^{zero} = 2.4$  K. The residual resistivity of FeS was determined to be  $\rho_0 = 240 \mu\Omega\text{-cm}$  based on an average of the values measured for several samples (Fig. 3.10), all of which exhibit a room temperature to residual resistivity ratio (RRR) of approximately 10, indicative of the high quality of our crystalline samples and the low uncertainty in geometric factors that may vary widely due to the micaceous nature of the crystals.

Figure 3.11b presents the normalized magnetoresistance (MR) as a function of applied magnetic field at 1.8 K. As shown, a significant anisotropy appears in both the

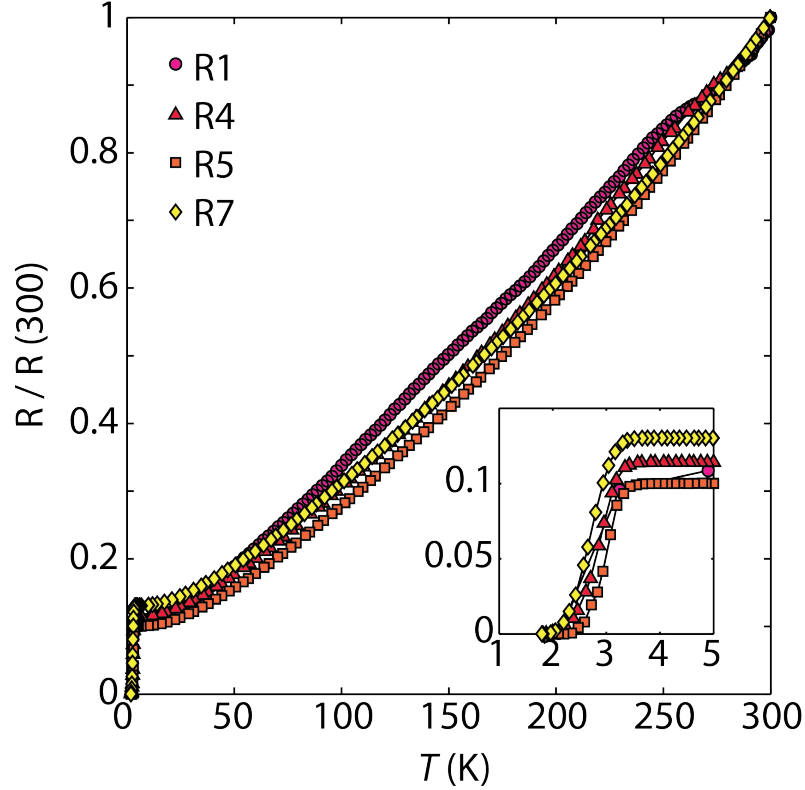


Figure 3.10: Electrical resistivity measurements of different crystals of FeS. R1, R4, R5, R7 are labeled to indicate that the measurement was performed on different crystals from the same synthetic method. Inset highlights low temperature transition to superconductivity.

normal state high-field MR as well as the  $H_{c2}$  transition, with the latter ranging from 0.16 T for  $H \parallel c$  to 1.6 T for  $H \parallel ab$ . The full angular dependence of these features are presented in Figure 3.12. Panels (a) and (b) present the angular variation of MR for both longitudinal ( $H(90^\circ) \parallel I$ ) and transverse ( $H(\theta) \perp I$ ) orientations, respectively. Indeed, as shown in Figure 3.12c, the MR angular variation is well represented by a cosine-like dependence for both longitudinal and transverse orientation angles.

A very large anisotropy is also evident in the upper critical field  $H_{c2}$  as the field angle is rotated away from the  $c$ -axis. In both longitudinal and transverse orientations,  $H_{c2}$  is observed to diminish strongly as the field rotates toward the basal plane, as shown

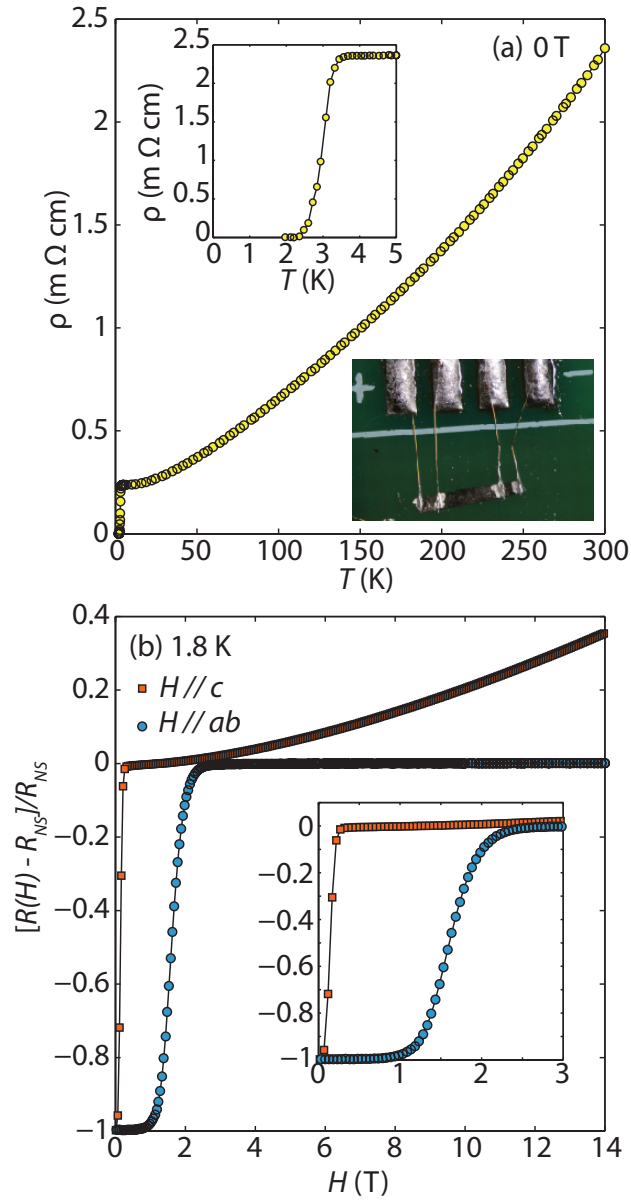


Figure 3.11: Electrical resistivity of single crystalline FeS. (a) Temperature-dependent resistivity with inset highlighting low temperature transition to the superconducting state at  $T = 3.5$  K. The geometry of the resistivity measurement for the single crystal also shown as inset. (b) Resistivity as a function of applied magnetic field for both  $H^{\parallel ab}$  and  $H^{\parallel c}$  orientations (always transverse to current direction).

in the insets of Figure 3.12a-b. Taking the two extremes, one can define an  $H_{c2}$  anisotropy

$\Gamma \equiv H_{c2}^{\parallel ab} / H_{c2}^{\parallel c}$ , which is a value of 10 at 1.8 K. A more complete evaluation of the full

$H_{c2}(T)$  dependence allows for an extrapolation of  $\Gamma$  to zero temperature. As shown in Figure 3.13a-d, extracting the  $H_{c2}(T)$  values from the resistive transitions at several angles (all transverse to current direction, with  $T_c$  values chosen at the 50% resistance midpoint) leads to a full  $H_{c2}(T)$  plot given in Figure 3.13e. For all field directions,  $H_{c2}(0)$  was estimated using the Werthamer-Helfand-Hohenberg (WHH) formula ( $H_{c2} = 0.69[-(dH_{c2}/dT)]|_{T_c T_c}$ ).<sup>115</sup> Fitting results give  $H_{c2}^{\parallel ab}(0) = 2.75$  T and  $H_{c2}^{\parallel c}(0) = 0.275$  T, yielding nearly the same anisotropy value  $\Gamma(0)=10$  as for 1.8 K. The coherence lengths calculated from the estimated  $H_{c2}(0)$  values ( $\xi = \sqrt{\Phi_0/(2\pi H_{c2})}$  where  $\Phi$  is the flux quantum) are calculated to be  $\xi_{H\parallel ab} = 343$  Å and  $\xi_{H\parallel c} = 104$  Å.

These large changes in  $H_{c2}$  with field angle and the concomitant coherence length anisotropy are in line with the strong anisotropy observed in the normal state MR as discussed above. To determine whether the large  $H_{c2}$  anisotropy is indicative of a truly two-dimensional and not a strongly anisotropic three-dimensional superconducting system, we performed detailed measurements of the angular dependence of  $H_{c2}$  at 1.8 K. Figure 3.14 presents the angle dependence of  $H_{c2}(1.8$  K) as determined from midpoints of field sweep resistive transitions. (Using different criterion to define  $H_{c2}$  results in slight variation in absolute anisotropy, but the shape of the  $H_{c2}(\theta)$  curve remains constant). The shape of the  $H_{c2}(\theta)$  curve, especially near the  $H \parallel ab$  ( $\theta = 90^\circ$ ) orientation, is indicative of the true dimensionality of the superconductor with respect to the coherence length. Tinkham's model for thin-film superconductors incorporates the effect of reduced dimen-

sionality,<sup>116</sup> yielding an angular dependence given by

$$\left| \frac{H_{c2}(\theta)\sin\theta}{H_{c2}^{\perp}} \right| + \left( \frac{H_{c2}(\theta)\cos\theta}{H_{c2}^{\parallel}} \right)^2 = 1, \quad (3.1)$$

whereas Ginzburg Landau (GL) theory<sup>117</sup> can be used to determine the effect of an anisotropic effective mass  $m^*$  on the angular dependence as

$$\left( \frac{H_{c2}(\theta)\sin\theta}{H_{c2}^{\perp}} \right)^2 + \left( \frac{H_{c2}(\theta)\cos\theta}{H_{c2}^{\parallel}} \right)^2 = 1. \quad (3.2)$$

As shown in the inset of Figure 3.14, the  $H_{c2}(\theta)$  data is much better represented by the anisotropic GL theory, suggesting a highly anisotropic 3D environment for the superconductivity in FeS. This can be quantified by using the calculated anisotropy for this sample  $\Gamma \simeq 12.8$  to extract the effective mass ratio  $m_{\parallel}^*/m_{\perp}^* = \Gamma^2 = 164$ . This is believed to be the largest upper critical field anisotropy observed in any Fe based superconductor reported so far.

## 3.5 Discussion

### 3.5.1 Strongly anisotropic electronic properties

The previous report for powder samples of FeS found  $H_{c2}(0)$  to be 0.4 T,<sup>63</sup> which is much lower than that of FeSe and other iron-based superconductors.  $H_{c2}$  for FeSe has been reported to be 16.3 T in powder samples.<sup>13</sup> This difference between the upper critical fields in FeSe and FeS has significant effects on their coherence lengths as well.

Coherence lengths calculated from  $H_{c2}(0)$  for FeS powders<sup>63</sup> and FeSe powders<sup>13</sup> are 287 Å and 45.0 Å, respectively. We confirm Lai's report of a much lower  $H_{c2}(0)$  and higher coherence length in FeS compared to other iron-based superconductors, but also demonstrate that these properties are highly anisotropic.

As important as the comparatively smaller critical fields in FeS, the anisotropy also appears to be much larger in this system. We find an anisotropy ratio of  $\Gamma \sim 10$ , and to our knowledge this is the largest reported  $\Gamma$  yet for an iron-based superconductor. For FeTe<sub>1-y</sub>S<sub>y</sub> single crystals, the field dependence on  $T_c$  is mostly isotropic with a reported  $\Gamma = H_{c2}^{\parallel ab} / H_{c2}^{\parallel c} = 18 \text{ T} / 19 \text{ T} = 0.95$ .<sup>118</sup> Recent studies on Fe(Se<sub>1-x</sub>S<sub>x</sub>) single crystals has shown sulfur to increase  $T_c$  from 8.5 K for  $x = 0$  to 10.7 K for  $x = 0.11$ , and the anisotropy is also more pronounced in crystals with higher sulfur content as  $\Gamma = H_{c2}^{\parallel ab} / H_{c2}^{\parallel c} = 2$  for  $x = 0$  and 3.5 for  $x = 0.11$ .<sup>119</sup>

Surprisingly, in our studies of angular dependence of MR, both longitudinal and transverse rotation studies show a diminishment of MR as the field is rotated toward the crystallographic basal plane, irrespective of whether the field direction is rotated parallel or perpendicular to the current direction (Figure 3.12a,b). This is consistent with either a projection-like orbital MR of a very thin specimen (*i.e.*, with a large MR when  $H$  is perpendicular to the plane where orbital motion is allowed and zero MR when orbital motion of charge carriers is prohibited by geometric confinement), or with a very strong electronic anisotropy as found in other materials with reduced electronic dimensionality.

Given the micaceous nature of FeS single crystals, the anisotropic behavior of the MR may arise due to a microscopic physical separation of crystalline layers resulting in effectively two-dimensional layers that would act much as in a thin film. Such a descrip-

tion of our sample’s behavior would imply that it contains a slab thickness that is less than the characteristic magnetic length scale. Our studies of  $H_{c2}$  anisotropy and its angular variation (Figure 3.14) suggest that the measured superconducting state of FeS is in fact inhabiting a three-dimensional environment with strong anisotropy, given the lack of a cusp in  $H_{c2}(\theta)$  near the  $90^\circ$  field alignment (Figure 3.14). The result for our case is in good agreement with GL theory. Therefore, the appropriate length scale to consider is the superconducting coherence length which is  $104 \text{ \AA}$  for  $\xi_{H\parallel ab}$ . In other words, our single-crystal samples must entail crystalline slabs of at least  $104 \text{ \AA}$  thickness in order to exhibit the GL-type behavior of  $H_{c2}$  that follows from Eq. 2. An estimate of the mean free path of quasiparticles<sup>120</sup> yields  $l_{\text{mfp}} \approx 30 \text{ \AA}$ , which is much smaller than  $104 \text{ \AA}$ , suggesting the scattering length is at least much smaller than the known slab thickness. At the very least, the fact that the effective thickness must be at least  $\sim 20$  unit cells suggests quasiparticles are not artificially confined, and that the observed two-dimensional behavior in MR may be intrinsic to the electronic structure.

### 3.5.2 True ground and normal state properties of FeS

The tetragonal FeS system was originally predicted to be semiconductor in nature by Bertaut *et al.*<sup>90</sup> This claim was recently supported by resistivity measurements performed by Denholme *et al.*<sup>94</sup>, which showed that their samples were non-superconducting with ferrimagnetic-like behavior. Similarly, samples prepared by Sines *et al.*<sup>95</sup> were also exhibited semiconducting and ferrimagnetic behavior. Contrary to experimental evidence published before the work of Lai *et al.*,<sup>63</sup> several other groups had predicted tetragonal

FeS to be metallic.<sup>121–125</sup> Vaughan and Ridout<sup>121</sup> proposed that the bonding in the tetragonal FeS was metallic in nature due to delocalized *d* electrons in iron sublattice. Recent density functional theory (DFT) calculations also supported metallicity, in tetragonal FeS.<sup>122–124</sup>

Geochemists studying mackinawite have suggested that the ferrimagnetic-like behavior from earlier magnetization data might have arisen from the well-known thiospinel ferrimagnetic impurity, Fe<sub>3</sub>S<sub>4</sub>, considering the ease of conversion of mackinawite FeS to Fe<sub>3</sub>S<sub>4</sub>.<sup>97,98</sup> Several of our powder FeS samples prepared through the synthesis detailed by Lennie *et al.*<sup>92</sup> form with an Fe<sub>3</sub>S<sub>4</sub> impurity as revealed by combined magnetization measurements and neutron powder diffraction. Even Denholme *et al.* acknowledged that the semiconductor behavior of FeS could be attributed to the surface oxide layers of FeS, as suggested by Bertaut *et al.*<sup>90,94</sup> Indeed, similar oxidation has been observed in the FeSe system, as Greenfield *et al.*<sup>126</sup> reported that amorphous surface oxide layers of FeSe particles suppressed the superconductivity in FeSe. Our single crystal results definitively support a metallicity in the normal state properties and superconductivity in the ground state.

### 3.5.3 Structural trends concerning $T_c$

Compared to tetragonal FeSe, mackinawite FeS contains more regular tetrahedral *Ch*–Fe–*Ch* bond angles where *Ch* = chalcogenide. In FeSe, the Se–Fe–Se out-of-plane bond angle is 112.32(6)° and the Se–Fe–Se in-plane bond angle is 103.91(7)°.<sup>16</sup> The respective bond angles for our FeS powder and single crystal samples were calculated to be

close to  $108.1(3)^\circ$  and  $110.2(2)^\circ$  (Table 3.1). Several studies have suggested that higher  $T_c$  could be achieved from more regular bond angles,<sup>94</sup> as is with iron pnictide superconductors.<sup>127,128</sup> However, this structural parameter does not seem to be as important an indicator in the iron chalcogenides since FeSe exhibits a higher  $T_c$  (8 K) than FeS ( $T_c = 4$  K) even though it is comprised of more distorted tetrahedra. This suggests that structural factors controlling  $T_c$  in iron pnictides may not be identical to those of the iron chalcogenides.

Anion height has also been implicated as a reliable predictor for  $T_c$  in iron-based superconductors.<sup>128</sup> For iron pnictides,  $T_c$  increases with increasing anion height as FeP-based superconductors have lower anion height and lower  $T_c$  than FeAs-based superconductors. However,  $T_c$  begins to drop off for anion heights greater than  $1.38 \text{ \AA}$ , which suggests there is an optimal anion height for maximizing  $T_c$ . For FeSe with  $T_c = 8$  K, the Se height is  $1.45 \text{ \AA}$ , and upon application of physical pressure, the Se height decreases to  $1.425 \text{ \AA}$ , which leads to an increase in  $T_c$  up to 37 K (8 GPa).<sup>128,129</sup> For larger anions, i.e. FeTe, the anion height is larger than that of FeSe and while FeTe is not superconducting at ambient pressure isovalent anionic substitution as in  $\text{FeTe}_{0.8}\text{S}_{0.2}$  induces superconductivity (anion height =  $1.75 \text{ \AA}$ ,  $T_c = 10$  K).<sup>130,131</sup> From this anion height principle, we should expect the smaller anionic radius of sulfide to lead to a larger  $T_c$ . However, the anion height in FeS was found in the range from  $1.27(1)$  to  $1.34(1) \text{ \AA}$  (Table 3.1), which is below the optimal height of  $1.38 \text{ \AA}$ . This result for FeS could therefore explain why the  $T_c$  is remains low and between 3.5 and 5 K despite having more regular tetrahedra than FeSe or FeTe.

As a preliminary study on modifying the anion height in FeS to affect  $T_c$ , we have

performed magnetization measurements as a function applied pressure. As shown in Figure 3.15, measurements of magnetic susceptibility in a clamp-cell setup show that the transition temperature decreases with increasing pressure, at least up to 10 kbar. While it is known that  $T_c$  in the related superconductor FeSe undergoes a dramatic enhancement under pressure, the increase in  $T_c$  for FeSe occurs at much higher pressures than currently reached in the present experiment for FeS (on the order of 10 GPa). Further work to study the relation between  $T_c(P)$  and the crystallographic parameters as a function of applied pressure will shed more light on the relation between structure and superconductivity in FeS.

### 3.6 Conclusions

In conclusion, we have synthesized superconducting single crystals of FeS and characterized their thermal, magnetic, and electrical properties. The synthesis of FeS single crystals was accomplished through the novel method of reductive de-intercalation of  $K_x\text{Fe}_{2-y}\text{S}_2$  single crystals under hydrothermal conditions. The FeS crystals are stable up to 250 °C in argon and 200 °C in air. At 4 K the FeS crystals transition from a metallic, Pauli paramagnetic state to the superconducting state. In both the normal state and superconducting states, we observe a large anisotropy in the properties of FeS. The upper critical field expresses a large anisotropy with a  $\Gamma = H_{c2}^{\parallel ab}(0)/H_{c2}^{\parallel c}(0) = (2.75 \text{ T})/(0.275 \text{ T}) = 10$ , the largest reported for any iron-based superconductor thus far. Magnetoresistance measurements for the normal state performed as a function of applied field angle reveal a remarkable two-dimensional behavior in FeS. Overall, the physical property results indi-

cate that the Fermi surface of FeS may be highly two-dimensional, and perhaps even more so than other closely-related iron-based superconductors. Nevertheless, FeS appears to be a three-dimensional superconductor with highly anisotropic properties both in the superconducting and normal state. Since the metastable system, mackinawite-type FeS, is now confirmed as a superconductor and not a magnetic semiconductor, this system could be a template for the preparation of new sulfide-based superconductors that exhibit strong anisotropic behavior.

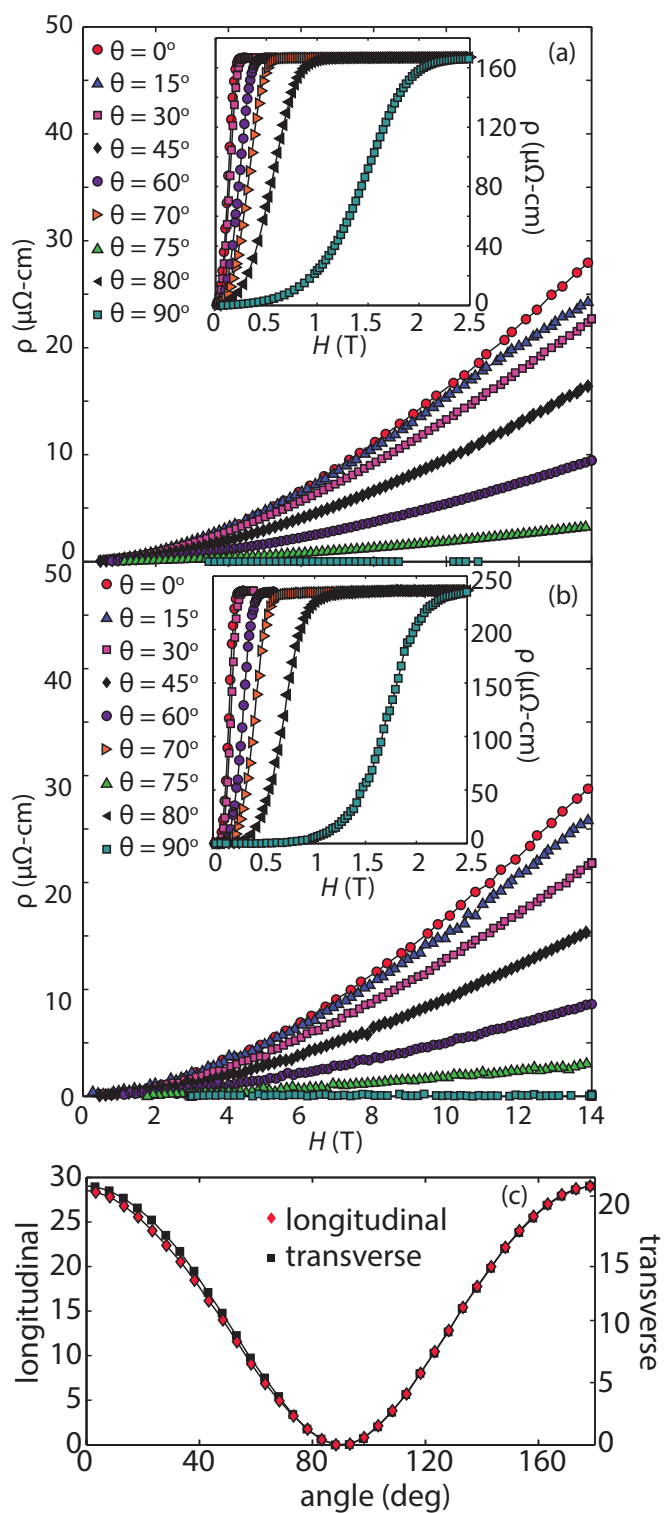


Figure 3.12: Constant temperature scans of magnetoresistance (MR) of FeS as a function of field angle  $\theta$ , defined as the deflection from  $c$ -axis direction. Angular dependence of (a) longitudinal ( $H(90^\circ) \parallel I$ ) and (b) transverse ( $H(\theta) \perp I$ ) MR taken at 1.8 K are presented. Insets in each figure display a zoom of the superconducting  $H_{c2}$  transition. (c) Comparison of angular dependence of transverse and longitudinal MR at 1.8 K and 14 T.

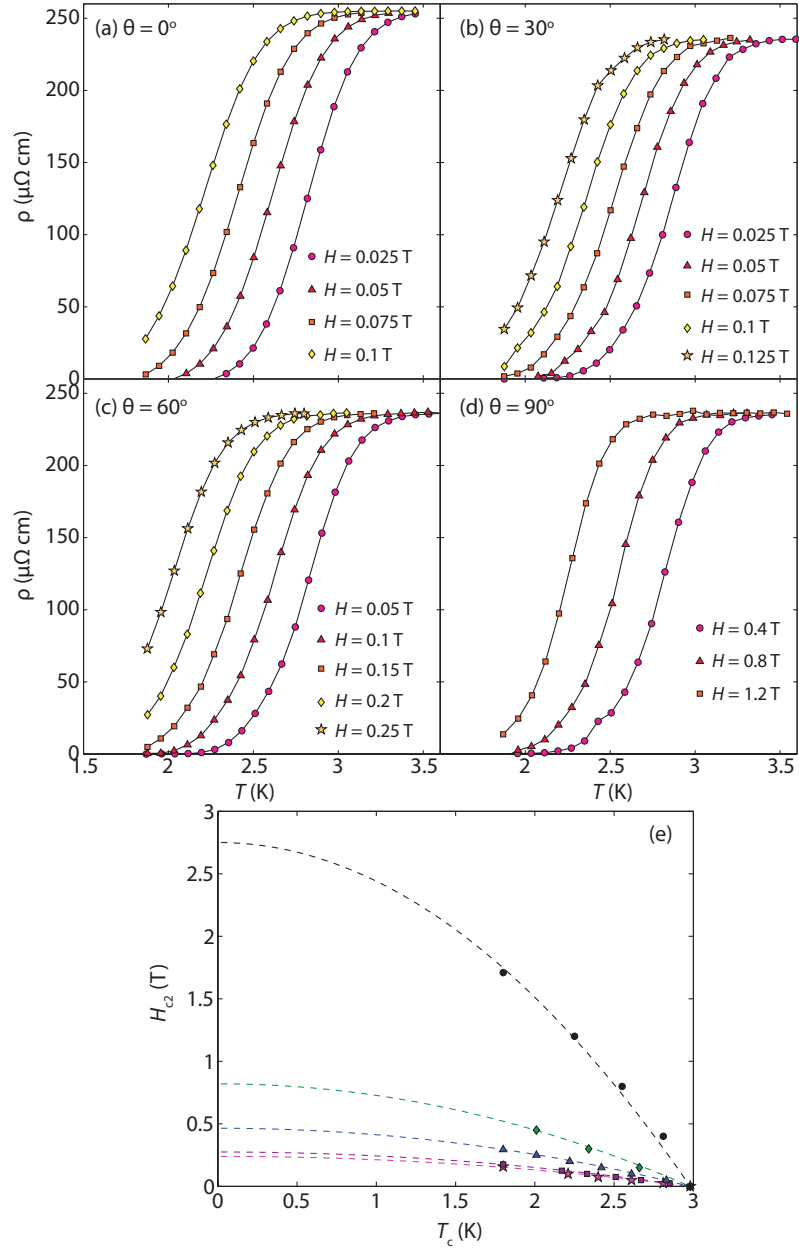


Figure 3.13: Superconducting transition of FeS single crystal as a function of magnetic field applied along different angles  $\theta$  with respect to the crystallographic  $c$ -axis (transverse to current direction). Panel e) presents the compiled  $H_{c2}(\theta)$  temperature dependences for all angles measured.  $T_c$  values were determined by the resistance transition midpoint. Solid lines represent the WHH orbital pair-breaking expectation for  $H_{c2}(T)$  in each case (see text for details).

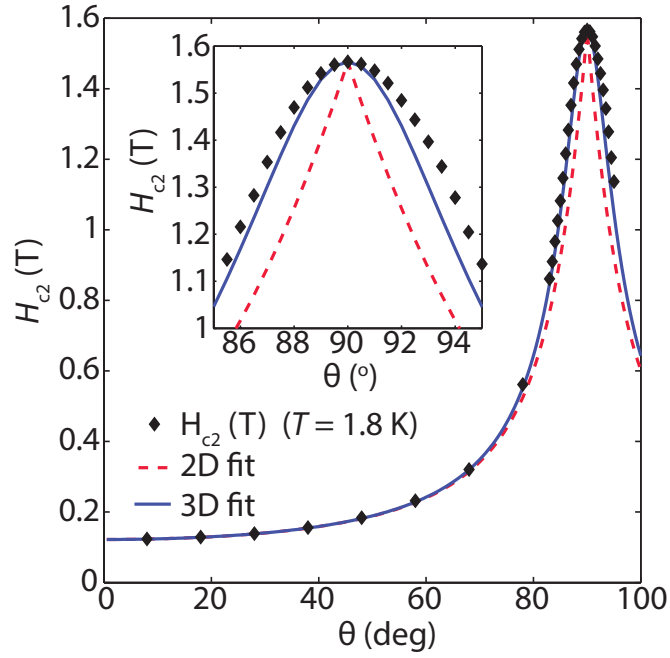


Figure 3.14: Angular dependence of the superconducting upper critical field  $H_{c2}$  at 1.8 K. Black diamonds represented measured transition fields (defined as the resistive transition midpoint), and lines represent fits to the theoretical expectation for the angular dependence: solid line represents the Ginzburg Landau expectation for a 3D system with anisotropic effective mass, and dashed line represents the Tinkham's model expectation for 2D superconductors. Inset displays zoomed data near  $90^\circ$  ( $H \parallel ab$ ). All data were collected with magnetic field direction always transverse to the current direction.

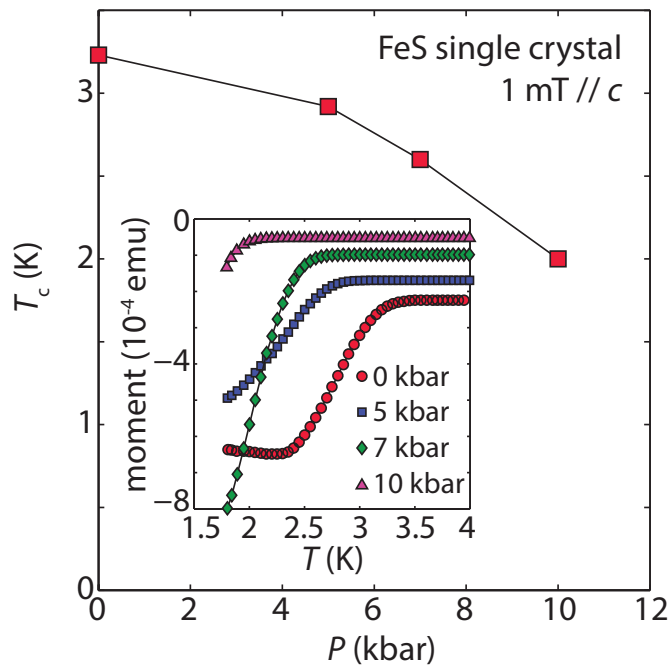


Figure 3.15: Applied pressure dependence of the superconducting transition temperature of an FeS crystal as extracted from magnetic susceptibility measurements performed using a BeCu piston-cylinder clamp cell. Inset displays the measured susceptibility data (presented with a vertical offset for clarity). Pressure values are determined at room temperature.

## **Chapter 4: Metastable Layered Cobalt Chalcogenides from Topochemical Deintercalation**

The work described within this chapter was published in *Journal of the American Chemical Society* **2016**, *138*, pg. 16432. Brandon Wilfong, Hector Vivanco, John-pierre Paglione, Craig M. Brown, and Efrain Rodriguez were contributing authors of the manuscript. X.Z., B.W. and H.V. prepared the samples, X.Z. performed MPMS measurements and DFT calculations, B.W. collected resistivity data, X.Z., B.W., and C.M.B. collected the neutron data.

### **4.1 Introduction**

To advance the first-principles approach towards materials discovery<sup>132,133</sup>, we must also develop new synthetic strategies for finding functional materials. One outstanding issue is that many predicted inorganic materials, especially extended solids, may not be thermodynamically favored. A solution to this problem is to kinetically stabilize such predicted compounds, *i.e.* to isolate the metastable phases. Inspired by recent work on finding metastable and superconducting iron chalcogenides,<sup>13,63</sup> we present topochemical methods to find metastable phases of cobalt chalcogenides that have been theoretically predicted but heretofore never synthesized. Through topochemical means, we preserve

the underlying layered structure by the kinetic removal (or insertion) of structural motifs from the thermodynamically stable phases.

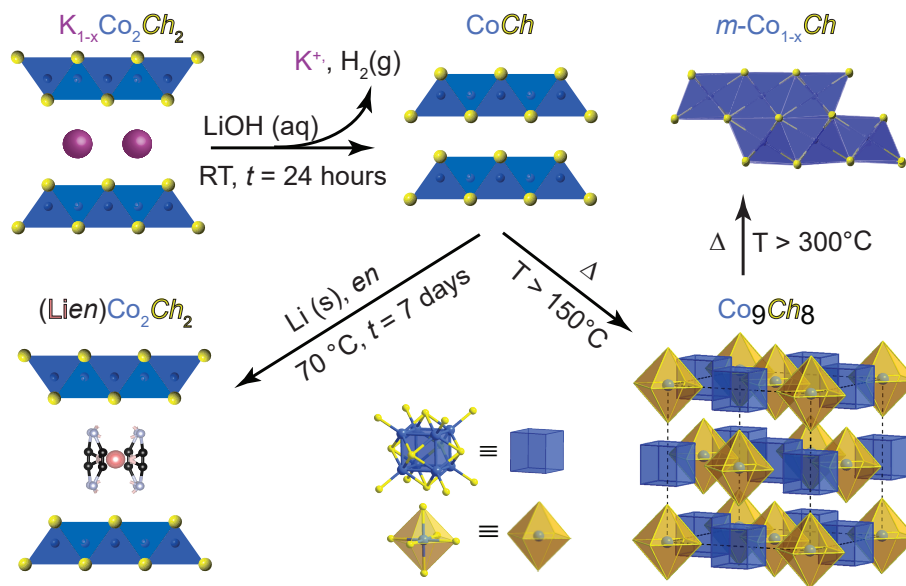


Figure 4.1: Reaction schemes for the manipulation of cobalt chalcogenides. From the thermodynamically stable  $K_xCo_2Ch_2$  phases, we prepare metastable tetragonal  $CoCh$  and  $(Lien)CoCh$  where  $en$ =ethylenediamine. Upon applying heat to the metastable phases, pentlandite ( $Co_9Se_8$ ) is prepared followed by the NiAs-derivative  $m-Co_{1-x}Ch$ .

In this study, we target topochemical de-intercalation of extended solids with the stoichiometry  $A_xM_2Ch_2$  where  $A$  = alkali metal,  $M$ =transition metal, and  $Ch$  is a chalcogenide that crystallize with the  $ThCr_2Si_2$ -type structure. The Inorganic Crystallographic Structural Database (ICSD) lists close to 1,865 compounds with the  $ThCr_2Si_2$ -type structure, of which approximately 40 are chalcogenides. Just as perovskite-derived metal oxides have been utilized for topochemical conversion to metastable oxides,<sup>134–137</sup>  $ThCr_2Si_2$ -derived chalcogenides (and pnictides) can be the basis for new metastable non-oxides. Greenblatt *et al.* have already developed effective and straight-forward methods to synthesize a variety of ternary or quaternary chalcogenides with this structure type.<sup>138–140</sup> Recently, we have demonstrated that *chemie douce* methods can be applied to such structures

to produce iron-based superconductors such as FeS,<sup>141</sup>  $(\text{Li}_{1-x}\text{Fe}_x\text{OH})\text{FeSe}$ ,<sup>53</sup>  $[\text{Na}_{1-x}\text{Fe}_x(\text{OH})_2]\text{FeS}$ , and  $(\text{Li}_{1-x}\text{Fe}_x\text{OH})\text{FeS}$ .<sup>142</sup>

Until now, iron has been found to be the only transition metal to form stable binary chalcogenides with the anti-PbO type structure. In compounds such as tetragonal mackinawite FeS and  $\beta$ -FeSe, the  $\text{FeCh}_4$  tetrahedra edge-share to form two-dimensional (2D) layers held by weak van der Waals interactions. Therefore, in addition to superconductivity, another appealing feature of the layered chalcogenides is their ability to act as hosts for intercalation chemistry<sup>50</sup>. In the FeSe case, its  $T_c$  can be increased from 8 K<sup>13</sup> to  $\approx 43$  K by intercalating either cationic species<sup>20,45</sup> or layers such as  $(\text{Li}_{1-x}\text{Fe}_x\text{OH})$ <sup>24,26</sup>. Therefore, we have decided to test our topochemical method by focusing on cobalt in order to also help answer the question of what makes iron so special for superconductivity in these layered materials.

First, we highlight the de-intercalation reaction of Fig. 4.1 to synthesize the hypothesized metastable tetragonal CoS and CoSe phases. Then, we will demonstrate how these new tetragonal phases, much as in the layered FeCh compounds, can serve as hosts for intercalation chemistry by using Li-ethylenediamine (Li-en) as a guest species (Fig. 4.1). We characterize the physical properties of these metastable phases and demonstrate that changing the symmetry, metal oxidation state, and electronic configuration have a profound effect on the physical properties of these materials. Similarly, Shatruk and co-workers have reported drastic change of magnetic ordering of Co sublattice by electron doping for the  $\text{ThCr}_2\text{Si}_2$ -type layered rare-earth ( $R$ ) cobalt pnictides ( $Pn$ ),  $R\text{Co}_2Pn_2$ .<sup>143–147</sup> Finally, we use *ab initio* calculations to explain why the topochemical approach is necessary and successful for the preparation of CoCh phases. We find that the application of

bonding analysis<sup>148,149</sup> to our solid state structures not only aids the interpretation of the first principles calculations, but also improves our predictive capability for finding new functional materials.

## 4.2 Experimental

### 4.2.1 Sample synthesis

Binary anti-PbO type CoSe and CoS single crystals and powders were prepared by de-intercalation of interlayer potassium cations from  $\text{KCo}_2\text{Se}_2$  and  $\text{KCo}_2\text{S}_2$  by a topochemical approach. For the synthesis of  $\text{KCo}_2\text{Se}_2$  (or  $\text{KCo}_2\text{S}_2$ ), 1:1 stoichiometric ratios of hexagonal CoSe (or CoS) were mixed with potassium metal (Sigma Aldrich 99.5%) and loaded into a quartz ampoule inside an argon-filled glovebox. The mixture was sealed using a double-ampoule technique, a bigger ampoule enclosing a smaller ampoule containing the mixture, to avoid oxidation, and heated to 1050 °C at a rate of 10 °C/hour and held at this temperature for five hours to form a congruent melt. Afterwards, the melt was slowly cooled at a rate of 5 °C/hour to 450 °C to allow for crystal growth. Upon recovery,  $\text{KCo}_2\text{Se}_2$  appeared as golden plate-like crystals and  $\text{KCo}_2\text{S}_2$  golden polycrystalline material.

Two methods were employed to yield the tetragonal CoSe and CoS. First,  $\text{KCo}_2\text{Se}_2$  or  $\text{KCo}_2\text{S}_2$ , crystals or powders respectively, were placed into ~ 10 mL of saturated LiOH solution, made by dissolving  $\text{LiOH} \cdot \text{H}_2\text{O}$  (Alfa Aesar 98%) in water. The mixtures were then placed in a vial for ultrasonication in a water bath for approximately one hour. After one hour, the contents were centrifuged and washed thrice to yield black powders.

Another method was employed for the  $\text{KCo}_2\text{Se}_2$  single crystals without the use of ultrasonication to avoid excessive break up of the crystallites.  $\text{KCo}_2\text{Se}_2$  single crystals were added to  $\sim 20$  mL of saturated LiOH or ammonia solution in a flask, placed on a Schlenk line under argon gas and stirred for approximately one day. Shiny silver flaky crystals were recovered, washed and dried under vacuum. The highly basic solutions during the de-intercalation reactions stabilize  $\text{Se}^{2-}$  anions over the formation of  $\text{H}_2\text{Se}$  and  $\text{HSe}^-$  species in solution, and subsequently prevented dissolution of the selenide layers. The de-intercalation reaction dynamics as a function of pH are discussed in more detail in our earlier work<sup>53</sup>.

## 4.2.2 Characterization methods

Powder X-ray diffraction (PXRD) data was collected using a Bruker D8 X-ray diffractometer with  $\text{Cu K}\alpha$  radiation,  $\lambda = 1.5406 \text{ \AA}$  (step size =  $0.020^\circ$ ). Low temperature (3 K) diffraction data for CoSe were collected on the BT-1 high-resolution neutron powder diffraction (NPD) with the Ge(311) monochromator ( $\lambda = 2.0790 \text{ \AA}$ ) at the NIST Center for Neutron Research. Temperature dependent PXRD on ground crystals of CoSe was performed using a Bruker C2 diffractometer with a Vantec500 2D detector,  $\lambda = 1.5406 \text{ \AA}$  (step size =  $0.015^\circ$ ,  $2\theta = 13.5^\circ - 74^\circ$ ). The sample was heated using an Anton Paar DHS 1100 graphite-dome stage with heating from  $27^\circ \text{ C}$  to  $600^\circ \text{ C}$  under Ar flow to determine stability of the tetragonal CoSe phase. Rietveld and Pawley refinements with all the diffraction data were carried out using the TOPAS 4.2 software<sup>66</sup>.

Elemental analysis was performed using scanning electron microscopy (SEM) on a

Hitachi SU-70 Schottky field emission gun SEM with an equipped Bruker Quantax energy dispersive X-ray detector. Energy dispersive X-ray spectroscopy (EDS) was carried out at 15 keV. Inductively coupled plasma atomic emission spectroscopy (ICP-AES) data were collected using an Shimadzu ICPE-9000 spectrometer. Standards used for ICP-AES were diluted from 1000 ppm of respective elements purchased from FLUKA.

All magnetic susceptibility measurements were carried out using a Quantum Design Magnetic Susceptibility Measurement System (MPMS)<sup>1</sup> on powder samples of  $\text{KCo}_2\text{Se}_2$ ,  $\text{KCo}_2\text{S}_2$ , and tetragonal CoSe and CoS. Field-cooled (FC) and zero field-cooled measurements (ZFC) were taken from 1.8 K to 300 K with various applied magnetic fields. Magnetic hysteresis measurements were taken at a series of temperatures, (1.8 K, 60 K, and 120 K) with applied magnetic field between  $H = \pm 7$  T.

Electrical transport measurements were performed using a 9 T Quantum Design Physical Property Measurement System (PPMS-9). Single crystals of CoSe were mounted on a Quantum Design DC resistivity puck. Thin gold wires were attached to the crystal to form electrical contacts via silver paste. An applied current of 0.1 mA with frequencies near 10 Hz was utilized.

### 4.2.3 Computational methods

All density functional theory (DFT)<sup>72,73</sup> calculations were performed by using the Vienna Ab-initio Simulation Package (VASP)<sup>74-77</sup> software package with potentials using the projector augmented wave (PAW)<sup>78</sup> method. The exchange and correlation functional

---

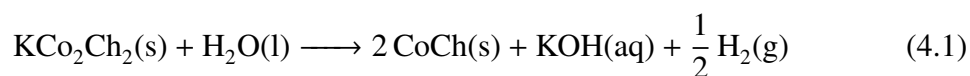
<sup>1</sup>Certain commercial equipment, instruments, or materials are identified in this document. Such identification does not imply recommendation or endorsement by the National Institute of Standards and Technology nor does it imply that the products identified are necessarily the best available for the purpose

were treated by the generalized gradient approximation (PBE-GGA).<sup>79</sup> The cut-off energy, 450 eV, was applied to the valence electronic wave functions expanded in a plane-wave basis set for all chalcogenides. A Monkhorst-Pack<sup>80</sup> generated 23×23×17 k-point grid was used for the Brillouin-zone integration to obtain accurate electronic structures. Crystal orbital Hamilton populations (COHP) were extracted using the program Local-Orbital Basis Suite Towards Electronic-Structure Reconstruction (LOBSTER) developed by Dronskowski et al<sup>81–84</sup>. COHP provides an intuitive chemical bonding analysis to the calculated electronic structures.

## 4.3 Results

### 4.3.1 Topochemical De-intercalation

As illustrated in Fig. 4.1, the topochemical de-intercalation process leading to anti-PbO type *CoCh* (**2**) is traced in the reaction from **1** to **2**. In this process,  $\text{KCo}_2\text{Ch}_2$  reacts with water to form  $\text{H}_2$  gas and KOH, and this reaction is depicted below.



The reaction for the kinetic study was carried out in water without LiOH. During the de-intercalation of the sample in water, we observed the evolution of gas bubbles, which are more rigorous when ultrasonication is applied. When the de-intercalation was complete, the pH of the filtered solution was highly basic, suggesting the formation of KOH by the reduction of water.

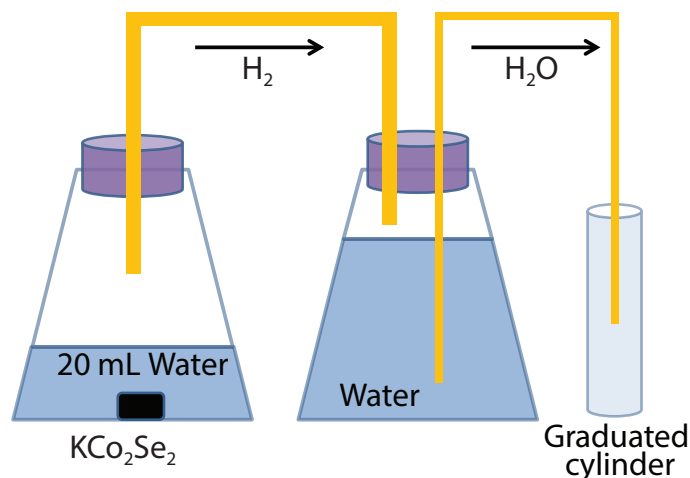


Figure 4.2: Diagram for experimental set-up of a hydrogen trap during the de-intercalation reaction of  $K_{1-x}Co_{2-y}Se_2$ . The amount of hydrogen generated during this reaction will expel equal volume amount of water to the graduated cylinder. By measuring the hydrogen generation as a function of time, a semi-quantitative analysis can be achieved.

The evolution of the hydrogen gas allowed us to study the reaction rate for the formation of the metastable  $CoCh$  phases. A semi-quantitative experiment measuring the volume of hydrogen gas evolved was set up by connecting two Erlenmeyer flasks – one as the reaction flask and the other as the  $H_2$  measurement flask (Fig. 4.2). The two flasks were tightly sealed, so that hydrogen generated in the reaction flask could only flow into the capturing flask, which expelled an equal volume amount of water. The expelled water was collected in a graduated cylinder via a cannula and measured as a function of time.

From Eqn. 4.1 we express the reaction rate as  $r = d[KOH]/dt = 2[H_2]/dt$ . Approximating the molar volume of  $H_2$  gas with that of an ideal gas, we can then relate the value of molar concentration  $[KOH]$  generated to the volume of expelled water.

$$n_{KOH} = \frac{2V_{H_2}}{22.4 \text{ L mol}^{-1}} \quad (4.2)$$

$$[KOH] = \frac{V_{H_2O}}{V_{sol} \times 11.2 \text{ L mol}^{-1}} \quad (4.3)$$

where  $V_{H_2}$  and  $V_{H_2O}$  are volumes of hydrogen gas generated and water expelled, respectively,  $V_{sol}$  the volume of the de-intercalation solution, and  $n_{KOH}$  is the number of moles of KOH. Since the reactants include an insoluble solid and the solvent (i.e. water), then a plausible rate law could be written in terms of the molar concentration of the products  $[H_2]$  or  $[KOH]$ . The amount of water expelled was observed to have a  $t^{1/2}$  behavior as shown in Fig. 4.3, which would be consistent with a rate law that has the form  $r = k/[KOH]$ . A derivation of this proposed rate law from the  $t^{1/2}$  dependence is described below.

$$r = \frac{k}{[KOH]} \quad (4.4)$$

$$\frac{d[KOH]}{dt} = \frac{k}{[KOH]} \quad (4.5)$$

$$\int_{[KOH]_0}^{[KOH]} [KOH]d[KOH] = \int_0^t kdt \quad (4.6)$$

$$\frac{1}{2}[KOH]^2 = kt \quad (4.7)$$

$$[KOH] = \sqrt{2kt} \quad (4.8)$$

The results from the semi-quantitative analysis of the reaction kinetics confirm that the de-intercalation of  $KCO_2Se_2$  involves the hydration of  $K^+$  cations and the transfer of

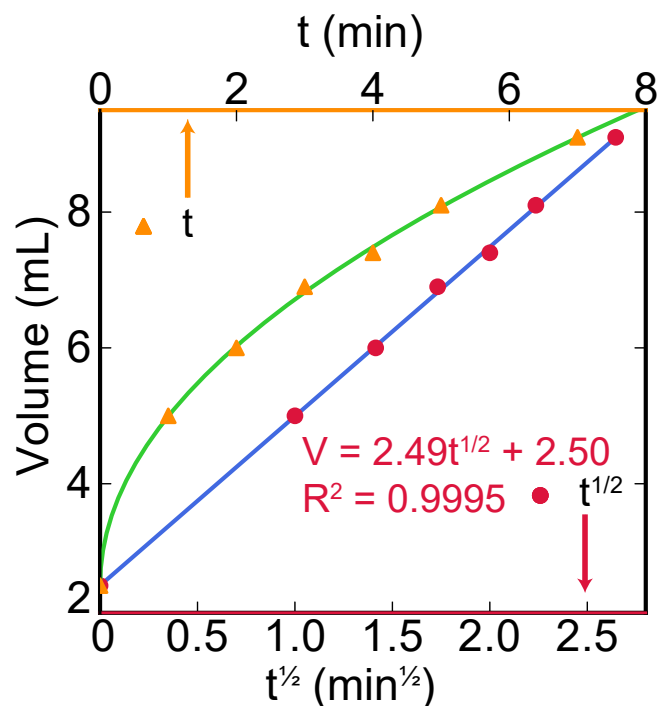


Figure 4.3: Volume of hydrogen generated during a de-intercalation reaction of  $\text{KCo}_2\text{Se}_2$  vs. time  $t$  and  $t^{1/2}$  leading to the preparation of pure  $\text{CoSe}$ . For this reaction,  $t = 0$  is the point when water flow was observed from  $\text{H}_2$  generation. The lines drawn represent a least square fit of the data.

electrons between  $\text{Co}^{1.5+}$  centers and  $\text{H}_2\text{O}$  molecules to evolve  $\text{H}_2$  gas and  $\text{OH}^-$  groups.

We postulate that the de-intercalation reaction is in part driven by the oxidation of  $\text{Co}^{1.5+}$ , and since the reaction conditions are mildly oxidative at room temperature, no major structural reconstruction of the chalcogenides occurs. Therefore, the sheets of edge-sharing  $\text{CoCh}_4$  tetrahedra in  $\text{KCo}_2\text{Ch}_2$  are retained, but the layers does undergo a rearrangement from the body-centered to the primitive setting. Overall, kinetically controlled topochemical de-intercalation leads to the first isolation of anti-PbO type  $\text{CoSe}$  and  $\text{CoS}$ .

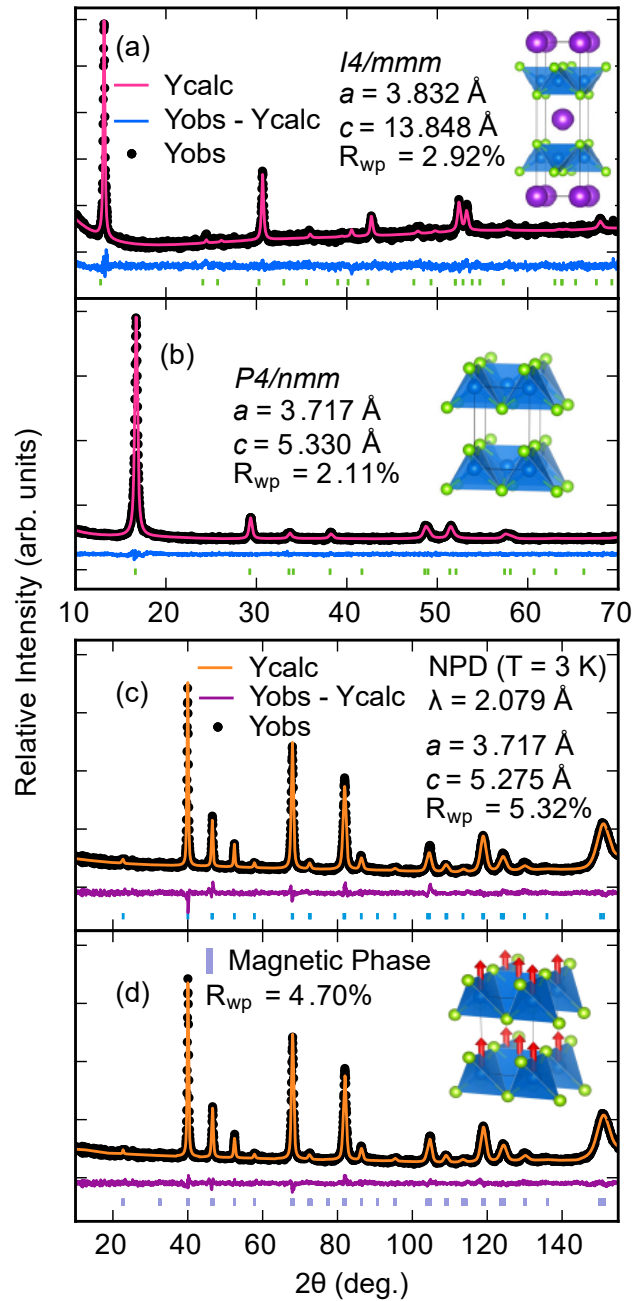


Figure 4.4: Powder X-ray diffraction patterns with  $\text{Cu } K\alpha$  radiation of (a)  $\text{KCo}_2\text{Se}_2$  in the body-centered tetragonal structure ( $I4/mmm$ ) at room temperature and (b)  $\text{CoSe}$  with a primitive tetragonal structure ( $P4/nmm$ ) at room temperature. (c) Neutron powder diffraction (NPD) pattern of  $\text{CoSe}$  at 3 K (BT-1, NIST). (d) The NPD pattern but with the addition of the ferromagnetic phase with the moment on the Co site pointing in the  $c$ -direction as shown in the inset. Tick marks representing the corresponding tetragonal phases are shown below the calculated, observed, and differences curves from Rietveld analysis.

Table 4.1: Structural parameters for ground single crystals of  $\text{KCo}_2\text{Se}_2$  and  $\text{CoSe}$ . Structures are for room temperature PXRD data and 3 K NPD data. All relevant bond angles and distances from the refinements are given. Standard uncertainties given in parantheses indicate one standard deviation.

KCo <sub>2</sub> Se <sub>2</sub> (298 K, PXRD), <i>I4/mmm</i> , $R_{wp} = 2.917\%$						
$a = 3.832(2) \text{ \AA}, c = 13.848(3) \text{ \AA}$						
atom	Site	x	y	z	Occ.	$U_{iso} (\text{\AA}^2)$
K1	2a	0	0	0	0.94(6)	0.109(22)
Co1	4d	0	0.5	0.25	0.96(6)	0.060(11)
Se1	4e	0	0	0.359(3)	1	0.019(4)
Co-Se (Å)	Se-Co-Se (°)	Se-Co-Se (°)	Co-Co (Å)	anion height (Å)		
2.442(6)	103.4(4)	112.6(2)	2.710(3)	1.509(3)		
CoSe (298 K, PXRD), <i>P4/nmm</i> , $R_{wp} = 2.102\%$						
$a = 3.717(3) \text{ \AA}, c = 5.330(3) \text{ \AA}$						
atom	Site	x	y	z	Occ.	$U_{iso} (\text{\AA}^2)$
Co1	2a	0	0	0	1	0.012(3)
Se1	2c	0	0.5	0.265(5)	1	0.010(3)
Co-Se (Å)	Se-Co-Se (°)	Se-Co-Se (°)	Co-Co (Å)	anion height (Å)		
2.332(2)	111.382(63)	105.8(2)	2.6284(3)	1.412(3)		
CoSe (3 K, NPD), <i>P4/nmm</i> , $R_{wp} = 5.318\%$						
$a = 3.716(6) \text{ \AA}, c = 5.275(1) \text{ \AA}$						
atom	Site	x	y	z	Occ.	$U_{iso} (\text{\AA}^2)$
Co1	2a	0	0	0	1	0.0026(8)
Se1	2c	0	0.5	0.269(2)	1	0.0020(5)
Co-Se (Å)	Se-Co-Se (°)	Se-Co-Se (°)	Co-Co (Å)	anion height (Å)		
2.339(5)	111.632(36)	105.232(68)	2.6280	1.412(3)		

### 4.3.2 Crystallography, chemical composition, and thermal stability

Comparisons of the PXRD patterns of ground single crystals of  $\text{KCo}_2\text{Se}_2$  and  $\text{CoSe}$  are shown in Fig. 4.4, and the NPD results are shown in Fig. 4.4c. PXRD patterns of the sulfide analogues are shown in Fig. 4.5. As seen from both the X-ray and neutron data, the crystal structures of both de-intercalated  $\text{CoSe}$  and  $\text{CoS}$  can be fit well with the anti-PbO type structure, which has the primitive space group *P4/nmm*. Detailed structural information extracted by Rietveld refinements of PXRD and NPD for the selenides are reported in Table 4.1.

Elemental analysis from EDS gave a Co:Se ratio close to 0.94:1 (Table 4.2), but the more accurate ICP-AES measurement gave a composition of  $\text{Co}_{0.98\pm 0.02}\text{Se}$ . Therefore, while it is likely that the starting compositions of  $\text{KCo}_2\text{Se}_2$  could have some vacancies on the cobalt site, our resulting CoSe products show little evidence for significant vacancies on the Co site. Furthermore, for CoSe no residual potassium could be detected by EDS, suggesting complete de-intercalation. For CoS, however, about 4.5 at% of potassium was measured by EDS (Table 4.2). While the residual potassium in CoS could be further reduced by longer reaction time with ultrasound, this usually resulted in worse crystallinity in the products.

Table 4.2: Elemental analysis of newly synthesized anti-PbO type CoSe and CoS using scanning electron microscopy (SEM) and energy dispersive X-ray spectroscopy (EDS). EDS was carried out at 15 keV.

CoSe (298 K, ground single crystal) , 15eV EDS				
Element	Series	Norm. Percent (wt. %)	Norm. Percent (at. %)	Error [ $3\sigma$ ] (wt. %)
Cobalt	L-series	41.30	48.53	4.00
Selenium	K-series	58.70	51.47	9.22
CoS (298 K, ground polycrystalline material) , 15eV EDS				
Element	Series	Norm. Percent (wt. %)	Norm. Percent (at. %)	Error [ $3\sigma$ ] (wt. %)
Cobalt	K-series	64.41	50.11	6.16
Sulfur	K-series	31.73	45.37	3.52
Potassium	K-series	3.85	4.52	0.49

Although CoSe and CoS have been prepared for the first time in their tetragonal form, the sulfide appears to be less stable than the selenide. In addition to its poor crystallinity (Fig. 4.5), certain ( $hk0$ ) reflections are missing for CoS, which indicates some disorder within its  $ab$  plane. For longer de-intercalation reactions, up to 5 hours under ultrasonication, the as-recovered CoS sample was amorphous as no Bragg reflection could

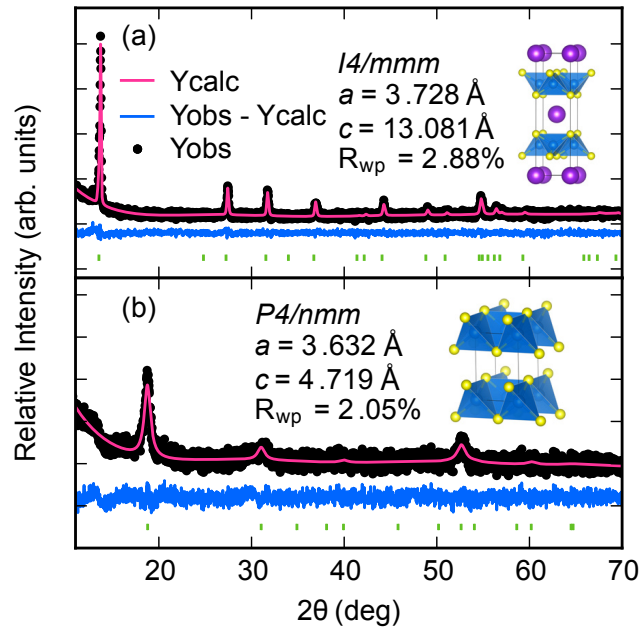


Figure 4.5: Powder X-ray diffraction patterns with Cu  $K\alpha$  radiation of (a)  $KCo_2S_2$  and (b)  $CoS$  collected at room temperature. Tick marks representing the corresponding tetragonal phases are shown below the calculated, observed, and differences curves from Rietveld analysis for (a) and Pawley fit for (b).

be identified. Contrastingly, prolonged reactions for  $CoSe$  samples led to no noticeable changes in its crystallinity. Our results suggest that anti-PbO type  $CoS$  can be stabilized kinetically, but it is much less stable than the selenide analogue.

In order to exploit tetragonal  $CoSe$  as an intercalation host, temperature dependent PXRD was carried out to examine its thermal stability. Powders of ground single crystals of  $CoSe$  were heated from 27 °C to 600 °C, and the evolution of the PXRD patterns is shown in Fig. 4.6. Upon heating to 200 °C, the tetragonal  $CoSe$  ( $P4/nmm$ ) completely transformed to cubic cobalt seleno-pentlandite ( $Co_9Se_8$ ,  $Fm\bar{3}m$ , Fig. 4.1). Around 400 °C, the cubic  $Co_9Se_8$  phase started to convert to a monoclinic phase ( $Co_3Se_4$ ,  $C2/m$ ), a distorted and vacancy-ordered NiAs-type (Fig. 4.1). This monoclinic phase persisted to 600 °C and remained the major phase when cooled back to room temperature.

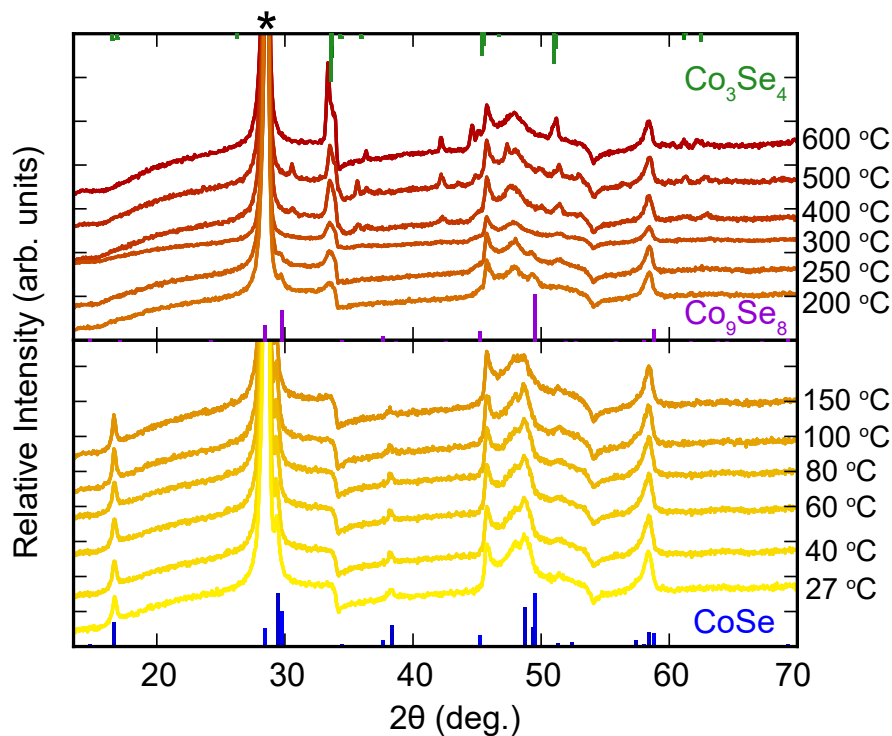


Figure 4.6: Temperature evolution of the x-ray powder diffraction of ground single crystals of CoSe from 27 °C to 600 °C performed using an Anton Paar DHS 1100 graphite-dome stage. Two phase transitions are observed. CoSe ( $P4/nmm$ ) starts to transform to  $\text{Co}_9\text{Se}_8$ , the cobalt pentlandite system ( $Fm\bar{3}m$ ), around 200 °C. Around 400 °C,  $\text{Co}_9\text{Se}_8$  begins to transition to the  $\text{Co}_3\text{Se}_4$ , the monoclinic distortion of the NiAs-type ( $C2/m$ ). Tick marks represent the corresponding phases as labeled. The (\*) symbol shows peak introduced by the Anton Paar DHS 1100 graphite-dome stage used to heat the sample.

The results between 200 °C and 600 °C are in good agreement with the phase diagram of the Co-Se system<sup>150</sup>. The transformation from tetragonal CoSe to the  $\text{Co}_9\text{Se}_8$  pentlandite structure between 150 °C and 200 °C suggests that any intercalation reactions of the anti-PbO type CoSe need to be limited to below 200 °C in order to avoid structural reconstruction of the selenide sublattice.

Although pentlandite-type  $\text{Co}_9\text{Se}_8$  exists on the Co-Se phase diagram below 400 °C, it is unusual to prepare it by direct phase transformation as it has very limited window of phase stability<sup>150</sup>. For an approximately 1:1 Co/Se ratio, the NiAs type variant

is favored thermodynamically from room temperature to about 1100 °C. In fact, octahedral coordination of  $\text{Co}^{2+}$  in selenides dominates most regions of the phase diagram as in the NiAs and pyrite-type structures. Therefore, predominately tetrahedrally coordinated cobalt in pentlandite can only be formed by annealing samples at 400 °C within a narrow compositional window<sup>151</sup>. It is likely that the transformation from anti-PbO type CoSe to pentlandite is kinetically favored since it does not require overcoming the high energy barrier associated with changing coordination geometry of cobalt. Therefore, the monoclinic phase exists as a thermodynamic sink, and once formed, it does not revert back to the pentlandite structure when cooling from 600 °C to room temperature.

### 4.3.3 Magnetic properties

Upon de-intercalation of potassium from  $\text{KCo}_2\text{Se}_2$  to form CoSe, a drastic change was observed in their respective magnetic properties (Fig. 4.7).  $\text{KCo}_2\text{S}_2$  displays temperature independent magnetic susceptibility above 85 K indicative of Pauli paramagnetism. Below, 85 K, the magnetization diverges and appears to be ferromagnetic with a Curie temperature ( $T_C$ ) near 82 K. For completely de-intercalated CoSe, its  $T_C$  decreased to about 10 K and its response to magnetic field became significantly weaker compared to  $\text{KCo}_2\text{Se}_2$ . The previous report by Yang *et al.* showed  $\text{KCo}_2\text{Se}_2$  to have a  $T_C = 74$  K,<sup>152</sup> which might indicate that the amount of potassium in the lattice, and hence the electron filling level, influences the magnetic properties.

To shed more light on this it is useful to briefly discuss the recent studies on  $\text{RCo}_2\text{P}_2$  phases where  $R$ = rare earth. These isostructural cobalt phosphides are thought to display

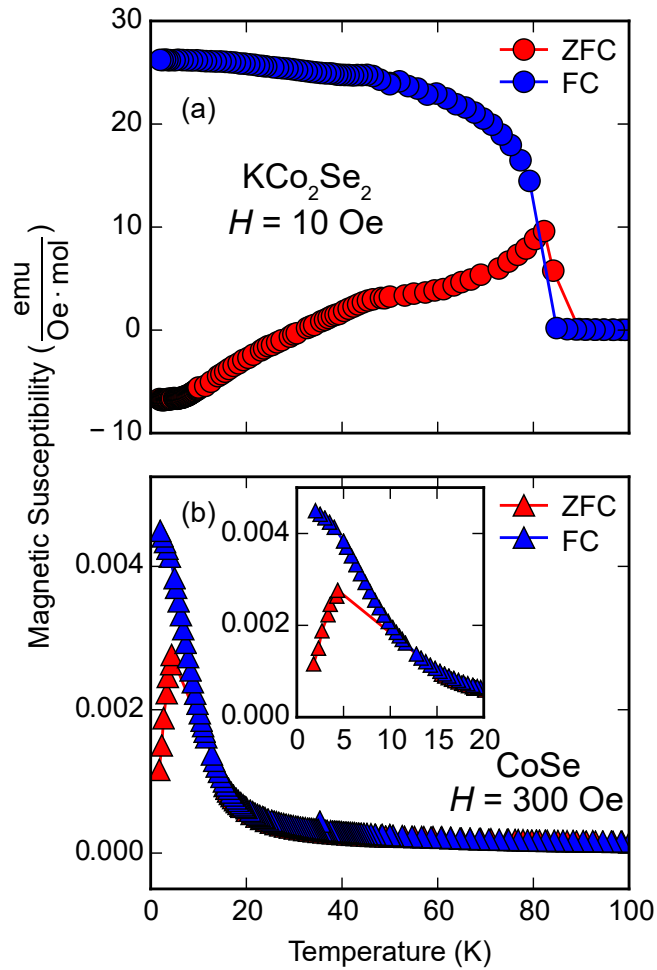


Figure 4.7: Magnetic susceptibility of (a)  $\text{KCo}_2\text{Se}_2$  and (b)  $\text{CoSe}$ , vs. temperature measured in applied field of 10 Oe and 300 Oe respectively. (a)  $\text{KCo}_2\text{Se}_2$  displays a ferromagnetic transition at  $T_C = 82$  K and (b)  $\text{CoSe}$  a  $T_C = 10$  K; the inset shows zoomed-in region near  $T_C$ .

charge transfer from the rare-earth  $4f$  shell to the Co  $3d$  level, which alters the magnetic behavior of Co square sublattice.<sup>143–145</sup> In our selenide samples, the formal oxidation state of Co changes from approximately +1.5 in  $\text{KCo}_2\text{Se}_2$  to +2 in  $\text{CoSe}$ . This indicates that charge transfer from the K cations effectively enhances ferromagnetism in the Co sublattice and raises its  $T_C$ . Furthermore, an increase in  $T_C$  has also been observed when the Co-Co distance in  $\text{La}_{1-x}\text{Pr}_x\text{Co}_2\text{P}_2$  is increased.<sup>143,153</sup> We observe the same trend in the

cobalt selenides as the Co-Co distance increases from 2.6284(3) Å in CoSe to 2.710(3) Å in  $\text{KCo}_2\text{Se}_2$ . Therefore, it seems plausible that the electronic structure responsible for ferromagnetism is heavily influenced by both the metal-metal distances in the square lattice and the transition metal's electron configuration.

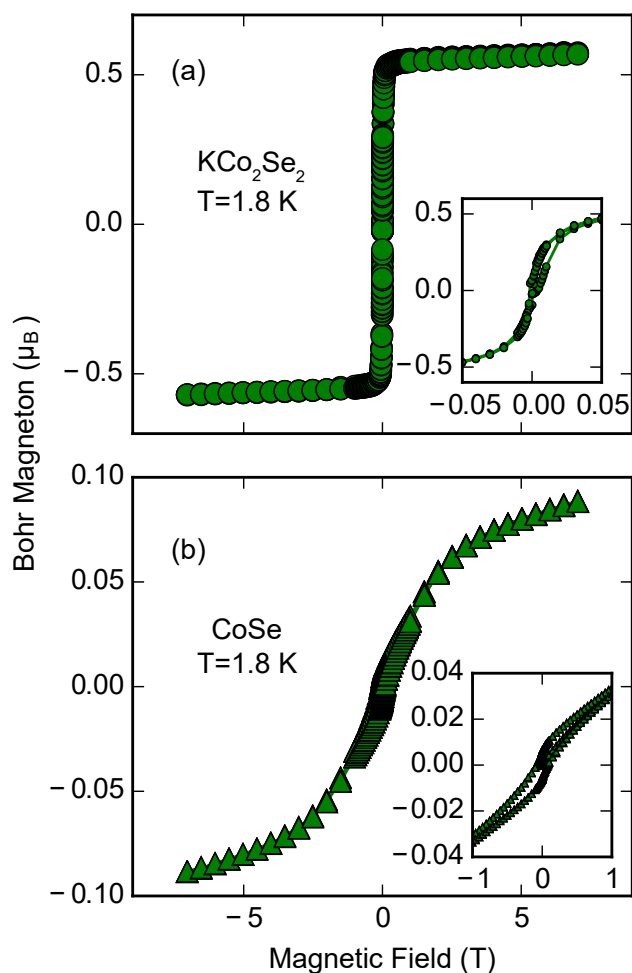


Figure 4.8: Isothermal magnetization vs. applied field  $H$  for (a)  $\text{KCo}_2\text{Se}_2$  and (b) CoSe at 1.8 K. Both  $\text{KCo}_2\text{Se}_2$  and CoSe show hysteretic behavior indicating ferromagnetic ordering.

The differences between  $\text{KCo}_2\text{Se}_2$  and CoSe were further elaborated by their respective isothermal magnetization measurements (Fig. 4.8).  $\text{KCo}_2\text{Se}_2$  demonstrates clear hysteretic behavior indicative of the ferromagnetic ordering at low temperature. Similar

to the work of Yang *et. al*<sup>152</sup>, we observe a small coercive field and complete saturation of the magnetization in  $\text{KCo}_2\text{Se}_2$ , approaching a value of  $0.6 \mu_B/\text{Co}$ , whereas for  $\text{CoSe}$ , no saturation was observed for a field up to 7 T. In addition,  $\text{CoSe}$  seems to carry a much smaller moment of  $\approx 0.1 \mu_B/\text{Co}$  at  $H = 7$  T. The lack of complete saturation to the expected  $3 \mu_B$  for a tetrahedral  $\text{Co}^{2+}$  crystal field can be attributed to the itinerant character of ferromagnetism in these materials<sup>154</sup>. In comparison to the more complex magnetic phase diagram of the layered cobalt oxide system,  $\text{Li}_x\text{CoO}_2$ , the de-intercalation of  $\text{K}^+$  from  $\text{KCo}_2\text{Se}_2$  mostly affects the  $T_C$  instead of the types of magnetic ordering (i.e. various antiferromagnetic phases).<sup>155</sup> We attribute this difference in the physical properties to the multiple structural transitions as a function of  $x$  in  $\text{Li}_x\text{CoO}_2$  whereas we do not observe such transitions in the  $\text{KCo}_2\text{Se}_2$  system.

$\text{CoSe}$  shows clear ferromagnetic hysteresis at 1.8 K (Fig. 4.8), and in order to confirm the validity of this ferromagnetic signal, isothermal magnetization for  $\text{CoSe}$  was performed at various temperatures: 2 K, 60 K, and 150 K (Fig. 4.9). With the increase of temperature to 60 K, the hysteretic behavior for  $\text{CoSe}$  disappears and paramagnetic behavior emerges. In addition, the paramagnetic behavior at 60 K indicates the absence of any residual  $\text{KCo}_2\text{Se}_2$  in the sample since 60 K is well below its Curie temperature.

$\text{CoS}$  shows similar magnetic behavior to  $\text{CoSe}$  (Fig. 4.10). A ferromagnetic transition around 10 K was observed for  $\text{CoS}$ , and hysteretic behavior at 1.8 K that does not fully saturate at applied fields up to  $\pm 7$  T. A more thorough magnetic study may be required to elucidate the subtle differences between the selenides and sulfides. Such a study would be useful in light of the fact that the iron analogues,  $\text{FeSe}$  and  $\text{FeS}$ , display a different superconducting critical temperatures, 8 K and 5 K, respectively.

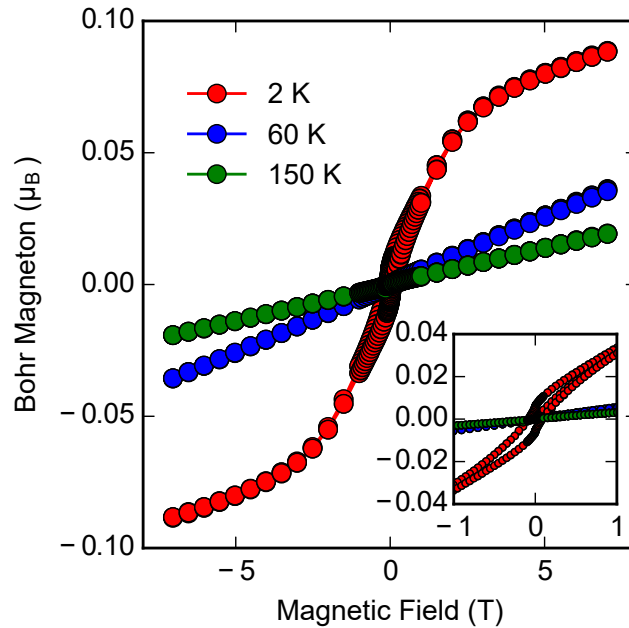


Figure 4.9: Isothermal magnetization vs. applied field  $H$  for CoSe at  $T = 2$  K, 60 K, and 150 K. While the 2 K data displays hysteresis with some blocking, the 60 K and 150 K data indicate paramagnetic behavior. The inset shows a zoomed region emphasizing the disappearance of hysteresis at higher temperatures.

Neutron diffraction remains one of the most powerful tools for elucidating the long-range magnetic ordering in materials, and our NPD data further elucidates the nature of such ordering in CoSe. First, the NPD does not indicate any long-range antiferromagnetic ordering in CoSe since the 3 K pattern (Fig. 4.4c) does not display any satellite reflections. We therefore rule out ferrimagnetic ordering as the cause of the hysteresis in the magnetization data. Second, we fit a ferromagnetic phase to the NPD data (Fig. 4.4d) and obtain a moment of  $0.30(17) \mu_B$  pointing only in the  $c$ -direction. After considering the magnetic contributions to the nuclear phase, the  $R_{wp}$  of the refinement decreased from 5.3 % to 4.7 %, indicating meaningful improvement of the statistics. The value for the moment may not be conclusive, however, due to the limitations of unpolarized neutron diffraction, where it is impossible to separate the nuclear from the magnetic contributions

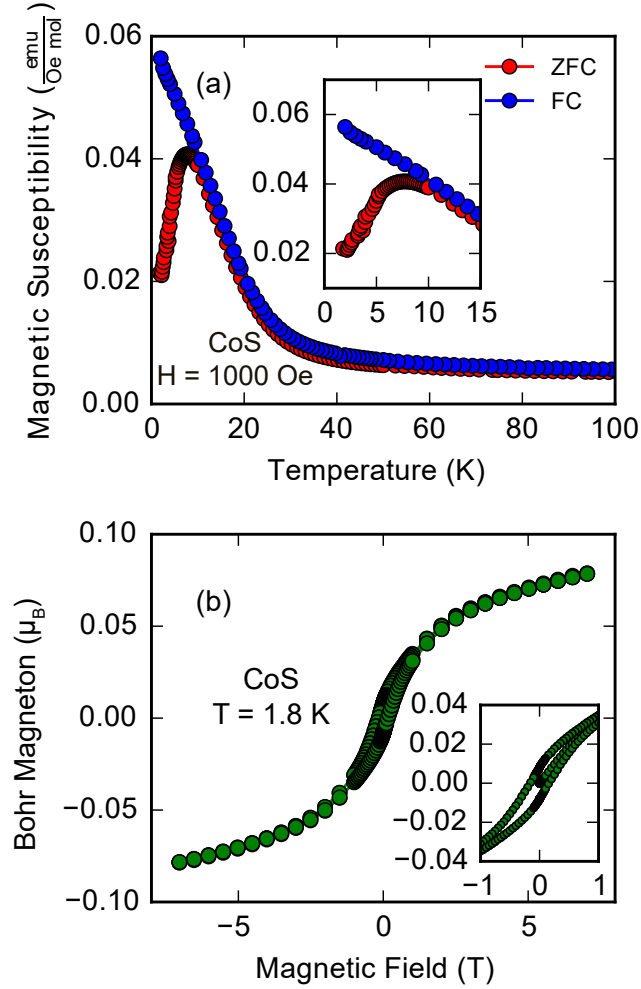


Figure 4.10: Magnetic susceptibility of CoS, measured in applied field of 1000 Oe. Temperature-dependent magnetic susceptibility  $\chi(T) = M/H$ :  $\text{KCo}_2\text{Se}_2$  (a) shows a ferromagnetic transition at  $T_C = 10$  K comparable to CoSe and (b) CoS shows incomplete saturation approaching  $0.09 \mu_B/\text{Co}$  at an applied field of 7 T, slightly less than CoSe.

to the Bragg reflections. It is important to note that our attempt to refine the magnetic moment for the 15 K NPD data led to a divergence in the fit. Since the moment is apparently small from the magnetization data, more careful temperature-dependent neutron diffraction studies may be carried out on a single crystal to study the nature of the weak itinerant ferromagnetism in CoSe.

### 4.3.4 Electrical Resistivity

Temperature dependent electrical resistivity of CoSe single crystal is presented in Fig. 4.11. The resistivity displays typical metallic behavior down to approximately 10 K, the proposed Curie temperature for CoSe. Due to the lack of single crystal  $\text{KCo}_2\text{S}_2$ , a single crystal of CoS was not prepared and no transport data is presented for CoS.

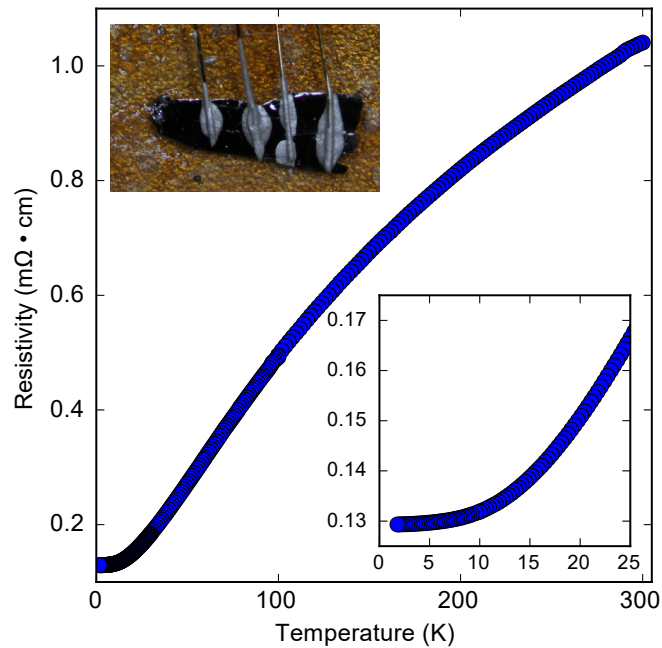


Figure 4.11: Temperature dependent electrical resistivity of CoSe measured on a single crystal. CoSe displays metallic behavior at high temperature with a slight deviation in slope around 10 K (inset), close to the ferromagnetic transition temperature.

The properties of CoSe can be summarized as a weak ferromagnetic metal. In the region below 10 K, (Fig. 4.11 inset), the slope of the resistivity curve changes abruptly from the high temperature region. This change is indicative of the ferromagnetic transition occurring at 10 K. It is known that ferromagnetic materials display clear  $T^2$  behavior at low temperature, below  $T_C$ , due to electron-electron scattering<sup>156</sup> and typical Fermi liquid behavior. This behavior is more profound in the ferromagnetic parent  $\text{KCo}_2\text{Se}_2$

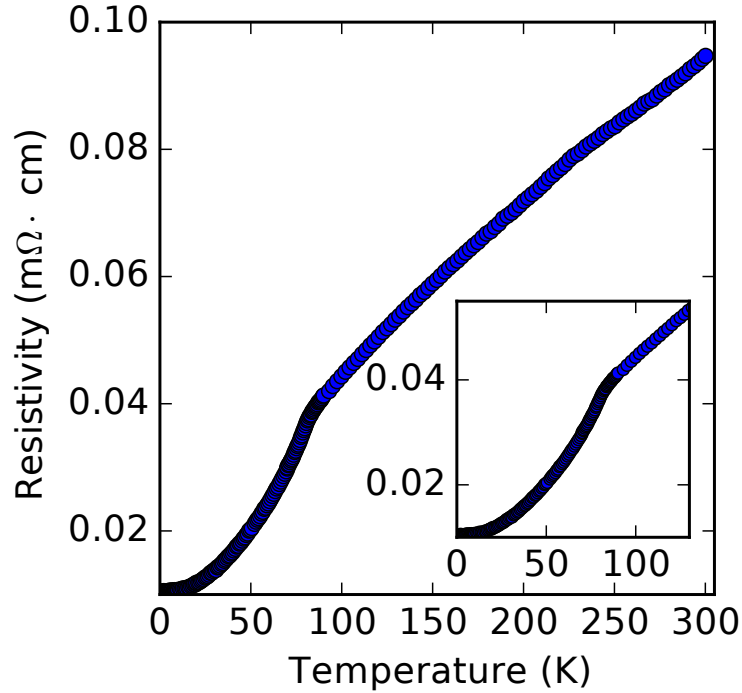


Figure 4.12: Temperature dependent electrical resistivity of  $\text{KCo}_2\text{Se}_2$  measured on a single crystal.  $\text{KCo}_2\text{Se}_2$  displays metallic behavior at high temperature with a slight deviation in slope around 80 K (inset), close to the ferromagnetic transition temperature.

compound (Fig. 4.12). Its temperature-dependent resistivity clearly shows linear correlation above 80 K close to its  $T_C$  (74 K), and  $T^2$  behavior below 80 K. With the addition of spin fluctuations contributions, electrical resistivity of a weak ferromagnet is predicted to have significant  $T^{5/3}$  behavior near the transition temperature<sup>157</sup>. The low temperature resistivity of CoSe does not display clear  $T^{5/3}$  or  $T^2$  behavior, and is likely a combination of the two. This can be attributed to the very low Curie temperature of CoSe; there is no distinct range for which different scattering processes will dominate, causing the overlap in temperature dependencies.

## 4.4 Discussion

### 4.4.1 De-intercalation chemistry of late transition metal chalcogenides

It is interesting to consider the crystallographic changes induced by our topochemical method for de-intercalation of  $AM_2Ch_2$ -type phases, and compare it with others recently published in the literature<sup>110</sup>. Depending on the synthetic conditions and the chemical system, kinetically controlled de-intercalation can also induce structural reconfiguration. In our topochemical de-intercalation, only a shift in the stacking of the alternating planes of  $CoCh$  along the  $c$ -direction occurs. As the de-intercalation proceeds, the body-centered operation is lost while an  $n$ -glide plane is introduced to change the  $CoCh$  stacking sequence (Fig. 4.1). Otherwise, no major reconstruction occurs within the  $CoCh$  planes, and the transition metal, whether iron or cobalt, remains in tetrahedral geometry.

So far we have demonstrated success on preparing anti-PbO type Fe and Co chalcogenides via our topochemical de-intercalation approach. Despite similar strategies, their respective synthetic conditions are not mutually interchangeable. As reported in our earlier work on single crystal tetragonal FeS obtained by de-intercalation of  $KFe_2S_2$ ,<sup>141</sup> highly basic hydrothermal conditions are oxidative and can lead to large concentrations of Fe vacancies. Hydrothermally prepared FeSe can also lead to a large number of vacancies, which are detrimental to superconductivity.<sup>126</sup> To remedy this, extra Fe powder was added in the autoclave to create a reducing environment and fill the Fe vacancies. The differences between the preparations of  $FeCh$  and  $CoCh$  suggest that fine-tuning of synthetic conditions will be required to obtain other anti-PbO type transition metal chalcogenides.

In all, it must be said that the target of other anti-PbO type *MCh* systems may be significantly harder to achieve in comparison to the cobalt analogues. A recent comprehensive study on the de-intercalation reaction conditions of  $\text{KNi}_2\text{Se}_2$  reported by Neilson and McQueen<sup>110</sup> sheds more light on this. Utilizing stronger oxidization conditions produced by  $\text{CuI}_2$  in acetonitrile, they reported formation of NiAs-type hexagonal NiSe from the  $\text{ThCr}_2\text{Si}_2$ -type  $\text{KNi}_2\text{Se}_2$ . Accompanying the de-intercalation of  $\text{K}^+$ , edge-sharing layered  $\text{NiSe}_4$  tetrahedra in  $\text{KNi}_2\text{Se}_2$  completely transform to corner-sharing  $\text{NiSe}_6$  octahedra. Although, this de-intercalation reaction is kinetically controlled, upon losing too much  $\text{K}^+$ ,  $\text{KNi}_2\text{Se}_2$  does not retain the original tetrahedral layered structure and transforms directly to the thermodynamically stable hexagonal NiSe. One of the major discoveries for this de-intercalation process is that the increase of Ni vacancies and Ni oxidation are the driving forces for structural reconstruction.<sup>110</sup>

#### 4.4.2 Intercalation chemistry of late transition metal chalcogenides

Ever since Gamble *et al.* prepared a large new family of intercalated layered transition metal dichalcogenides in the early 1970's to explore superconductivity,<sup>34,35</sup> intercalation chemistry has remained a great tool for the manipulation of layered materials held by van der Waals interactions. Intercalation chemistry via *chimie douce* methods in iron-based superconductors has more recently been pioneered by Clarke *et al.*<sup>20,23</sup> to overcome the common impurity phases that form from solid-state reactions of alkali metals with iron chalcogenides.<sup>22</sup> Before now, one of the outstanding issues was that the thermodynamically available tetragonal chalcogenides were limited to iron. With the discovery

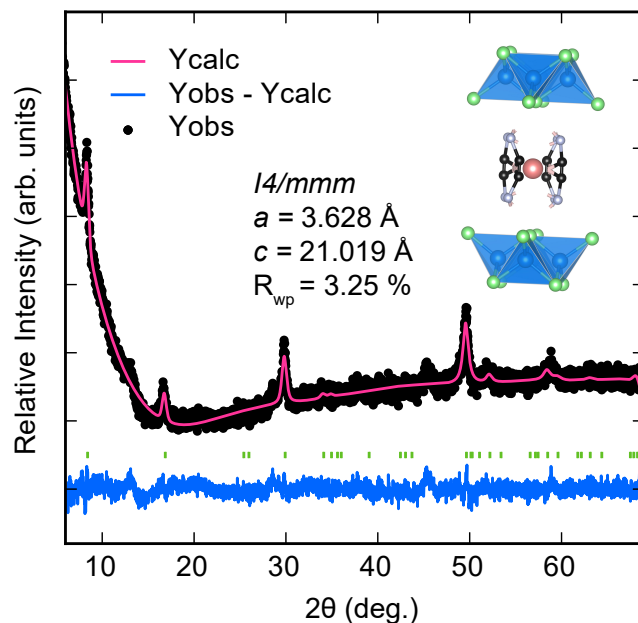


Figure 4.13: Powder X-ray diffraction patterns of ground polycrystalline  $\text{Li}(\text{C}_2\text{H}_8\text{N}_2)\text{CoSe}$  collected at room temperature. Refinement of the  $\text{Li}(\text{C}_2\text{H}_8\text{N}_2)\text{CoSe}$  structure in the body-centered tetragonal group ( $I4/mmm$ ). Tick marks represent the corresponding phase.

of the anti-PbO type  $\text{CoCh}$  in the present study, we now have the opportunity to explore intercalation chemistry in this new family.

First, we present the ion exchange reaction of  $\text{KCo}_2\text{Se}_2$  single crystals with  $\text{LiOH}$  using a similar hydrothermal route for  $\text{LiOH}$  intercalated  $\text{FeSe}$  from our previous work.<sup>53</sup> Hydrothermal reactions using  $\text{LiOH}$ , selenourea, and  $\text{H}_2\text{O}$  along with single crystals of  $\text{KCo}_2\text{Se}_2$  reacted at 100-160 °C for 1-3 days. Reactions at 100-120 °C yielded a mixture of the tetragonal  $\text{CoSe}$  and the pentlandite type  $\text{Co}_9\text{Se}_8$ , while reactions at 140 °C and above gave pure seleno-pentlandite in single crystal form (Fig. 4.14, Table 4.3). Although attempts to synthesize  $(\text{LiOH})\text{CoSe}$  were not successful, our method provides a route to high purity single crystal seleno-pentlandite, which was not available previously.

After the lack of success with  $\text{LiOH}$  intercalation, we present the direct intercala-

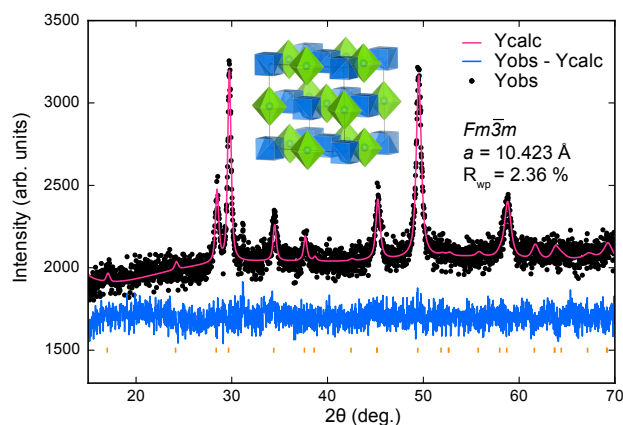


Figure 4.14: Rietveld refinements with x-ray powder diffraction on ground polycrystalline material of  $\text{Co}_9\text{Se}_8$  collected at room temperature. Refinement of  $\text{Co}_9\text{Se}_8$  in the pentlandite structure ( $Fm\bar{3}m$ ). Tick marks represent the corresponding phase for pentlandite.

Table 4.3: Structural parameters for ground polycrystalline material of  $\text{Co}_9\text{Se}_8$ . Rietveld refinements for preformed for the room temperature structures. All relevant bond angles and distances from the refinements are given.

$\text{Co}_9\text{Se}_8$ (298 K, PXRD), $Fm\bar{3}m$ , $R_{wp} = 2.356\%$				
$a = 10.4236(72)$ Å				
atom	Site	x	y	z
Co1	4b	0.5	0.5	0.5
Co1	32f	0.125	0.125	0.125
Se1	8c	0.25	0.25	0.25
Se2	24e	0.2713(6)	0	0
Co2-Se1 (Å)	Co2-Se2 (Å)	Se-Co-Se (°)	Se-Co-Se(°)	Co-Co (Å)
2.2567(8)	2.392(4)	105.1(1)	113.4(1)	2.6059(1)

tion with amine adducts of Li metal. The smaller layer spacing in the CoSe compared to the iron analogue (5.33 Å in CoSe vs. 5.52 Å in FeSe) could be an impediment to intercalation, so we used ethylenediamine (*en*) instead of liquid ammonia as the solvent to perform the reaction at an elevated temperature. Tetragonal CoSe was reacted with Li metal dissolved in 15 mL *en* on a Schlenk line under Ar flow at 70-90 °C for 7 days. The PXRD pattern of the as-recovered product (Fig. 4.13) closely matches the pattern of Li-*en* intercalated FeSe (Li-*en*-FeSe) reported by Hatakedra *et al.*<sup>45</sup> The new phase was

fit to a body-centered tetragonal cell ( $I4/mmm$ ) using the Pawley method, and its lattice constant  $c$  increased to 21.019 Å, which is comparable to Li-*en*-FeSe (20.74 Å<sup>45</sup>).

Although it is not possible to solve the structure of the Li-*en*-CoSe phase using our current PXRD data, a recent neutron diffraction study on Na-*en*-FeSe shed light on the structure of such amine-intercalated phases.<sup>48</sup> Using the model by Jin *et al.*, the proposed structure for Li-*en*-CoSe is shown in Fig. 4.13. To confirm the intercalation of Li cations into CoSe, the sample was heated to 800 °C in air to decompose it. The PXRD pattern of the decomposition product was fit well with the layered LiCoO<sub>2</sub> structure ( $R\bar{3}m$ ), suggesting the presence of Li in the intercalated compound. The exciting implication of this result is that the intercalation chemistry for the Fe family can also be applied to the Co system.

First-principles calculations of the electronic density of states, and bonding analysis of such states may also provide answers as to the optimal electron filling level and the possible limits of topochemical de-intercalation and intercalation. We discuss those in the next section.

### 4.4.3 Relationship to FeSe and DFT Predicted Stability

Anti-PbO type FeSe and FeS with critical temperatures ( $T_c$ 's) of 8 K<sup>13</sup> and 4 K<sup>63</sup> respectively, are of great interest to the superconductivity community. The synthesis of the isostructural CoSe and CoS offers another point for investigation how the variation of electronic structure leads to superconductivity. Some basic physical and chemical properties of CoSe and CoS can be understood when analyzing the density of states (DOS) and

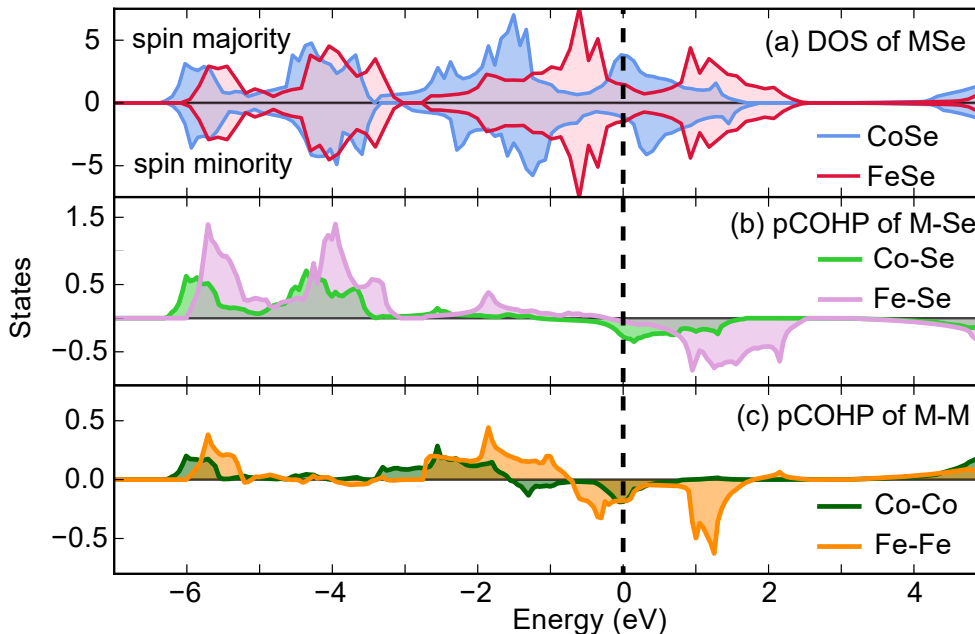


Figure 4.15: a) The spin-polarized electronic density of states (DOS) of FeSe and CoSe. b) The partial crystal orbital Hamilton population (pCOHP) to describe the  $M$ -Se bonding and antibonding interactions. c) The pCOHP for  $M-M$  interactions. In b) and c), positive and negative states represent bonding and anti-bonding interactions, respectively.

their projected crystal orbital Hamilton population (pCOHP) of the cobalt system in comparison to the iron analogues. In particular, phase stability can be compared intuitively by analyzing their bonding and anti-bonding interactions using COHP extracted by the LOBSTER package provided by Dronskowski and co-workers<sup>81-84</sup>. The results of DFT calculations on CoSe and FeSe are shown in Fig. 4.15.

In comparing the spin-polarized density of states (DOS) for CoSe with FeSe, the former shows clear splitting of the DOS near the Fermi level. This splitting matches Stoner's criterion for ferromagnetism, whereby the spin-polarized DOS are lowered in energy due to exchange interactions<sup>158</sup>. Similar exchange splitting is also observed for CoS (Fig. 4.17). The predicted ground state magnetic moments on each Co atom in CoSe and CoS are  $0.32 \mu_B$  and  $0.42 \mu_B$ , respectively. Our DFT calculations therefore suggest

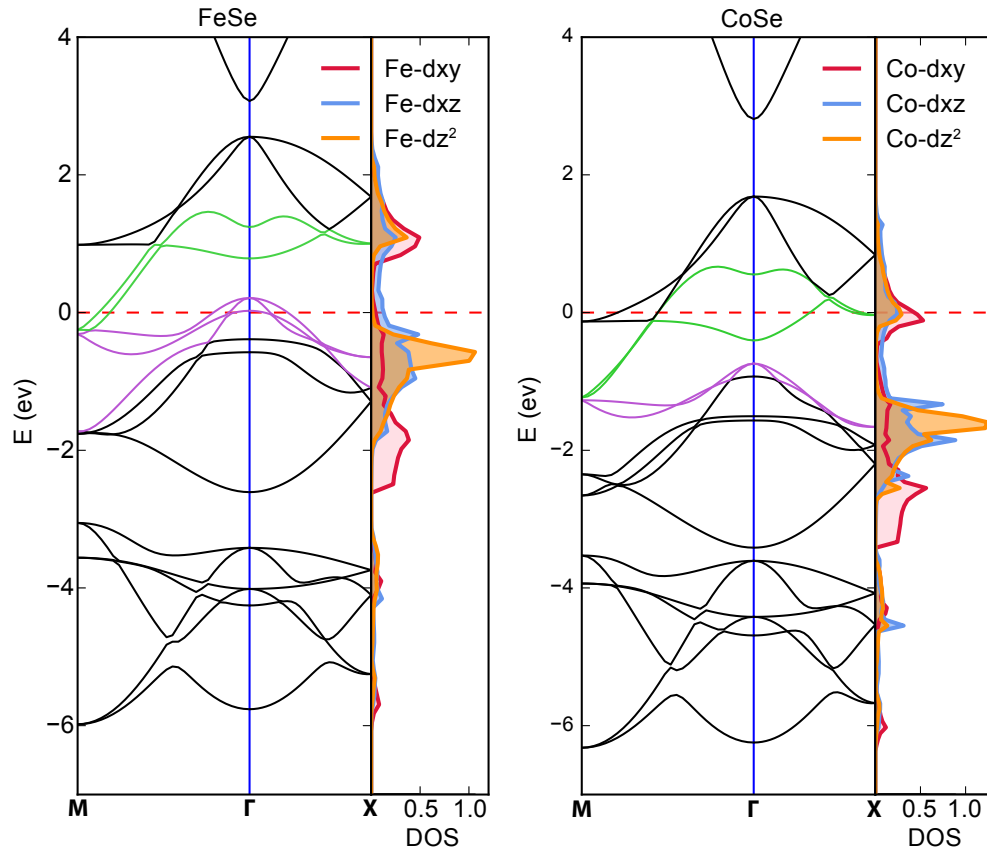


Figure 4.16: Band structure along three different directions and the corresponding partial DOS of 3d states for FeSe and CoSe. Purple and green lines in the band structure indicate bands crossing the Fermi-level close to the  $\Gamma$  and M points, respectively.

weak itinerant ferromagnetism in both tetragonal CoSe and CoS and well describe the physical property and neutron diffraction measurements. A previous DFT study by Ding *et al.*<sup>159</sup> did not predict CoSe to be ferromagnetic as spin-polarized calculations were not carried out.

To explore how the electronic structure affects phase stability, and hence the success of topochemical de-intercalation, COHP analysis was performed for tetragonal Fe, Co and Ni chalcogenides (Fig. 4.15, Fig. 4.17 and Fig. 4.18). Amongst this group, the anti-PbO type FeSe is the only thermodynamically stable one. The so-called  $\beta$ -FeSe is

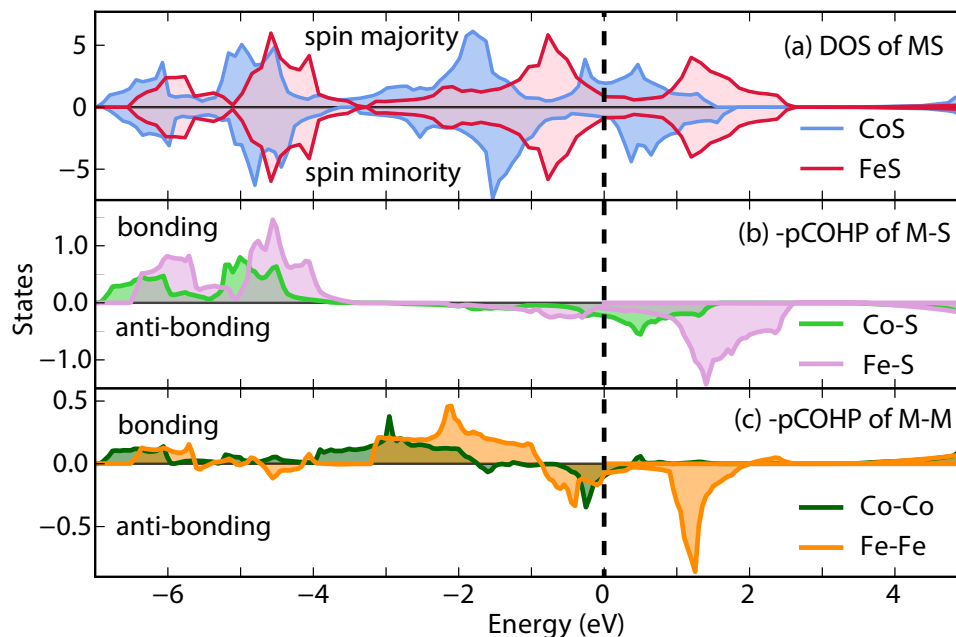


Figure 4.17: Density functional theory (DFT) calculations of FeS and CoS for a) the total density of states (DOS) and -pCOHP of b) M-S and c) M-M interactions. In b) and c), positive and negative states represent bonding and anti-bonding interactions, respectively.

on the Fe-Se phase diagram and can be formed by direct reaction of the elements at high temperatures. In contrast, FeS, CoSe and CoS can only be synthesized using kinetically controlled and therefore low-temperature routes, and tetragonal NiSe and NiS remain hypothesized compounds.

COHP plots show that for  $M - Ch$  interactions, there are nearly negligible anti-bonding states at the Fermi-level for FeSe, whereas FeS, CoSe, and CoS (Fig. 4.15 and Fig. 4.17) show population of anti-bonding states increasing in the order listed. The increased anti-bonding character suggests that FeS, CoSe to CoS become less stable, which matches the observations from our synthetic work. For NiSe and NiS, both COHP plots (Fig. 4.18) show stronger anti-bonding characters for Ni- $Ch$  interactions, which may also explain why they have yet to be reported. In addition, NiSe shows significantly increased

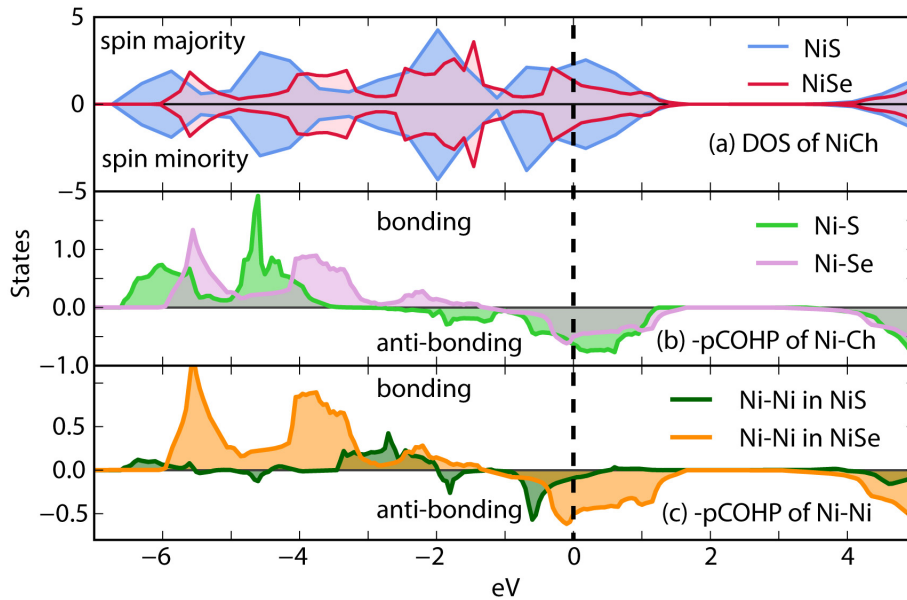


Figure 4.18: Density functional theory (DFT) calculations of NiSe and NiS for a) the total density of states (DOS) and -pCOHP of b) Ni-*Ch* and c) Ni-Ni interactions. In b) and c), positive and negative states represent bonding and anti-bonding interactions, respectively.

Ni-Ni anti-bonding interactions. By retaining the metal square sublattice, the stronger Ni-Ni anti-bonding interactions will increase as the de-intercalation of  $K^+$  proceeds. Such unfavorable interactions would then be countered by the formation of a large amount of Ni vacancies or structural reconstruction altogether.

One of the most interesting features of the iron-based superconductors has been the control of superconducting properties through the manipulation of the Fermi surface and therefore the filling of the electronic bands. Given the very similar tetragonal structures, the electronic dispersion curves along high-symmetry points of the *CoCh* phases are similar to those of the *FeCh* phases. As shown in the partial DOS diagram of Fig. 4.16, the ten dispersion curves from  $-2$  eV to  $+2$  eV correspond to the predominately 10 *d*-orbitals of

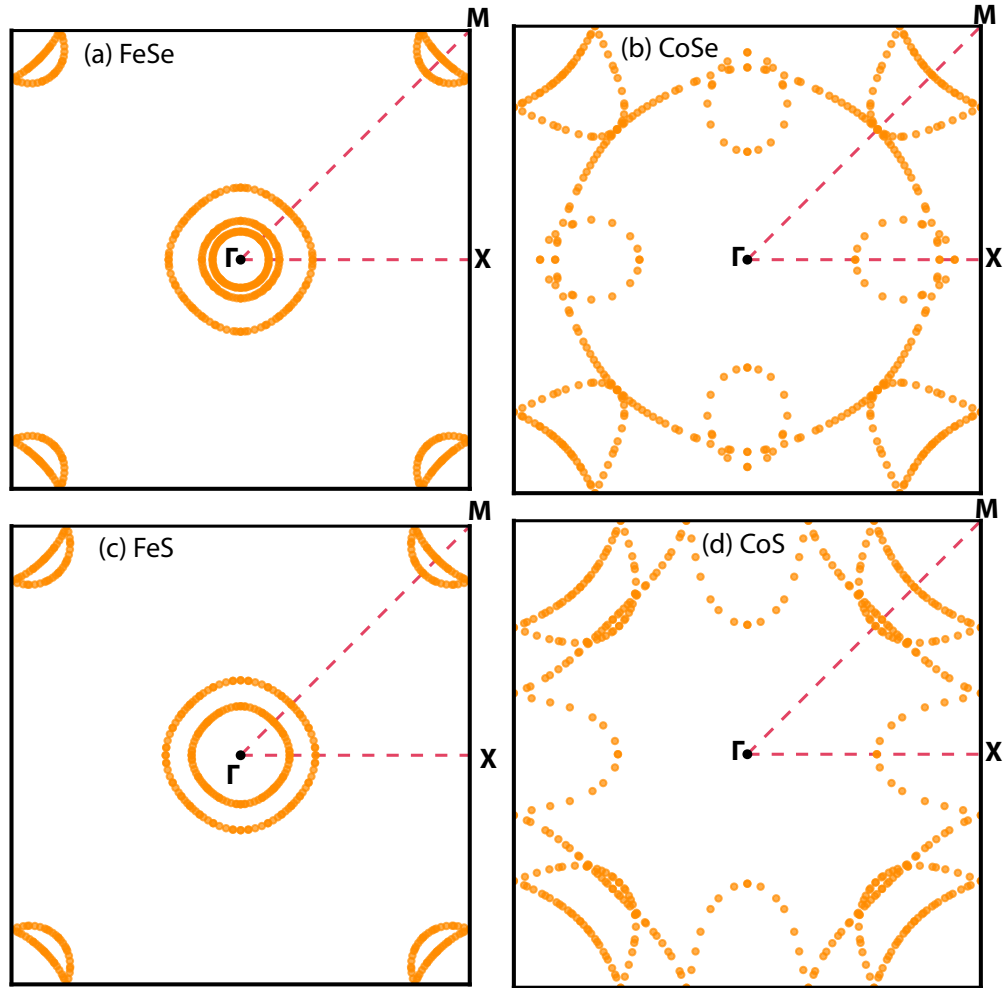


Figure 4.19: Fermi surface plots on the  $\Gamma$ -M-X plane for a) FeSe, b) CoSe, c) FeS and d) CoS.

the two transition metals per unit cell. Therefore, in the simple anti-PbO type structure for transition metal chalcogenides, the physical properties are derived from the occupation of the predominantly  $d$ -bands.

Since Co has one more electron than Fe, the Fermi level of CoSe moves to higher energy levels with respect to the Fe analogues (Fig. 4.16 and Fig. 4.20). Consequently, the hole pockets at the  $\Gamma$ -point close to the Fermi level in  $FeCh$  superconductors are missing in the  $CoCh$  phases. The electron pockets at the M-point become much deeper for

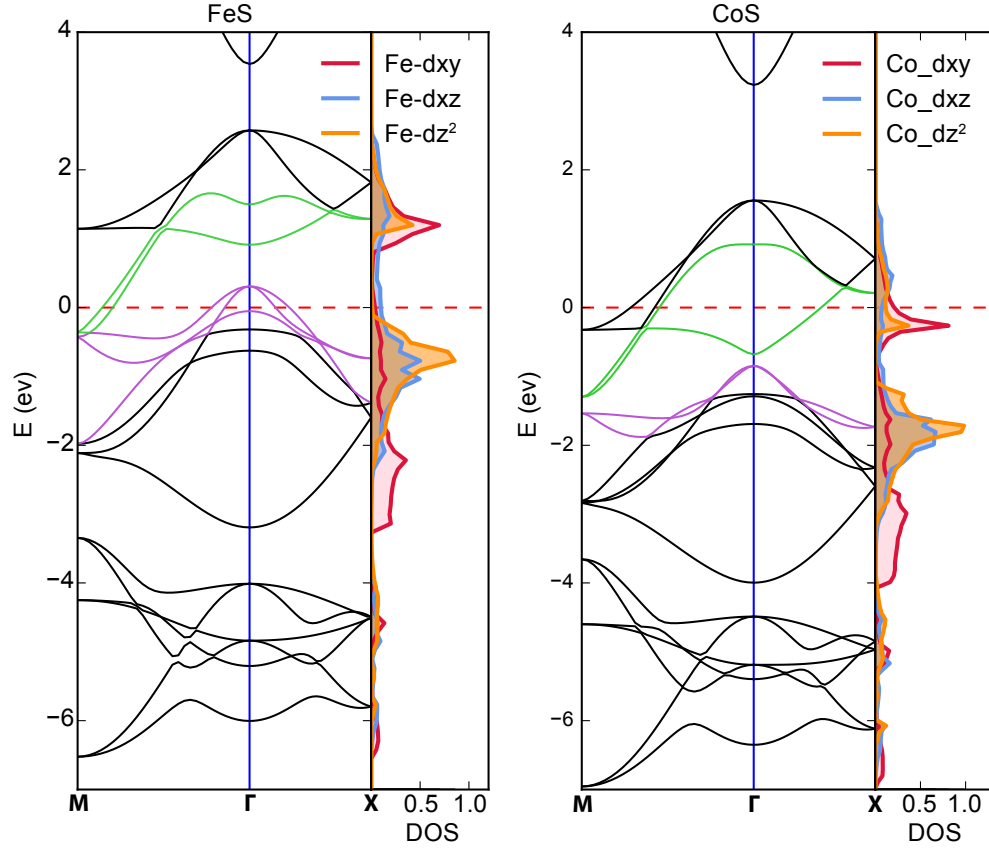


Figure 4.20: Band structure and partial DOS of 3d orbitals of a) FeS and b) CoS. Purple and green lines in the band structure indicate bands crossing the Fermi-level close to the  $\Gamma$  and M points, respectively.

*CoCh*. Since nesting of the electron and hole pockets is considered to be key for the superconducting mechanism, we did not anticipate the pure *CoCh* phases to be superconducting on this simple diagram. Recent ARPES studies on the FeSe/STO mono-layer superconductors ( $T_c \sim 100$  K)<sup>27,29</sup> have revealed the absence of hole pocket at the  $\Gamma$ -point, and it is suggested that the electron pocket at M-point could be more important. Hence, it might be possible to tune *CoCh* towards superconductivity by reducing the electron density near the M-point via Fe substitution on the Co site or As/P substitution on the chalcogenide site.

The Fermi surfaces of *FeCh* are highly two-dimensional and manifest themselves as isolated 2D cylindrical sheets that do not overlap. As shown in their band structures (Fig. 4.16a and Fig. 4.20a), there are three bands crossing the Fermi level of FeSe close to the  $\Gamma$ -point, while there are only two for FeS. This is reflected on their Fermi surface plots, as three and two cylindrical sheets can be seen for FeSe and FeS, respectively. For *CoCh*, because there is no hole pocket at the  $\Gamma$ -point, their Fermi surfaces have moved farther away from the  $\Gamma$ -point compared to *FeCh*. More importantly, a complete reconstruction of the Fermi surface occurs and in *CoCh* a flatly dispersing band approaching the X-point is occupied.

## 4.5 Conclusions

We have demonstrated that through topochemical means, new binary phases can be prepared and particularly that kinetic control is a means to prepare novel 2D layered transition metal chalcogenides. These new phases can be stabilized if the topochemical de-intercalation utilizes mild oxidative environment and replenishing metal vacancies in the chalcogenide layer. With this strategy we prepared the hypothesized metastable CoSe and CoS with the anti-PbO structure for the first time. These new *CoCh* phases will now help answer some important questions regarding superconductivity in their iron analogues FeSe and FeS. Furthermore, the topochemical de-intercalation of single crystalline  $\text{KCo}_2\text{Se}_2$  lead the formation of single crystalline CoSe, which was key for more thorough exploration of physical properties such as electrical resistivity. Finally, our physical property and neutron diffraction measurements of CoSe reveals that it is a weak itinerant

ferromagnet with a  $T_C$  near 10 K and a small moment near  $0.1 \mu_B$  per Co cation. Similar measurements for CoS reveal weak ferromagnetism as well, although the less crystalline nature of CoS impedes a more accurate determination of its physical properties.

DFT calculations support our interpretation of both CoSe and CoS as weak ferromagnetic metals, and the manner in which the Fermi level fills the predominately  $d$ -states helps explain why CoSe and CoS should not be expected to be superconductors. Furthermore, bonding analysis of the electronic DOS reveals that antibonding Co- $Ch$  states are more occupied than in the case of the iron analogues, thus justifying the higher thermodynamic stability in the latter compounds.

Future work in this area includes further expansion of known layered  $MCh$  phases through intercalation chemistry. Our first attempts with bases such as Li-ethylenediamine indicate that CoSe can indeed act as intercalation host. Given that guest species can readily be inserted into these materials, we now have a tool to increase the two-dimensionality of the electronic structures. Since the simple electronic structure of the metal square sublattice does not seem to change much as a function of transition metal, we anticipate that the physical properties of new  $MCh$  phases could be predicted.

## Chapter 5: The Preparation and Phase Diagrams of ( ${}^7\text{Li}_{1-x}\text{Fe}_x\text{OD}$ )FeSe and ( $\text{Li}_{1-x}\text{Fe}_x\text{OH}$ )FeSe Superconductors

The work described within this chapter was published in *Journal of Materials Chemistry C* **2016**, 4, pg. 3934. Christopher Borg, Jeffrey W. Lynn, Shanta Saha, Johnpierre Paglione, Craig M Brown, and Efrain Rodriguez were contributing authors of the manuscript. X.Z. and C.K.H.B prepared the samples and collected XRD data, X.Z., C.K.H.B, and J.W.L. collected the neutron data, X.Z., C.K.H.B, and S.S. collected MPMS data.

### 5.1 Introduction

In the iron-based pnictide and chalcogenide superconductors, chemical doping and physical pressure are universal variables by which to tune the superconducting properties.<sup>11,85</sup> For example, the critical temperature,  $T_c$ , of 8 K in FeSe under ambient conditions<sup>13,16</sup> can be raised to 38 K by externally applied pressure<sup>19,129</sup> or 44 K by intercalation of cationic species.<sup>20,23,40,160</sup> The tetragonal ( $P4/nmm$ ) structure of FeSe (1.1) consists of sheets of edge-sharing  $\text{FeSe}_4$  tetrahedra held together by van der Waals interactions, which makes it an ideal host for intercalation chemistry. Negative pressure, or strain, has also been implicated as a parameter in the high  $T_c$  of 65 K - 100 K reported for single

layered FeSe.<sup>27,28,161</sup> Given the propensity of the FeSe layered system for chemical and physical manipulation, FeSe is an ideal platform for understanding the superconductivity of the iron-based systems and for the preparation of new layered functional materials. The recently discovered  $(\text{Li}_{1-x}\text{Fe}_x\text{OH})\text{FeSe}$  system,<sup>25,26,52,162,163</sup> which contains PbO-type layers of LiOH alternating with the anti-PbO type layers of FeSe (Figure 1), offers such an opportunity. Iron may occupy the lithium site and therefore effectively charge dope the FeSe layer since the  $(\text{Li}_{1-x}\text{Fe}_x\text{OH})$  layer would be positively charged. Sun *et al.* have also reported that increased lithiation of the  $(\text{Li}_{1-x}\text{Fe}_x\text{OH})$  layer would force iron to occupy any vacancies in the FeSe layer, which can be detrimental to the superconducting properties.<sup>26</sup>

Three outstanding issues in the  $(\text{Li}_{1-x}\text{Fe}_x\text{OH})\text{FeSe}$  system and related phases are whether 1) the parent phase is antiferromagnetic, 2) superconductivity coexists with ferromagnetism, and 3) any isotope effects on  $T_c$  exist. Critical to answering all three questions is the preparation of the deuterioxide version of  $(\text{Li}_{1-x}\text{Fe}_x\text{OH})\text{FeSe}$  and comparing their phase diagrams. Furthermore, hydrothermal synthesis under either  $\text{H}_2\text{O}$  or  $\text{D}_2\text{O}$  presents interesting differences in the purity of the resulting superconducting phases due to differences in the reaction kinetics. Thus, this study will help workers in the field understand the thermodynamic and kinetic factors in the preparation of phase pure and superconducting FeSe-based materials.

Due to the large incoherent scattering of hydrogen and high neutron absorption cross section of  $^6\text{Li}$ , our compounds were prepared doubly isotopically pure,  $(^7\text{Li}_{1-x}\text{Fe}_x\text{OD})\text{FeSe}$ , which allowed for an opportunity to complete a phase diagram for the deuterated series. Although some studies have found no evidence of ferromagnetism below  $T_c$  in their sam-

ples,<sup>162,163</sup> under the right synthesis conditions, we have observed a ferromagnetic signal in the superconducting regime as first reported by Pachmayr *et al.*<sup>25</sup> Herein, we report the phase diagram for  $(\text{Li}_{1-x}\text{Fe}_x\text{OD})\text{FeSe}$ , compare it to that of  $(\text{Li}_{1-x}\text{Fe}_x\text{OH})\text{FeSe}$ , and investigate the magnetic properties of the non-superconducting and superconducting samples.

## 5.2 Experimental

### 5.2.1 Sample preparation

The preparation of powder samples were modified from a hydrothermal route reported in the literature.<sup>54,163</sup> For the synthesis of deuterated samples we first prepared the doubly isotopically pure  $^7\text{LiOD}$  as a precursor.  $^7\text{LiOD}$  was prepared by mixing a stoichiometric amount of  $^7\text{LiCO}_3$  (Sigma Aldrich, 99% for  $^7\text{Li}$ ) and  $\text{CaO}$  (calcined from  $\text{CaCO}_3$ , Sigma Aldrich, 99%) in  $\text{D}_2\text{O}$ . The  $\text{CaCO}_3$  precipitate was filtered, and  $^7\text{LiOD}$  crystallized by evaporation of the solvent.

For a typical preparation of  $(\text{Li}_{1-x}\text{Fe}_x\text{OD})\text{FeSe}$ , 5 mmol of Fe powder (Alfa Aesar, 99.9%), 6 mmol of selenourea (Sigma Aldrich, 98%) and 50 mmol of  $\text{LiOD}$  powder were suspended in 5 mL of distilled  $\text{D}_2\text{O}$  (Oxford Isotope, 99.9%). The mixture was placed in a Teflon-lined stainless steel autoclave at 120-200 °C for 3-5 days. Afterwards, the autoclave was opened in an argon-filled glove bag, and the shiny black precipitate was washed with  $\text{D}_2\text{O}$ . The product was washed and centrifuged several times until the supernatant was clear. The remaining product was collected, vacuumed dried, and stored in a nitrogen-filled glove box. The yield of the product was usually between 50% and 70%.

Single crystal  $(\text{Li}_{1-x}\text{Fe}_x\text{OD})\text{FeSe}$  and  $(\text{Li}_{1-x}\text{Fe}_x\text{OH})\text{FeSe}$  samples were prepared by replacing potassium cations with LiOD or LiOH from  $\text{K}_x\text{Fe}_{2-y}\text{Se}_2$  single crystals under hydrothermal conditions similar to those reported by Dong *et al.*<sup>111</sup> For the growth of the  $\text{K}_x\text{Fe}_{2-y}\text{Se}_2$  single crystals, 1.8 g (13 mmol) of FeSe powder was mixed with 0.21 g (5.4 mmol) of potassium metal (Alfa Aesar, 99%) to match the nominal composition of  $\text{K}_{0.8}\text{Fe}_{2-y}\text{Se}_2$ .<sup>128,164</sup> The FeSe precursor was prepared by heating Fe (Alfa Aesar, 99.9%) and Se (Alfa Aesar, 99%) powders to 700 °C for 5 h followed by furnace cooling; the resulting phase does not need to be of the tetragonal  $\beta$ -FeSe form for the crystal growth. The FeSe/K mixtures were loaded in a quartz ampoule inside a nitrogen-filled glovebox, and the ampoules flame sealed under vacuum. In order to avoid oxidation of the samples from breaking of the ampoule due to potassium-induced corrosion of the quartz walls, the sample container was sealed in a larger ampoule. For crystal growth of  $\text{K}_x\text{Fe}_{2-y}\text{Se}_2$ , the mixture was heated to 1030 °C over 10 h and held at 1030 °C for 3 hours to form a homogeneous melt. Subsequently, the melt was slowly cooled at a rate of 6 °C/hour to 650 °C to allow crystal growth. After cooling to room temperature,  $\text{K}_x\text{Fe}_{2-y}\text{Se}_2$  single crystal approximately 8 mm in diameter was recovered.

In order to compare the effect of  $\text{D}_2\text{O}$  to the reaction kinetics, single crystals of both  $(\text{Li}_{1-x}\text{Fe}_x\text{OH})\text{FeSe}$  and  $(\text{Li}_{1-x}\text{Fe}_x\text{OD})\text{FeSe}$  were prepared under identical hydrothermal conditions. For the preparation of  $(\text{Li}_{1-x}\text{Fe}_x\text{OH})\text{FeSe}$  single crystals, the  $\text{K}_x\text{Fe}_{2-y}\text{Se}_2$  precursor (0.2 g - 0.4 g), 0.14 g (2.5 mmol) Fe powder, and 2 g (47 mmol) LiOH monohydrate were added to 5 mL water. For  $(\text{Li}_{1-x}\text{Fe}_x\text{OD})\text{FeSe}$  single crystals, to match the concentration of LiOH in water, 1.2 g (47 mmol) LiOD and 6 mL  $\text{D}_2\text{O}$  were used for reactions. The mixture was placed in a Teflon-lined stainless steel autoclave at 120-200

°C for 4-5 days. Silver colored single crystals were recovered by washing away excess powder with water and drying under vacuum overnight. The as-recovered single crystals retained similar shape to the starting  $K_x\text{Fe}_{2-y}\text{Se}_2$  single crystals.

Samples prepared in the absence of excess iron powder were not superconducting, which could be due to either oxidation of the iron or vacancy formation in the FeSe layer. To study the role of metal powders during the cation exchange reactions, experiments using Sn metal (Alfa Aesar, 99.9%) instead of Fe powder for the preparation of  $((\text{Li}_{1-x}\text{Fe}_x\text{OH})\text{FeSe})$  and  $((\text{Li}_{1-x}\text{Fe}_x\text{OD})\text{FeSe})$  single crystals at 120 °C were carried out. Sn can react with hot concentrated bases to form soluble  $[\text{Sn}(\text{OH})_6]^{2+}$  species while evolving  $\text{H}_2$  gas,<sup>165</sup> thus providing a stronger reducing environment than the hydrothermal reactions without the presence of metal powders.

### 5.2.2 Laboratory and synchrotron X-ray diffraction measurements

Room temperature powder X-ray diffraction (PXRD) data were collected on a Bruker D8 X-ray diffractometer ( $\lambda = 1.5418 \text{ \AA}$ ). Data were collected with a step size of  $0.02^\circ$  between  $7^\circ$  and  $70^\circ$  for Pawley fits to extract lattice constants and  $7^\circ$  and  $120^\circ$  for Rietveld fits to obtain better structural parameters. In order to find any possible crystallographic phase transitions that are coupled to either the superconducting or magnetization order parameters, temperature dependent (5-300 K) high-resolution synchrotron X-ray diffraction was carried out for powders of ground single crystals at Beamline

11-BM at the Advanced Photon Source (APS). In addition to finding subtle changes in symmetry due to peak splitting, the synchrotron measurements provide high- $Q$  data

and therefore more accurate structural parameters. Analysis of the high- $Q$  reflections help determine any small changes in the iron occupancies in both the FeSe and LiOH layers, which could affect  $T_c$ 's of the sample as suggested by Sun *et al.*<sup>18</sup> An Oxford helium cryostat (closed flow system) was used to reach a temperature that is close to liquid helium ( $\approx 4$  K). Ground powders of single crystals were packed in 0.4 mm Kapton capillaries tubes and sealed with epoxy. Diffraction data were collected between  $0.5^\circ$  and  $46^\circ$  with a step size of  $0.0001^\circ$  using a constant wavelength  $\lambda = 0.413964 \text{ \AA}$  (30 keV).

### 5.2.3 Magnetization measurements

Magnetic susceptibility measurements were carried out using a magnetic property measurement system (Quantum Design MPMS). Both field-cooled (FC) and zero-field-cooled (ZFC) magnetic susceptibility measurements were taken from 2 K - 300 K in direct current mode with an applied magnetic field of 1 or 3 mT.

### 5.2.4 Neutron powder diffraction measurements

All the neutron work was carried out with doubly isotopically pure samples ( $^7\text{Li}_{1-x}\text{Fe}_x\text{OD}$ )FeSe at the NIST Center for Neutron Research (NCNR). The samples were loaded into He-filled vanadium cans and subsequently into a closed cycle refrigerator for low temperature measurements. Low temperature (4 K) diffraction data were collected on the BT-1 high-resolution NPD with the Cu(311) monochromator ( $\lambda = 1.540 \text{ \AA}$ ). In addition to base temperature measurements, we performed NPD measurements at various temperatures 25 K, 75 K, 150 K, and room temperature to search for any crystallographic phase transi-

tions. High-intensity and coarse-resolution diffraction measurements were carried out on the BT-7 spectrometer ( $\lambda = 2.359 \text{ \AA}$ ) using the position sensitive detector (PSD) to search for magnetic Bragg peaks from base temperature up to 150 K.<sup>67</sup>

## 5.3 Results

### 5.3.1 Crystallography and phase diagram

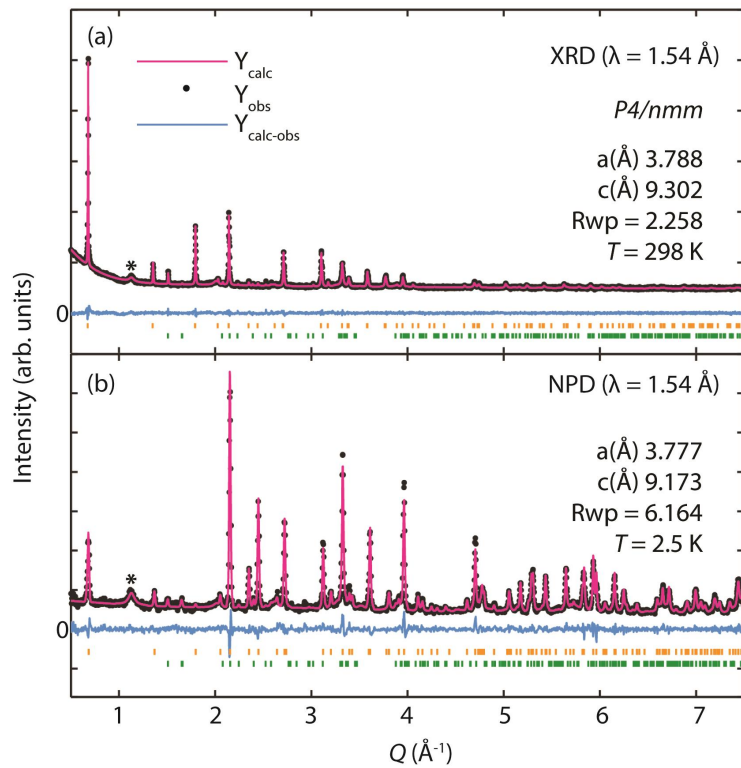


Figure 5.1: (a) X-ray and (b) neutron powder diffraction for non-superconducting ( ${}^7\text{Li}_{1-x}\text{Fe}_x\text{OD}$ )FeSe with  $x = 0.166$ . No magnetic phase could be indexed in the NPD, indicating lack of antiferromagnetic ordering. Weight percent fractions from structural refinements are as follows: 98% ( ${}^7\text{Li}_{1-x}\text{Fe}_x\text{OD}$ )FeSe (gold ticks) and 2%  $\text{Li}_2\text{CO}_3$  (green ticks). A few broad peaks corresponding to FeSe were fit by a Pawley routine (asterisk).

Rietveld refinements with both XRD and NPD data were carried out with the TOPAS 4.2 software.<sup>66</sup> Representative fits to one of the deuterioxide samples are presented in 5.1

for both laboratory X-rays and neutrons. Although the samples are mostly phase pure, some starting reagent  $\text{Li}_2\text{CO}_3$  was found as an impurity in the neutron data, which is more of a bulk technique than X-ray diffraction. Furthermore, two very broad peaks could be indexed as close to the lattice parameters of the parent phase  $\beta\text{-FeSe}$ . Indeed, these peaks have also been observed in previous work.<sup>25,52</sup> The much broader peak width for the FeSe impurity is indicative of very small crystallite size and quantitatively fitting this phase is not possible given its nearly amorphous nature.

Table 5.1: Rietveld refinement of synchrotron PXRD data collected at 7 K for a superconducting sample of ( ${}^7\text{Li}_{1-x}\text{Fe}_x\text{OD}$ )FeSe shown in Fig. 5.2 and a non-superconducting sample. Both samples are fitted to a  $P4/nmm$  space group with origin choice 1. The tetrahedral angles  $\alpha_1$  and  $\alpha_2$  represent the Se-Fe-Se angles in and out of the basal plane, respectively.

$a = 3.7725(1) \text{ \AA}, c = 9.1330(2) \text{ \AA}, R_{wp} = 12.83\%, T_c = 37 \text{ K}$						
Atom	Wyckoff site	$x$	$y$	$z$	Occ.	$U_{iso} (\text{\AA}^2)$
Li/Fe1	2b	0	0	0.5	0.827/0.173(2)	0.0134
Fe2	2a	0.5	0.5	0	0.979(2)	0.0057
O	2c	0.5	0	0.4266(3)	1	0.0037(7)
Se	2c	0	0.5	0.1603(1)	1	0.0028(2)
$\alpha_1$ ( $^\circ$ )	$\alpha_2$ ( $^\circ$ )	Fe-Fe ( $\text{\AA}$ )	Fe-Se ( $\text{\AA}$ )			
104.38(2)	112.07(1)	2.6675(1)	2.3875(4)			
$a = 3.7820(1) \text{ \AA}, c = 9.0992(1) \text{ \AA}, R_{wp} = 10.66\%, \text{ non-superconducting}$						
Atom	Wyckoff site	$x$	$y$	$z$	Occ.	$U_{iso} (\text{\AA}^2)$
Li/Fe1	2b	0	0	0.5	0.809/0.191(2)	0.0156
Fe2	2a	0.5	0.5	0	0.919(2)	0.0036
O	2c	0.5	0	0.4252(3)	1	0.0038(1)
Se	2c	0	0.5	0.1609(1)	1	0.0019(6)
$\alpha_1$ ( $^\circ$ )	$\alpha_2$ ( $^\circ$ )	Fe-Fe ( $\text{\AA}$ )	Fe-Se ( $\text{\AA}$ )			
104.51(2)	112.01(1)	2.6743(1)	2.3914(3)			

The temperature-dependent synchrotron diffraction data did not reveal any major crystallographic changes in the structure (5.2). Therefore, unlike the parent FeSe phase, which undergoes a tetragonal to orthorhombic phase transition near 75 K,<sup>15</sup> ( $\text{Li}_{1-x}\text{Fe}_x\text{OH}$ )FeSe and ( $\text{Li}_{1-x}\text{Fe}_x\text{OD}$ )FeSe remain tetragonal down to base temperature (10 K). Rietveld re-

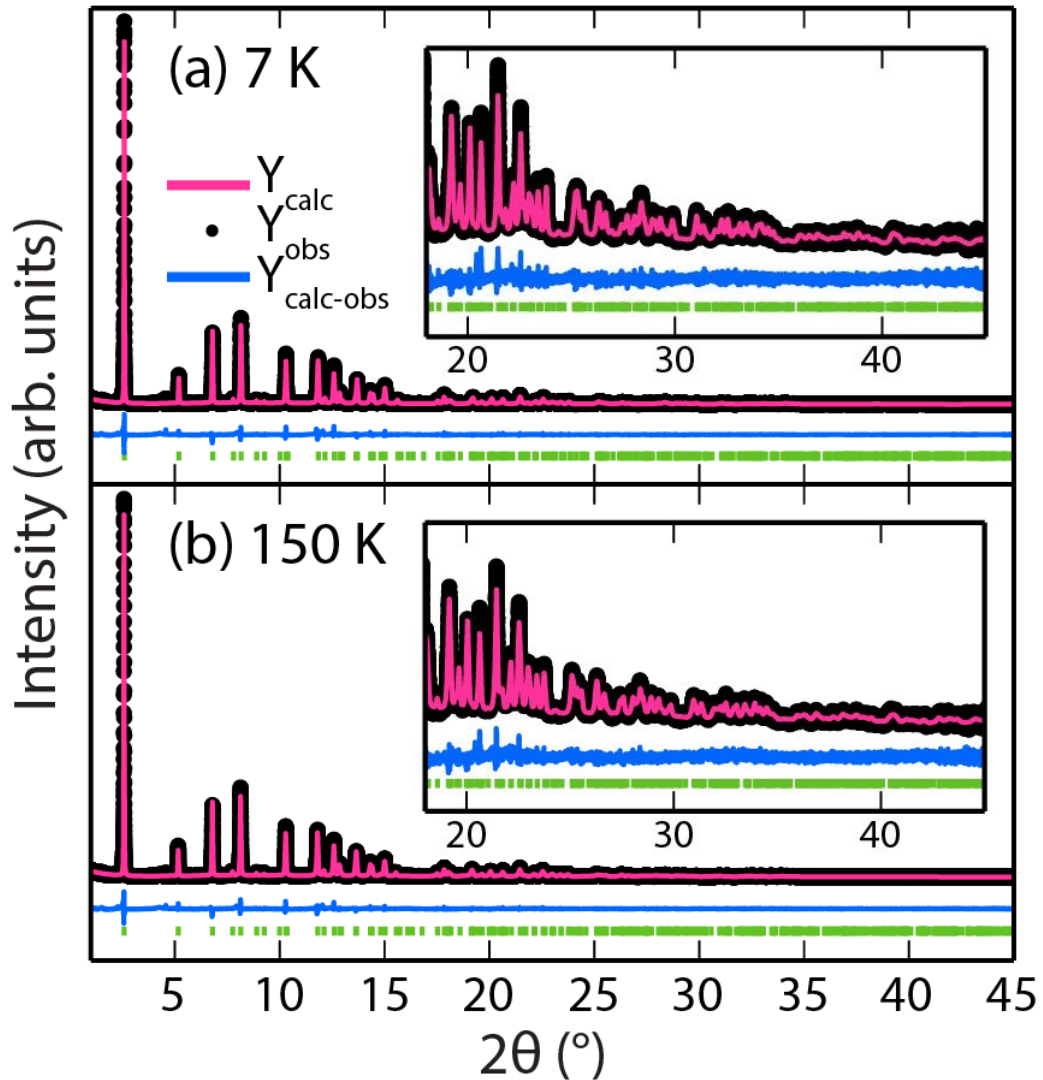


Figure 5.2: Synchrotron powder X-ray diffraction pattern at (a) 7 K and (b) 150 K for a single crystal sample of  $(\text{Li}_{1-x}\text{Fe}_x\text{OD})\text{FeSe}$  prepared at 120 °C for 5 days ( $T_c = 37$  K). Rietveld refinement of data collected at both temperatures did not reveal any lowering of symmetry from tetragonal  $P4/nmm$ . Tick marks representing the tetragonal phase are shown below the calculated, observed, and differences curves. The insets shown are a zoom in of the high-angle synchrotron data.

refinements of one of the deuterioxide patterns at 7 K and 150 K are presented in 5.2, and relevant structural parameters are in 5.1 for both superconducting and non-superconducting deuterioxide phases. Relevant bond distances and bond angles are also shown in 5.1. Only

results from the synchrotron X-ray dataset are presented in 5.1, and structural parameters from the Rietveld refinements, including the neutron data, for the rest of the samples used to construct the full phase diagrams can be found in the ESI (Tables S1-S5).

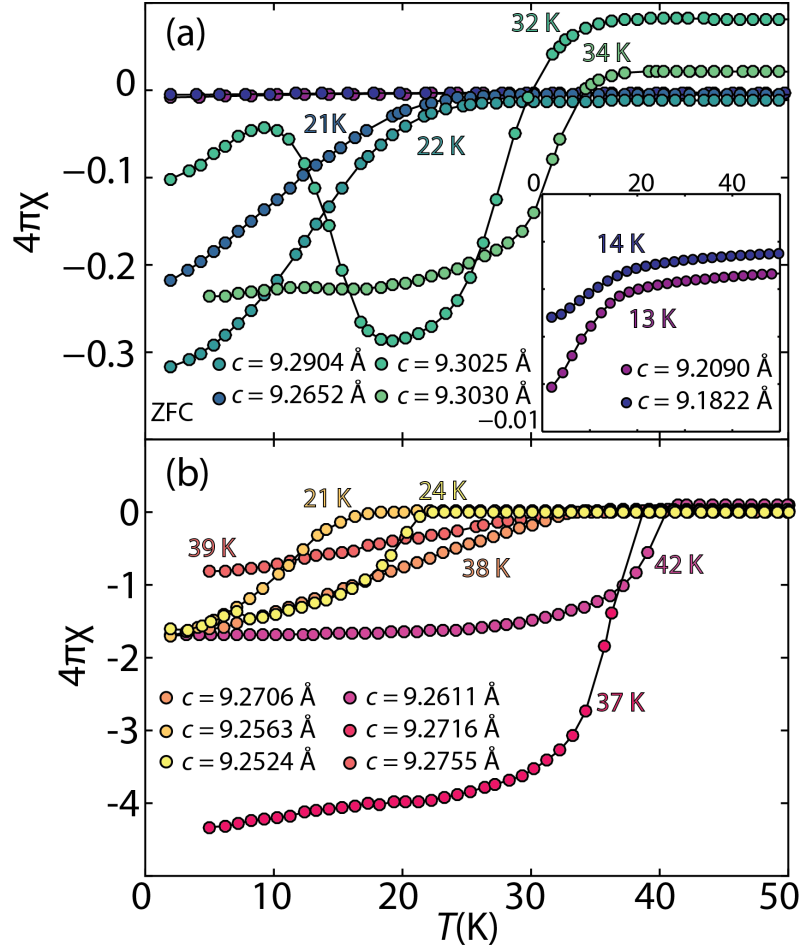


Figure 5.3: Magnetic susceptibility of samples prepared by (a) powder routes and (b) single crystal routes of deuterioxide series  $(\text{Li}_{1-x}\text{Fe}_x\text{OD})\text{FeSe}$ . For  $T_c = 32$  K, a ferromagnetic transition can be noted at  $T_f = 10$  K. ZFC data of powder samples and single crystal samples collected with applied fields of 1 mT and 3 mT, respectively, are shown.

### 5.3.2 Magnetization results and the phase diagrams

The SQUID magnetic susceptibility measurements for the series of hydroxide samples prepared through the powder routes are presented in 5.3a. The deuterioxide samples,

which were all derived from the single crystal route, are shown in 5.3b. Only one sample within the hydroxide series expressed a ferromagnetic signal within the superconducting regime. A similar plot (Figure S1) for the hydroxide system prepared via the single crystal route can be found in the ESI.

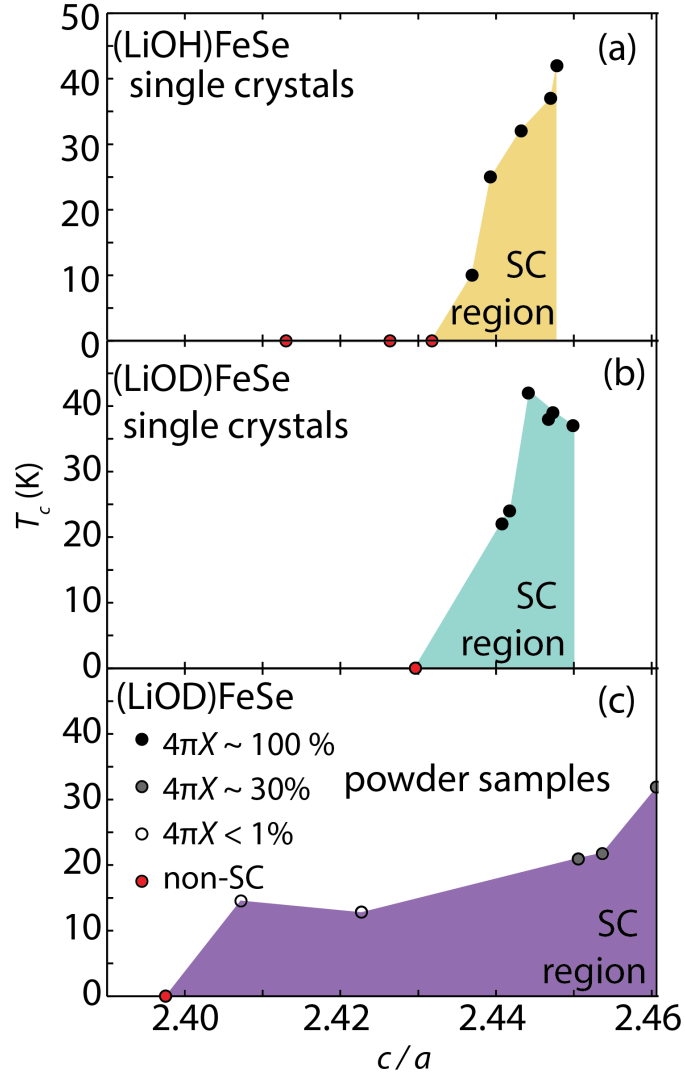


Figure 5.4: Superconducting phase diagrams of (a)  $(\text{Li}_{1-x}\text{Fe}_x\text{OH})\text{FeSe}$  as comparison for that of (b) single crystal  $({}^7\text{Li}_{1-x}\text{Fe}_x\text{OD})\text{FeSe}$  and (c) powder samples and  $(\text{Li}_{1-x}\text{Fe}_x\text{OD})\text{FeSe}$ . The critical temperatures  $T_c$  are related to the tetragonality parameter, which is the simple ratio of the lattice parameters  $c/a$ .

We have constructed superconducting phase diagrams in 5.4 that relate the critical

temperatures  $T_c$  to the lattice constants compiled from the SQUID data and diffraction results from all the samples. The lattice parameters of the tetragonal unit cell found at room temperature were used as the x-axis versus  $T_c$  in the phase diagrams. More specifically, we found the best correlation to  $T_c$  is that of the tetragonality parameter, which is the simple  $c/a$  ratio. The corresponding superconducting volume fractions ( $4\pi\chi$ ) were also established by SQUID magnetometry (5.3). We found that  $T_c$  and its volume fraction increased with the lattice constant  $c$  and decreased with lattice constant  $a$ . Therefore, those with the highest tetragonality gave the maximum  $T_c$  and superconducting volume fractions. For samples to exhibit significant superconducting volume fractions ( $4\pi\chi > 10\%$ ), the lattice constant  $c$  must be larger than about 9.20 Å and  $a$  smaller than about 3.80 Å. These trends in the lattice parameters are consistent with the findings of Sun *et al.* on their hydroxide analogues,<sup>26</sup> where they attribute a large lattice constant to iron vacancies in the FeSe layers and therefore iron slightly oxidized above 2+.

Our combined diffraction experiments did indeed find variations on the iron occupancies, whether superconducting or non-superconducting. In general, the smaller the tetragonality parameter, the lower the  $T_c$ . As 5.1 shows, when the occupancy of the Fe2 site falls from near full to 91.9(2) %, superconductivity is lost. The differences overall between the hydroxide samples prepared by powder routes and the single crystal ones could be due the accommodation of iron vacancies during the syntheses. As Sun *et al.* found in their samples,<sup>26</sup> when FeSe in its tetragonal  $\beta$ -phase is used as the host for intercalation via hydrothermal synthesis, iron powder is necessary in order to fill in the resulting vacancies. When we start with Fe powder and selenourea as the Se source, this leads to more variability in the amount of iron vacancies and therefore a larger spread in the tetrago-

nality parameter that can express superconductivity (5.4). Our powder method therefore would lead to the in-situ growth of alternating FeSe and  $\text{Li}_{1-x}\text{Fe}_x\text{OD}$  layers rather than post-synthetic modification (also known as soft chemistry) of FeSe layers as done in our single crystal method.

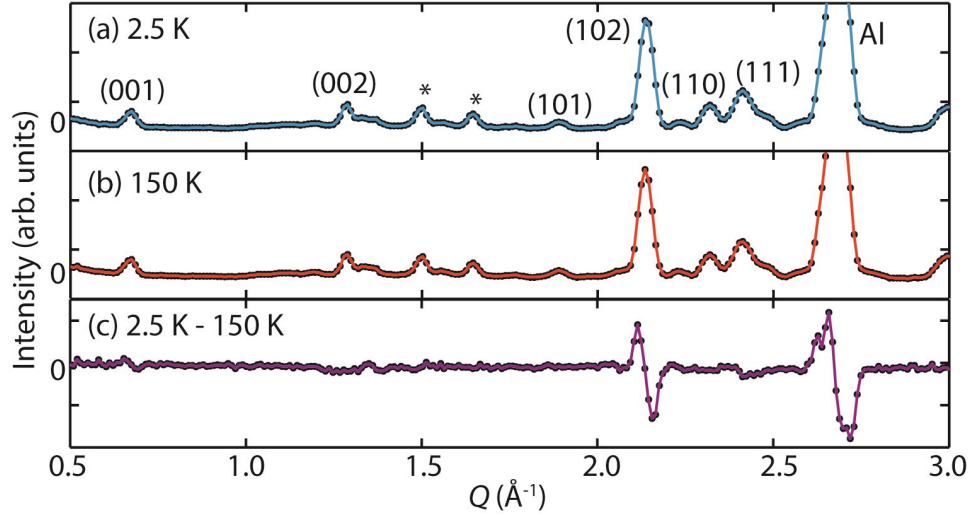


Figure 5.5: (a) The NPD pattern of non-superconducting phase of  $({}^7\text{Li}_{1-x}\text{Fe}_x\text{OD})\text{FeSe}$  at 150 K and (b) 4 K. The difference between the two patterns in (c) reveals no antiferromagnetic peaks.

### 5.3.3 Neutron results

To verify whether any of the samples exhibit antiferromagnetism, we searched for any superlattice peaks in the NPD patterns that could arise below 120 K, the AFM transition in the parent phase of  $(\text{Li}_{1-x}\text{Fe}_x\text{OD})\text{FeSe}$  reported by Dong *et al.*<sup>163</sup> No superlattice reflections were observed in the BT-1 high-resolution NPD patterns, and our deuterated samples allowed for a low background in case of a small Fe signal. Indeed, in the arsenide systems the iron moment can be small in the parent phases such as  $0.36(5) \mu_B/\text{Fe}$  in  $\text{LaOFeAs}$ <sup>166</sup> and  $0.25(7) \mu_B/\text{Fe}$  in  $\text{NdOFeAs}$ ,<sup>167</sup> Any hydrogen incoherent background

would easily overwhelm such a small signal from long-range magnetic ordering in the NPD. The samples were measured up to 50 K on BT-1, and no long range magnetic ordering was observed. NPD patterns measured with a PSD on BT-7, which has a much higher flux than BT-1 at low angles, also revealed no antiferromagnetic peaks in the non-superconducting samples (5.5). Difference patterns between 150 K and 4 K are shown in Figure 6, revealing no residual intensity and only differences arising from thermal expansion and thus peak positions.

## 5.4 Discussion

### 5.4.1 Relation between structural parameters and superconductivity

In preparing our deuterioxide samples, we found the reaction temperature to influence the lattice constants. Mild hydrothermal reaction temperatures (120 °C) led to samples expressing a higher  $T_c$ , while the reaction temperature above 180 °C led exclusively to either non-superconducting samples or ones with very low volume fractions ( $4\pi\chi < 1\%$ ). Reaction times also affected the lattice constants. Longer reaction times (>3 days) yielded samples with slightly larger  $a$  and smaller  $c$  (i.e. smaller tetragonality parameters). While all the deuterated samples followed the trend shown in the phase diagram (5.4), similarly prepared hydrated samples deviated in their behaviour. Indeed, some hydroxide samples with lattice parameters matching those in the phase diagram from earlier literature<sup>1</sup> did not exhibit superconductivity (5.3a). Interestingly, samples prepared at lower temperatures with the described mixing ratio and longer reaction times expressed coexistence between superconductivity and ferromagnetism (Figure 3). Thus, while longer reaction

times above 180 °C led to lower  $T_c$ 's or non-superconducting samples, longer reaction times at lower temperatures (120 °C) produced the ferromagnetic signal in superconducting  $(\text{Li}_{1-x}\text{Fe}_x\text{OD})\text{FeSe}$ . As described in the next section, this might be a kinetic effect from the increasing amount of oxidized iron in water from longer reaction times.

## 5.4.2 Relation between magnetism and superconductivity

In several of our non-superconducting samples, we have observed an antiferromagnetic transition close to 120 K. Dong et al.<sup>163</sup> have claimed that the hydroxide samples in the non-superconducting dome were antiferromagnetic parent phases with a  $T_N$  close to 120 K, and therefore that the selenides and arsenides have the same underlying physics with respect to the superconducting mechanism. This is a very important claim that could have large implications in the field of iron-based superconductors. None of our non-superconducting deuterioxide samples, however, exhibited this antiferromagnetic signal in the SQUID measurements, which led us to believe that the antiferromagnetism may not be intrinsic to this system.

Our findings in the preparation of hydroxide and deuterioxide samples revealed the strong possibility that the 120 K transition observed in the SQUID magnetization measurements arise from iron oxide impurities. The so-called Verwey transition, which corresponds to a  $\text{Fe}^{2+}/\text{Fe}^{3+}$  charge ordering transition in  $\text{Fe}_3\text{O}_4$  also occurs near 120 K.<sup>168,169</sup> Furthermore, structurally related  $\text{Li}_x\text{FeO}_2$  phases can express  $T_N$  from 100 K to 300 K according to amount of intercalated lithium cations.<sup>170,171</sup>

In order to study the formation of iron oxide impurities, a sample was prepared

under similar hydrothermal conditions but without the addition of selenourea. As pointed out by Sun *et al.* in their extensive study of the formation of  $(\text{Li}_{1-x}\text{Fe}_x\text{OH})\text{FeSe}$ , the strongly basic conditions ( $\text{pH} > 14$ ) of the synthesis strongly favors the formation of  $\text{Fe}^{3+}$  species according to the electrochemical-pH phase equilibrium diagram (i.e. Pourbaix) of iron.<sup>51</sup> Therefore, without the selenourea reagent to stabilize divalent iron, a large amount of mixed valent iron oxides are produced from hydrothermal synthesis containing large amounts of LiOH (or LiOD).

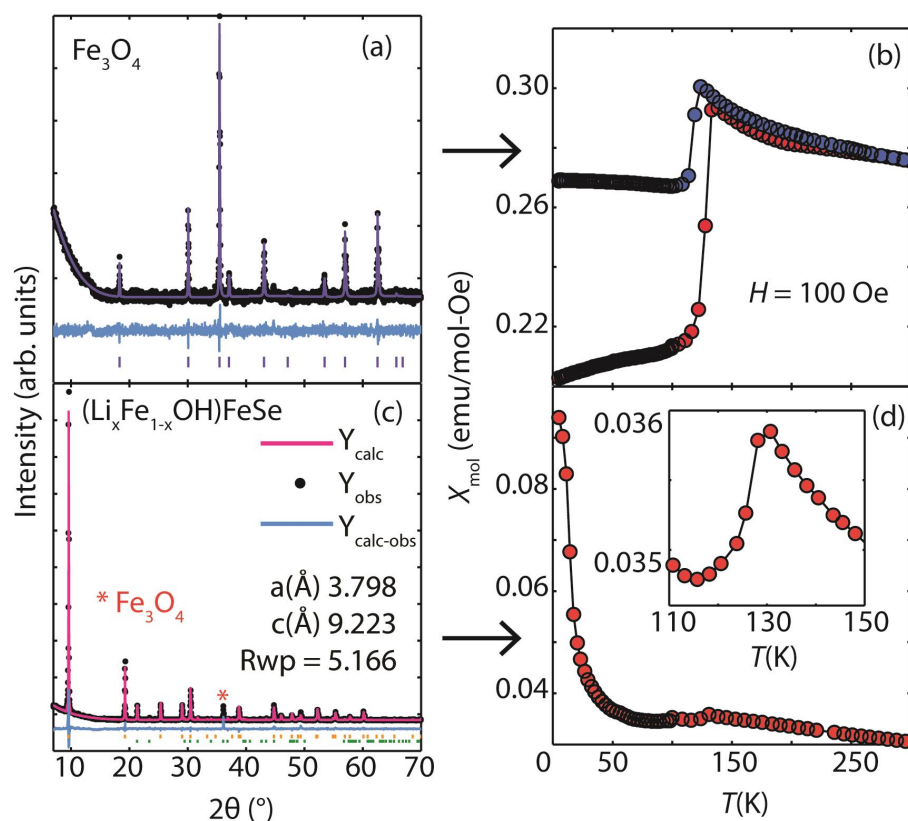


Figure 5.6: (a) Powder XRD and Rietveld analysis of phase pure  $\text{Fe}_3\text{O}_4$  prepared under similar hydrothermal conditions to that of  $(\text{Li}_{1-x}\text{Fe}_x\text{OH})\text{FeSe}$  in the absence of selenourea. (b) The corresponding magnetization data of the  $\text{Fe}_3\text{O}_4$  sample indicating the Verwey transition near 125 K. (c) The powder XRD of  $(\text{Li}_{1-x}\text{Fe}_x\text{OH})\text{FeSe}$  with the  $\text{Fe}_3\text{O}_4$  impurity marked along its strongest reflection. (d) The corresponding magnetization data of this non-superconducting  $(\text{Li}_{1-x}\text{Fe}_x\text{OH})\text{FeSe}$  sample, exhibiting the 125 K transition similar to that of  $\text{Fe}^{2+}/\text{Fe}^{3+}$  charge ordering seen in  $\text{Fe}_3\text{O}_4$  (inset).

The XRD pattern of the as-recovered sample from hydrothermal synthesis without selenourea was fitted to the  $\text{Fe}_3\text{O}_4$  structure, and its magnetic susceptibility measurement was in very good agreement with typical Verwey transition at 120 K (5.6). As shown in 5.6b, a hydroxide sample with lattice constants in the supposed superconducting region showed no superconductivity, but a transition similar to charge ordering in  $\text{Fe}_3\text{O}_4$ . Peaks in the XRD pattern (indicated by \* in Figure 5.6b) that cannot be matched with the  $(\text{Li}_{1-x}\text{Fe}_x\text{OH})\text{FeSe}$  phase was indexed well with the strongest peaks of  $\text{Fe}_3\text{O}_4$ . In addition, our synchrotron XRD data for a non-superconducting  $(\text{Li}_{1-x}\text{Fe}_x\text{OH})\text{FeSe}$  single crystal sample revealed small amounts of  $\text{Fe}_3\text{O}_4$  impurity (Figure S2), which was not observed by laboratory X-ray measurements. Therefore, it is likely that the 120 K transition in non-superconducting  $(\text{Li}_{1-x}\text{Fe}_x\text{OH})\text{FeSe}$  samples is extrinsic and due to magnetic impurities  $\text{Fe}_3\text{O}_4$  or structurally related  $\text{Li}_x\text{FeO}_2$ , which would modulate the ordering temperature.

Hydrothermal synthesis of samples with  $\text{D}_2\text{O}$  under similar conditions as those with  $\text{H}_2\text{O}$  did not lead to appreciable oxide impurity. We therefore conclude that the observed differences in the acid-base chemistry of  $\text{H}_2\text{O}$  and  $\text{D}_2\text{O}$  lead to different products for similar reaction conditions. Indeed, a hydrothermal treatment of iron powder with  $\text{D}_2\text{O}$  and with  $\text{LiOD}$  did not lead to complete conversion to  $\text{Fe}_3\text{O}_4$  but left unreacted iron powder (approximately 50%). Since under highly basic conditions,  $\text{Fe}^{3+}$  should be favoured thermodynamically, we believe the kinetics for the oxidation of iron with  $\text{D}_2\text{O}$  is slower than in  $\text{H}_2\text{O}$ . The autoionization constant of  $\text{D}_2\text{O}$  is smaller than that of  $\text{H}_2\text{O}$  due to the stronger  $\text{D-O}$  bond than the  $\text{H-O}$  bond.

All deuterioxide single crystal samples prepared in  $\text{D}_2\text{O}$  showed noticeable higher  $T_c$ 's than their hydroxide counterparts prepared at identical conditions (Table S2). The  $T_c$

of hydroxide samples can be improved by reducing the reaction time (i.e. 37 K vs. 32 K for 2 d and 4 d, respectively at 120 °C). It is likely that a shorter reaction time reduced the extent of Fe oxidation. Interestingly, both  $(\text{Li}_{1-x}\text{Fe}_x\text{OH})\text{FeSe}$  and  $(\text{Li}_{1-x}\text{Fe}_x\text{OD})\text{FeSe}$  single crystals prepared using Sn metal instead of Fe powder at 120 °C showed the same  $T_c$  at 42 K, higher than other samples without using Sn. The advantage of Sn metal was to create a reducing environment without introducing iron oxide impurities, due to lack of Fe powder.

Although we have established here that the  $(\text{Li}_{1-x}\text{Fe}_x\text{OH})\text{FeSe}$  system likely does not have a parent antiferromagnetic phase, we do not suggest that the chalcogenide-based superconductors are not linked to the arsenide-based superconductors from the present results. The  $\text{Fe}_{1+x}\text{Te}_y\text{Ch}_{1-y}$  for  $Ch = \text{Se}$  and  $\text{S}$  phases in particular exhibit a rich magnetic phase diagram<sup>62,131</sup> before superconductivity sets in with chemical substitution.<sup>172</sup> The ordered vacancy phase of  $\text{K}_{0.8}\text{Fe}_{1.6}\text{Se}_2$ <sup>128,164</sup> has also shown an antiferromagnetic transition at large temperatures (about 559 K)<sup>173</sup> while the disordered vacancy phase exhibits a  $T_c$  close to 30 K.<sup>21,107,174–176</sup> What distinguishes those two systems, however, from the present compound and  $\text{FeSe}$ , is the lack of a large magnetic moment on iron in the latter compounds.<sup>38,177–181</sup> In  $\text{Fe}_{1+x}\text{Te}$  it can be as large as  $2 \mu_B$ <sup>99</sup> and in  $\text{K}_{0.8}\text{Fe}_{1.6}\text{Se}_2$  as large as  $3.3(1) \mu_B$ .<sup>173</sup> Not surprisingly, when in the superconducting regime, both compounds exhibit a spin resonance energy in the inelastic neutron spectra, which corresponds to spin fluctuations. A large magnetic moment is clearly not the case in the present system.

As to the ferromagnetic transition observed at about 10 K in the sample with a  $T_c$  of 34 K, several authors have also observed it in the hydroxide analogues. Pachmeyer *et al.* attribute the long range magnetic order at 18 K to the iron cations partially substituted

on the Li site,<sup>25</sup> while Lu *et al.* assign this transition as being antiferromagnetic (about 12 K) according to their NMR studies.<sup>52</sup> Our recent small angle neutron scattering study illustrates the formation of long-range magnetic order below 12.5 K, but with a moment too small to see with diffraction.<sup>54</sup> No doubt this observation arises from the crystallographic site where the moment is located is too dilute with iron occupancy.

## 5.5 Conclusions

In conclusion, we have successfully mapped out a phase diagram for  $(\text{Li}_{1-x}\text{Fe}_x\text{OD})\text{FeSe}$  and have found that the highest  $T_c$  for deuterated samples is 42 K, and the  $T_c$  for both deuterated and hydroxide samples correlate with lattice constants. Since the highest  $T_c$  observed for the hydroxide sample was also approximately 42 K, we conclude that there is no isotope effect on the superconducting properties in substituting H by D. Mild hydrothermal preparation for long reaction times can lead to the coexistence of ferromagnetism and superconductivity. Finally, any claims of anti-ferromagnetism in the parent phase of this system should be re-evaluated in light of the easy preparation of oxide impurities with transition temperatures near the vicinity of 120 K in  $\text{H}_2\text{O}$ .

## Chapter 6: Superconductivity and Magnetism in Iron Sulfides Inter-calated by Metal Hydroxides

The work described within this chapter was published in *Chemical Science* **2017**, 8, pg. 3781. Christopher Eckberg, Brandon Wilfong, Sz-Chian Liou, Hector Vivanco, Johnpierre Paglione and Efrain Rodriguez were contributing authors of the manuscript. X.Z. prepared the samples, collected MPMS data and performed elemental analysis, B.W. and H.V. assisted with synthesis, C.E. and B.W. collected resistivity and heat capacity data, S.C.L. and X.Z. collected the TEM data.

### 6.1 Introduction

The chemistry of iron-based superconductors has been dominated by the arsenide,<sup>8,166,167,182,183</sup> selenide,<sup>13,14,17,18</sup> and telluride<sup>62,131,184</sup> compounds since their discovery nearly a decade ago. Many high-temperature superconductors exhibit layered structures, and rich chemistry can be applied to modify their structures that may result in the increase of their critical temperatures ( $T_c$ ).<sup>185,186</sup> We demonstrate that iron sulfides prepared by hydrothermal routes provide a new series of superconductors that could further elucidate the structure-property relationships across closely related phases. Mainly, we isolate FeS layers to enhance their two-dimensional (2D) electronic character by inserting metal hydroxide

spacers that also act as electron donating layers.

The tetragonal form of FeS known as mackinawite is a metastable mineral recently shown to be superconducting with a  $T_c$  near 4 K.<sup>63,141</sup> Mackinawite FeS adopts the anti-PbO structure where FeS<sub>4</sub> tetrahedra edge-share to form 2D layers held by weak van der Waals interactions. Consequently, these layered chalcogenides are excellent hosts for intercalation chemistry.<sup>50</sup> In the selenide case, the  $T_c$  can be increased from 8 K<sup>13</sup> to 42-44 K by intercalation of alkali metal in liquid ammonia<sup>20,40</sup> or (Li<sub>1-x</sub>Fe<sub>x</sub>OH)<sup>δ+</sup> under hydrothermal conditions.<sup>24,25</sup> Therefore, our goal was to extend this type of chemistry to the sulfides.

We have found the intercalation chemistry of layered FeS to be quite versatile, and we illustrate in Fig. 6.1 the various guest-host phases that can be prepared via hydrothermal routes. Inspired by recent studies on the hydrothermally prepared 42 K superconductor, (Li<sub>1-x</sub>Fe<sub>x</sub>OH)FeSe,<sup>24,25,52? -54</sup> we applied similar intercalation chemistry for FeS using different alkali metal hydroxides. Herein, we report newfound superconductivity in the Li-intercalated FeS phases, and magnetic ordering in the Na-intercalated FeS phases. We find that the superconducting properties depend on preserving an iron square lattice and in electron doping the metallic FeS layer.

## 6.2 Experimental

### 6.2.1 Synthesis

For a typical preparation of (Li<sub>1-x</sub>Fe<sub>x</sub>OH)FeS via the route from **2** to **3** in Fig. 1, 5 mmol Fe powder, 8 mmol of Li<sub>2</sub>S (or thiourea/Na<sub>2</sub>S · 9H<sub>2</sub>O), 1 mmol Sn metal plate

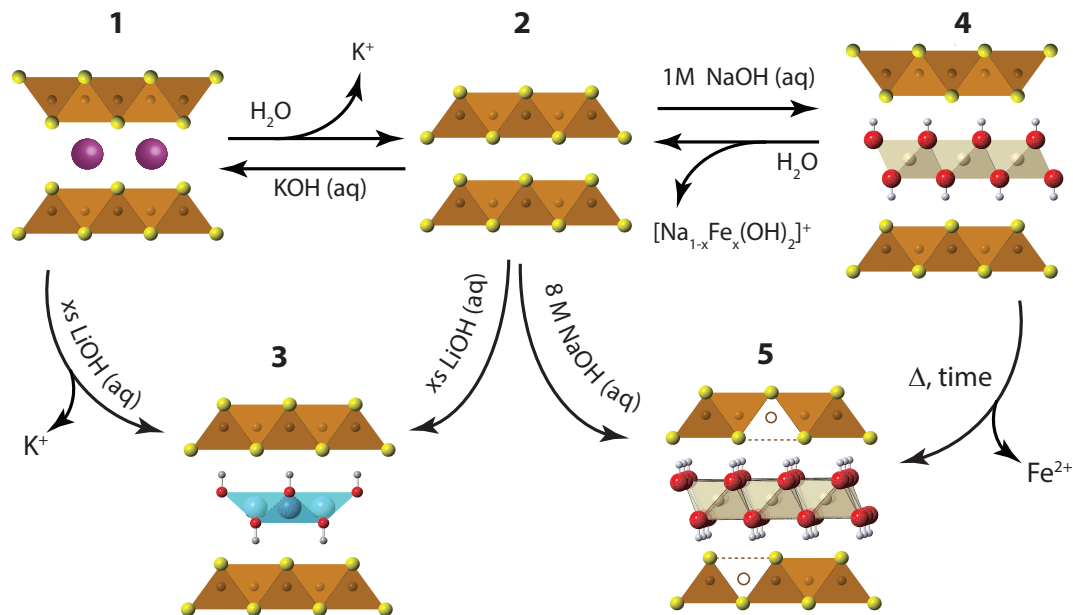


Figure 6.1: Synthetic scheme for the intercalation chemistry of FeS with metal hydroxides and K<sup>+</sup> cations via hydrothermal preparations.

and 72 mmol LiOH·H<sub>2</sub>O were mixed with 10 mL de-ionized (DI) water in a Teflon-lined stainless steel autoclave at 120-200 °C for 3 days. Mainly Li<sub>2</sub>S was used as the sulfur source to avoid possible contamination from other alkali cations such as sodium. Afterwards, the content in the autoclave was washed and centrifuged several times until the supernatant was clear. The remaining product was collected, vacuum dried, and stored in a nitrogen-filled glove box.

For (Li<sub>1-x</sub>Fe<sub>x</sub>OH)FeS prepared via the cation exchange route from **1** to **3** in Fig. 6.1, K<sub>x</sub>Fe<sub>2-y</sub>S<sub>2</sub> single crystals grown from high temperature reactions were mixed with 3 mmol Fe powder, 3 mmol of sulfur source (Li<sub>2</sub>S, thiourea or Na<sub>2</sub>S · 9H<sub>2</sub>O), 1 mmol Sn metal plate and 72 mmol LiOH·H<sub>2</sub>O. The K<sub>x</sub>Fe<sub>2-y</sub>S<sub>2</sub> precursors and reagents were reacted under hydrothermal conditions at 120 °C for 1-3 days. For the growth of the K<sub>x</sub>Fe<sub>2-y</sub>S<sub>2</sub> single crystals, 1.2 g of FeS powder was mixed with 0.266 g of potassium

metal to match the nominal composition of  $\text{KFe}_2\text{S}_2$ . The FeS/K mixtures were loaded in a quartz ampoule inside a nitrogen-filled glovebox, and the ampoules flame sealed under vacuum. In order to avoid oxidation of the samples from breaking of the ampoule due to potassium-induced corrosion of the quartz walls, the sample container was sealed in a larger ampoule. For crystal growth of  $\text{K}_x\text{Fe}_{2-y}\text{Se}_2$ , the mixture was heated to 1030 °C over 10 h and held at 1030 °C for 3 hours to form a homogeneous melt. Subsequently, the melt was slowly cooled at a rate of 6 °C/hour to 650 °C to allow crystal growth.

For the preparation of Na-intercalated phases, we combined 10 mmol of Fe powder, 10-12 mmol of  $\text{Na}_2\text{S} \cdot 9\text{H}_2\text{O}$ , and 5-10 mmol of NaOH in an autoclave with 10 mL of DI water and heated the mixture for 7 days at 120 °C. As described later in the Results section, these samples labeled *inc*-Na-tochilinite are compound **4** in Fig. 6.1. A different series of Na-intercalated samples (**5** in Fig. 6.1) were prepared by utilizing a larger amount of base. The series labeled Na-tochilinite was prepared by combining 10 mmol of Fe powder, 15-20 mmol of  $\text{Na}_2\text{S} \cdot 9\text{H}_2\text{O}$ , 50-80 mmol of NaOH, and 2 mmol of Sn metal plate in an autoclave with 10 mL DI water and heated to 120 °C for 3-7 days.

We also utilized hydrothermal synthesis for the preparation of K-intercalated phases labeled **1** in Fig. 6.1. Phase pure polycrystalline material was prepared by combining 10 mmol of Fe powder, 15 mmol of thiourea, 50-100 mmol of KOH, and 2mmol of Sn metal plate with 10 mL DI water in an autoclave and heated to 160 °C for 5-7 days.

## 6.2.2 Characterizations

Powder X-ray diffraction (XRD) data were collected using a Bruker D8 X-ray diffractometer with Cu  $K\alpha$  radiation,  $\lambda = 1.5418 \text{ \AA}$ . High-resolution synchrotron X-ray diffraction were carried out at Beamline 11-BM at the Advanced Photon Source (APS). Diffraction data were collected between  $0.5^\circ$  and  $46^\circ$  with a step size of  $0.0001^\circ$  using a constant wavelength  $\lambda = 0.414164 \text{ \AA}$  (30 keV). Rietveld and Pawley refinements were carried out using TOPAS software.<sup>66</sup> Microscopic images were examined on a Hitachi SU-70 SEM field emission scanning electron microscope (SEM), and their elemental compositions were determined by energy dispersive X-ray spectroscopy (EDS) using a BRUKER EDS detector. Electron diffraction patterns were obtained using a JEM 2100 LaB<sub>6</sub> transmission electron microscope (TEM) at an acceleration voltage of 200 KeV.

Inductively coupled plasma atomic emission spectroscopy (ICP-AES) data were collected using an Shimadzu ICPE-9000 spectrometer. Standards used for ICP-AES were diluted from 1000 ppm of respective elements purchased from Sigma-Aldrich.

Magnetic susceptibility measurements were performed using a Quantum Design Magnetic Properties Measurement System (MPMS). The volume fractions of superconducting phases were calculated based on the density obtained from Rietveld refinement. Electrical resistivity and heat capacity measurements were performed on a 14 T Quantum Design Physical Properties Measurement System (PPMS).

## 6.3 Results and discussions

### 6.3.1 Li-intercalated phases

We first describe our results utilizing LiOH to intercalate the FeS host. Our starting point is to utilize  $K_xFe_{2-y}S_2$  (**1**) crystals grown from congruently melting the constituent elements. Under hydrothermal and basic conditions, these crystals can either de-intercalate the potassium cations to form mackinawite FeS (**2**), or cation exchange the potassium for cationic layers of  $(Li_{1-x}Fe_xOH)^{\delta+}$  as traced in the reaction from **1** to **3**. Alternatively, we can isolate  $(Li_{1-x}Fe_xOH)FeS$  (**3**) via the method used by previous workers,<sup>59,60,162</sup> whereby polycrystalline material is prepared by the oxidation of iron metal in the presence of a sulfide source and excess amounts of LiOH base. In this reaction (**2** to **3** in Fig. 6.1), mackinawite FeS forms in-situ with the hydroxide layers to yield  $(Li_{1-x}Fe_xOH)FeS$ . We note that Lu *et al.*<sup>162</sup> and Pachmayr *et al.*<sup>59</sup> had previously observed superconductivity in some of their mixed solid-solutions,  $(Li_{1-x}Fe_xOH)FeS_{1-z}Se_z$ , but both studies had concluded that their pure sulfide samples ( $z = 0$ ) were nonsuperconducting.

We found that superconductivity can be established in the intercalated sulfides for both our cation exchange and polycrystalline routes if two conditions are met: 1) the reaction temperature must be less than 160 °C, i.e. mild hydrothermal conditions, and 2) the environment must remain reducing. The latter condition was maintained by the inclusion of tin metal plate as a way to dynamically change the hydrothermal conditions from oxidizing to more reducing.<sup>53</sup> No tin was found in the products as determined from

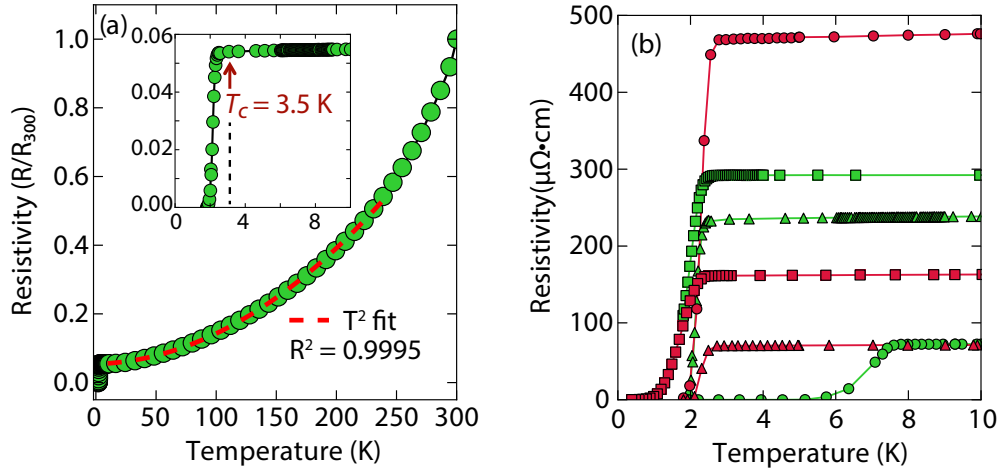


Figure 6.2: (a) Temperature dependent electrical resistivity of superconducting  $(\text{Li}_{1-x}\text{Fe}_x\text{OH})\text{FeS}$  samples prepared via the cation exchange route with thiourea (b) Low temperature resistivity curves for a variety of samples prepared by either thiourea (in green) or  $\text{Na}_2\text{S} \cdot 9\text{H}_2\text{O}$  (in red). For (a), the  $T_c$  is lower and most of the normal state resistivity (up to 250 K) can be fit with  $T^2$ -squared type behavior.

energy dispersive X-ray spectroscopy (EDS).

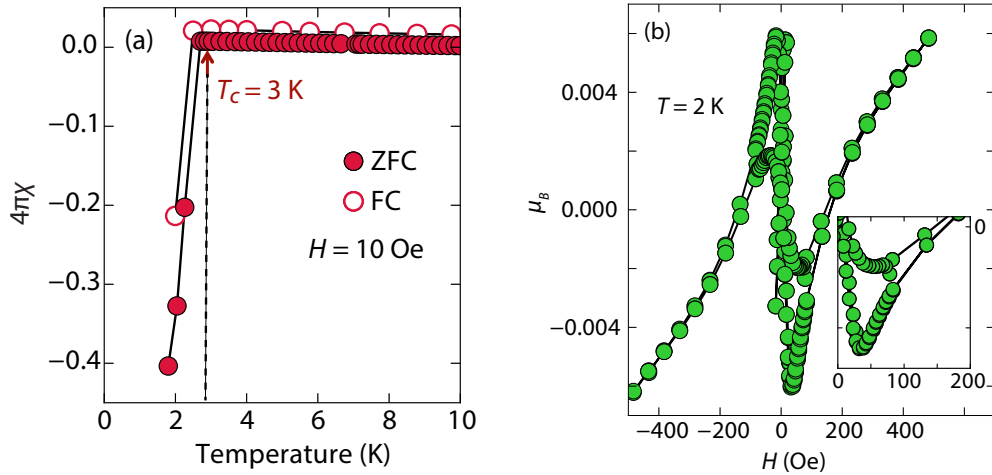


Figure 6.3: Magnetic susceptibility measurements of superconducting  $(\text{Li}_{1-x}\text{Fe}_x\text{OH})\text{FeS}$  at (a) constant field and (b) constant temperature. The  $H_{c1}$  and  $H_{c2}$  of this sample are about 40 and 180 Oe, respectively. The XRD pattern of this sample is shown in Fig. 6.7a.

Magnetization and electrical resistivity measurements revealed that the  $T_c$  of the  $(\text{Li}_{1-x}\text{Fe}_x\text{OH})\text{FeS}$  phases can vary from 3 K to 8 K (Fig. 6.2), with some samples showing

superconducting volume fractions up to 40%, indicative of bulk superconductivity (Fig. 6.3). We must note, however, that due to the proximity of  $T_c$  to the base temperature of our magnetometer (1.8 K) we could not reach full saturation of the diamagnetic signal. Therefore, it is possible that the volume fraction is even higher than 40%.

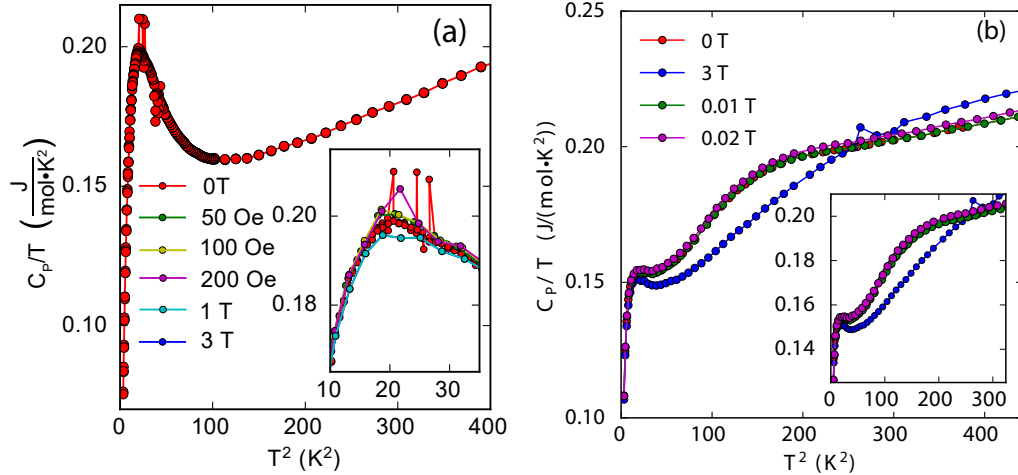


Figure 6.4: Specific heat measurements of (a) LiOH-intercalate FeS and (b) *inc*-Na-tochilinite.

Heat capacity measurements were also carried out in a sample with a  $T_c$  near 3 K, but a large signal peaked near 4.5 K whose intensity is independent of applied magnetic field seems to mask any superconducting signal (Fig. 6.4a). In the similar selenides  $(\text{Li}_{1-x}\text{Fe}_x\text{OH})\text{FeSe}$ , which have a  $T_c$  near 42 K, magnetic ordering in the superconducting state takes place near 10 K due to the iron substituted for lithium in the hydroxide layer.<sup>25,52,54</sup> Seemingly, a magnetic signal proximate to the  $T_c$  of the  $(\text{Li}_{1-x}\text{Fe}_x\text{OH})\text{FeS}$  makes it difficult to evaluate the superconducting properties from heat capacity measurements.

Remarkably, for  $(\text{Li}_{1-x}\text{Fe}_x\text{OH})\text{FeS}$  samples prepared via the cation exchange route, we observed  $T_c$ 's both above and below that of bulk FeS (Fig. 6.2). This result in-

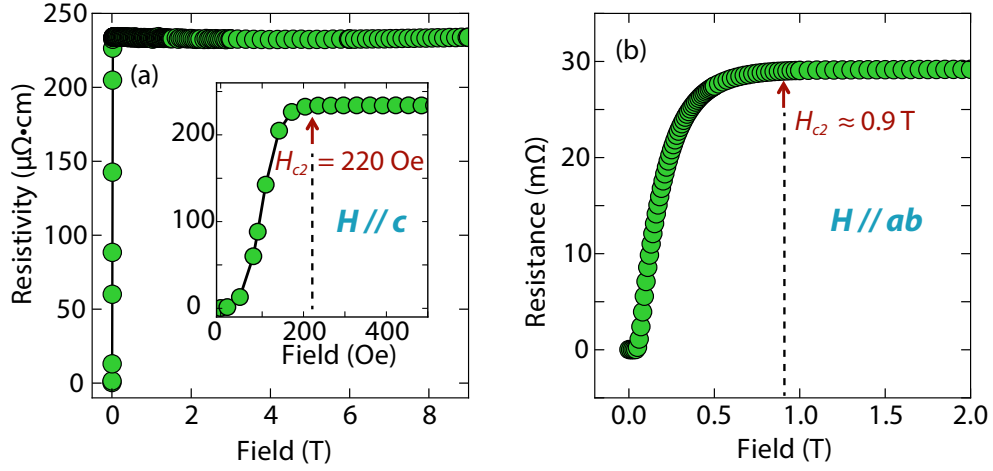


Figure 6.5: Field dependence of electrical resistance for a superconducting  $(\text{Li}_{1-x}\text{Fe}_x\text{OH})\text{FeS}$  sample ( $T_c = 3.5$  K) at 1.8 K. The anisotropy of  $H//c$  and  $H//ab$  are shown in (a) and (b), respectively. Its temperature dependent electrical resistivity is shown in Fig. 2a.

indicates that charge doping into the FeS layer is controlling the critical temperatures in  $(\text{Li}_{1-x}\text{Fe}_x\text{OH})\text{FeS}$ . From our various samples, intercalation by  $(\text{Li}_{1-x}\text{Fe}_x\text{OH})^{\delta+}$  could increase the  $T_c$  of FeS up to 8 K. Figure 6.2b shows the low temperature data near  $T_c$  for various samples and the sample with the lowest residual resistivity ratio also led to the highest  $T_c$  in the series. From  $M$  vs.  $H$  hysteresis loops, the upper critical field ( $H_{c2}$ ) of the sample at 2 K is 180 Oe whilst  $H_{c1}$  was found to be approximately 40 Oe (Fig. 6.3b). Magnetotransport measurements find a slightly higher  $H_{c2}$  near 220 Oe for  $H//c$  at 1.8 K (Fig. 6.5). Therefore, the intercalated compound was found to have an even smaller  $H_{c2}$  than pure FeS where it is approximately 1600 Oe along the  $c$ -direction and 16000 along the  $ab$ -plane.<sup>141</sup>

It is also interesting to note the normal state properties of the intercalated samples. Unlike pristine FeS,<sup>141</sup>  $(\text{Li}_{1-x}\text{Fe}_x\text{OH})\text{FeS}$  samples with the lower  $T_c$  ( $\approx 3.5$  K) displayed nonlinear temperature dependence in the electrical resistivity above  $T_c$  up to approxi-

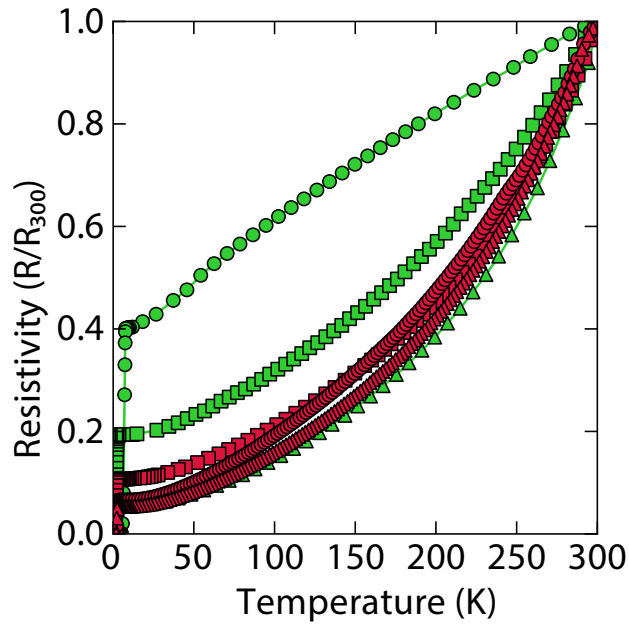


Figure 6.6: Temperature dependence of electrical resistivity for superconducting  $(\text{Li}_{1-x}\text{Fe}_x\text{OH})\text{FeS}$  samples. Green and red colors indicate samples prepared using thiourea and  $\text{Na}_2\text{S} \cdot 9\text{H}_2\text{O}$ , respectively.

mately 250 K, as shown by the  $T^2$ -fit in Fig. 6.2a. Typically,  $T^2$  dependence is associated with Fermi liquid behavior, and linear temperature dependence takes over at higher temperatures (approximately above the Debye temperature) due to electron-phonon scattering.<sup>187</sup> The samples with the lower  $T_c$  exhibit this quadratic behaviour more pronouncedly (Fig. 6.2a and Fig. 6.6). Similar Fermi liquid behaviour has been observed for the normal state in select cuprate superconductors that were overdoped in either electron and hole carriers.<sup>188–190</sup> Another superconductor that exhibits such quadratic dependence of its resistivity near room temperature is  $\text{Ag}_5\text{Pb}_2\text{O}_6$ , which is a three-dimensional electron-gas system.<sup>191</sup> Yonezawa and Maeno ascribe the  $T^2$  behaviour to enhanced electron-electron scattering that arises in superconductors with low electron carrier densities with respect to elements such as alkali and noble metals.<sup>191</sup> Therefore, it is possible that both the lower  $T_c$

and  $T^2$ -behaviour for the sample presented in Fig. 6.2a and Fig. 6.6 are related to having non-optimal charge doping in the FeS layers, and indeed lower carrier concentrations.

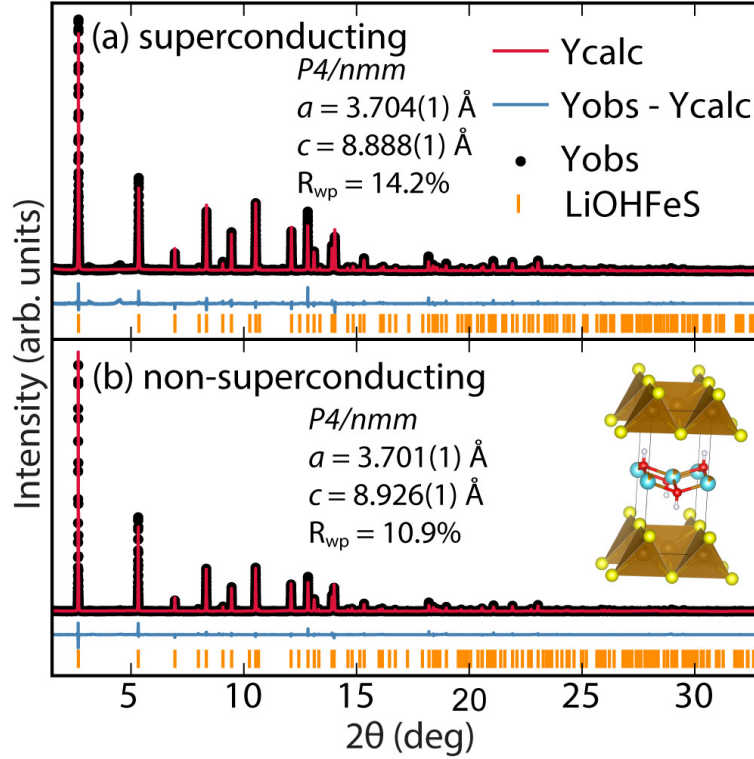


Figure 6.7: Synchrotron XRD patterns of (a) superconducting and (b) non-superconducting  $(\text{Li}_{1-x}\text{Fe}_x\text{OH})\text{FeS}$  prepared under hydrothermal conditions at 160 °C and 200 °C, respectively.

To determine the structure of our superconducting  $(\text{Li}_{1-x}\text{Fe}_x\text{OH})\text{FeS}$  samples, we performed high-resolution synchrotron X-ray powder diffraction (sXRD) as shown in Fig. 6.7. From quantitative analysis of the data, we have provided detailed crystallographic information for two samples in Table 6.2. Upon intercalation, the Fe–Fe bond distances increased from 2.604 Å in bulk FeS<sup>141</sup> to 2.619 Å in  $(\text{Li}_{1-x}\text{Fe}_x\text{OH})\text{FeS}$ , but the FeS<sub>4</sub> tetrahedron remains virtually unchanged both in bond distances and bond angles. There is also an increase in the distance between the iron square sublattices. In mackinawite, that interlayer distance is  $\approx 5.03$  Å,<sup>141</sup> whereas in the  $(\text{Li}_{1-x}\text{Fe}_x\text{OH})$ -intercalated phase

it is 8.89 Å–8.93 Å, further enhancing the two-dimensionality of its electronic structure. Due to the subtle changes in the  $(\text{Li}_{1-x}\text{Fe}_x\text{OH})^{\delta+}$  layer, Rietveld refinements for the superconducting and non-superconducting samples did not show significant differences in their stoichiometries (both close to  $(\text{Li}_{0.85}\text{Fe}_{0.15}\text{OH})\text{FeS}$ ).

Table 6.1: List of  $(\text{Li}_{1-x}\text{Fe}_x\text{OH})\text{FeS}$  samples.

	No.	Temperature (°C)	Sulfur source	Sn (Y/N)	$T_c$ (K)	$a$ (Å)	$c$ (Å)
Powder	1	130	$\text{Li}_2\text{S}$	N	N/A	3.706	8.862
	2	160	$\text{Li}_2\text{S}$	N	N/A	3.704	8.942
	3	160	thiourea	N	N/A	3.696	8.979
	4	180	thiourea	N	N/A	3.702	8.943
	5	200	thiourea	N	N/A	3.702	8.970
	6	120	thiourea	Y	2-3	3.700	8.919
	7	120	$\text{Li}_2\text{S}$	Y	2-3	3.704	8.900
	8	140	$\text{Li}_2\text{S}$	Y	2-3	3.706	8.900
	9	160	$\text{Li}_2\text{S}$	Y	2-3	3.704	8.888
	10	200	$\text{Li}_2\text{S}$	Y	N/A	3.701	8.926
SC	11	120	thiourea	Y	2-8	3.703	8.935
	12	120	$\text{Na}_2\text{S} \cdot 9\text{H}_2\text{O}$	Y	2-6	3.712	8.877
	13	120	$\text{Li}_2\text{S}$	Y	2-4	3.703	8.960

For a more accurate analysis of chemical composition of the  $(\text{Li}_{1-x}\text{Fe}_x\text{OH})\text{FeS}$  phases, we performed inductively coupled plasma atomic emission spectroscopy (ICP-AES). For superconducting and non-superconducting samples, ICP-AES afforded Fe/Li ratios of 1.132 and 1.093, respectively. Since Rietveld refinements for their high-resolution synchrotron data suggested no Fe vacancy in the FeS layers (Table 6.2), the excess amounts of Fe likely resided in the LiOH layers. Therefore, the superconducting samples contains more Fe in the hydroxide layer and consequently more electron doping ( $0.13 e^-$  vs  $0.09 e^-$ ) into the FeS layer. Similarly, Zhou *et al.*<sup>53</sup> have reported that for the selenide analogues, higher  $T_c$ 's were achieved with lower reaction temperatures so that more iron cations could incorporate into the lithium hydroxide layer. Studies on the same system by Clarke *et al.* demonstrated that the iron in the hydroxide layer is  $\text{Fe}^{2+}$  and that iron va-

cancies in the FeSe layer degraded the superconducting properties.<sup>26</sup> Through the cation exchange method demonstrated here, vacancy formation in the FeS layer is less of a factor and achieving sufficient electron doping from the hydroxide layer is the bigger challenge.

We detail the synthesis conditions for various superconducting and non-superconducting samples in Table 6.1. Detailed synthetic conditions are described in the above text, and only temperature, the most important factor, is shown in the table. Lattice constants of only representative samples are shown for duplicate samples. Because Na-tochilinite can be produced with the presence of NaOH,  $\text{Na}_2\text{S} \cdot 9\text{H}_2\text{O}$  was not used as a precursor for powder samples due to its hydrolysis to NaOH and NaSH in solution.  $\text{Li}_2\text{S}$  was the main sulfur source used for powder samples, and every sample prepared with  $\text{Li}_2\text{S}$  has been reproduced at least once. Single crystal samples are not very homogeneous, and their  $T_c$ 's vary from crystal to crystal, but their superconductivity is highly reproducible. Multiple single crystal batches have been reproduced at 120 °C using different sulfur sources with the presence of Sn.

### 6.3.2 Na-intercalated phases

Our next objective was to explore larger alkali metal hydroxides as intercalates. Unlike LiOH, which favors a square lattice commensurate with that of mackinawite FeS, a similar structure for NaOH was not reproduced. Instead, we found a new phase with very few reflections in the XRD powder pattern and its first peak corresponded to a  $d$ -spacing of 5.38 Å. This phase is reminiscent of a natural mineral known as tochilinite, which consists of brucite-type  $\text{Mg}(\text{OH})_2$  layers between mackinawite-like FeS sheets. Natural

Table 6.2: Lattice and structural parameters obtained from Rietveld refinement with synchrotron PXRD data collected at room temperature for a superconducting sample of  $(\text{Li}_{1-x}\text{Fe}_x\text{OH})\text{FeS}$  shown in Fig. 6.7a and a non-superconducting sample shown in Fig. 6.7b. Both samples are fitted to a  $P4/nmm$  space group with 2 formula units in each unit cell ( $Z = 2$ ). Relevant bond distances and bond angles are also presented for each compound. The tetrahedral angles  $\alpha_1$  and  $\alpha_2$  represent the S-Fe-S angles in and out of the basal plane, respectively.

$a = 3.7041(1) \text{ \AA}, c = 8.8877(1) \text{ \AA}, R_{wp} = 14.27 \%, T_c = 3 \text{ K}$						
Atom	Wyckoff site	$x$	$y$	$z$	Occ.	$U_{iso} (\text{Å}^2)$
Li	2b	0	0	0.5	0.848(1)	0.0398(11)
Fe1	2b	0	0	0.5	0.152(1)	0.0398(11)
Fe2	2a	0.5	0.5	0	1	0.0091(2)
O	2c	0.5	0	0.4184(3)	1	0.0174(7)
S	2c	0	0.5	0.1444(2)	1	0.0104(3)
$\alpha_1$ (°)	$\alpha_2$ (°)	Fe-Fe (Å)	Fe-S (Å)	F.U.		
110.55(5)	108.93(3)	2.6192(1)	2.2534(7)	(Li <sub>0.85</sub> Fe <sub>0.15</sub> OH)FeS		
$a = 3.7011(1) \text{ \AA}, c = 8.9257(1) \text{ \AA}, R_{wp} = 10.91 \%, \text{ non-superconducting}$						
Atom	Wyckoff site	$x$	$y$	$z$	Occ.	$U_{iso} (\text{Å}^2)$
Li	2b	0	0	0.5	0.846(1)	0.0380(7)
Fe1	2b	0	0	0.5	0.154(1)	0.0380(7)
Fe2	2a	0.5	0.5	0	1	0.0092(1)
O	2c	0.5	0	0.4182(2)	1	0.0141(5)
S	2c	0	0.5	0.1439(1)	1	0.0102(2)
$\alpha_1$ (°)	$\alpha_2$ (°)	Fe-Fe (Å)	Fe-S (Å)	F.U.		
110.47(3)	108.98(2)	2.6171(1)	2.2527(4)	(Li <sub>0.85</sub> Fe <sub>0.15</sub> OH)FeS		

tochilinite is quasi-commensurate and its (001) reflection has a  $d$ -spacing of  $10.72 \text{ \AA}$ , which is close to twice our first reflection. Therefore, if the first peak of our new phase is the (002) reflection, it would indicate that the FeS layers are stacked in a body-centered fashion. Since we only observe (00 $l$ ) reflections in our new phase, the square and hexagonal sheets are completely incommensurate to each other in the  $ab$ -plane. Henceforth, we refer to this phase as *inc*-Na-tochilinite (4 in Fig 6.1).

We found the new *inc*-Na-tochilinite to always coexist with some residual mackinawite FeS (Fig. 6.8). The ratio between *inc*-Na-tochilinite and mackinawite FeS was increased by using less  $\text{Na}_2\text{S} \cdot 9\text{H}_2\text{O}$  and decreased with prolonged ultrasonication, indi-

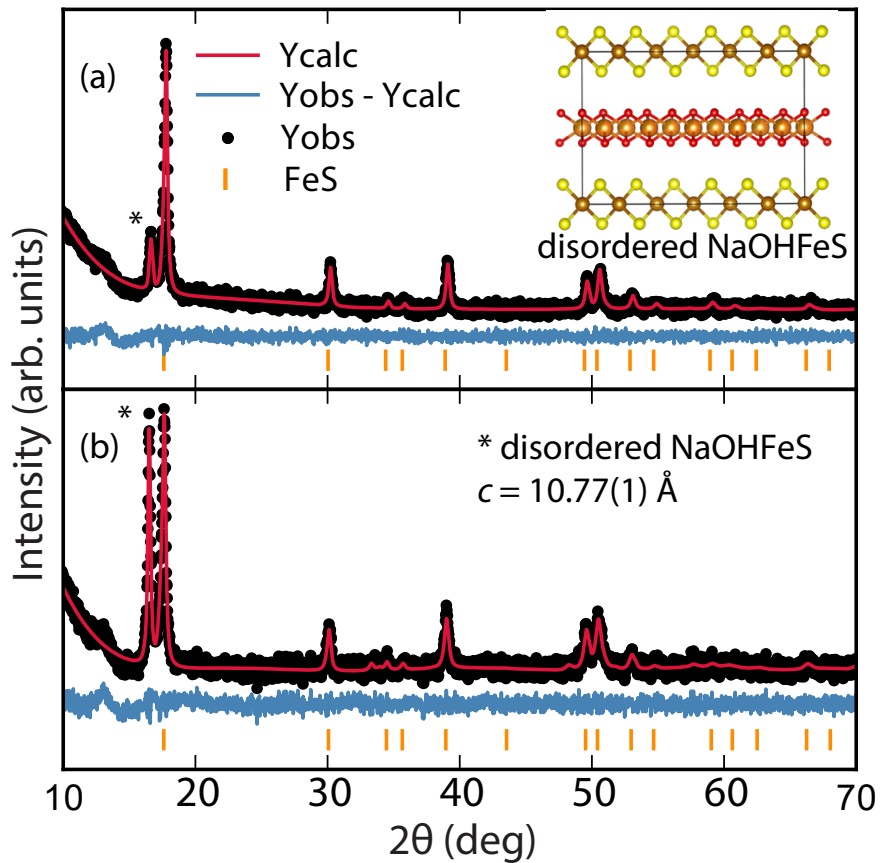


Figure 6.8: XRD patterns of mixtures of disordered NaOH intercalated FeS (indicated by \*) and tetragonal FeS (indicated by tick marks) with significantly more tetragonal FeS in (a) than (b). The magnetic susceptibility of (a) and (b) are shown in Fig. 6.10 and Fig. 6.9, respectively.

cating conversion of *inc*-Na-tochilinite to FeS by de-intercalation and dissolution of the metal hydroxide layer. The equilibrium between the two phases is indicated in the steps between **2** and **4** in Fig. 6.1.

At low fields, we observed two transitions at 5 K and 15 K (Fig. 6.9a). The 5 K transition was more pronounced for a sample that contained less *inc*-Na-tochilinite and more mackinawite FeS impurity (Figs. 6.9 and Fig. 6.10). Therefore, the 5 K anomaly likely corresponds to the superconducting transition of FeS ( $T_c \approx 4.5$  K). Although the transition at  $\approx 15$  K in the zero-field cooled (ZFC) curve (Fig. 6.9a) appears to indicate

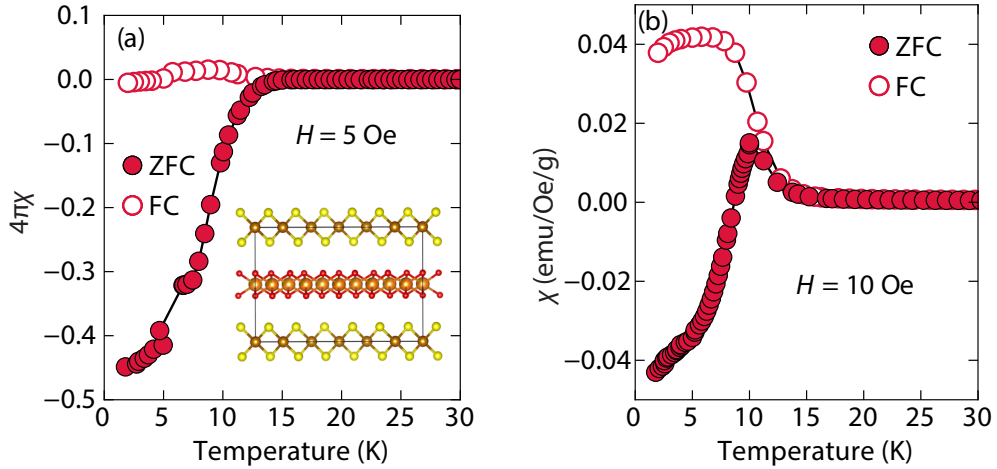


Figure 6.9: F

eS]Magnetic susceptibility of *inc*-Na-tochilinite,  $[(\text{Na}_{1-x}\text{Fe}_x)(\text{OH})_2]\text{FeS}$ , as a function of temperature with an applied external fields of (a) 5 Oe and (b) 10 Oe.

Meissner screening due to superconductivity, the negative signal may actually correspond to long-range ordering such as ferro- or ferrimagnetism. If the internal moment of a ferromagnetic material is of sufficient strength and aligned opposite to a weak external field, then the ZFC curve will display negative susceptibility below the Curie temperature. To resolve this ambiguity, we increased the external field of the magnetization measurements from 5 Oe to 10 Oe (Fig. 6.9). The field cooled (FC) curves better indicate a clear ferromagnetic transition in *inc*-Na-tochilinite near 15 K. Therefore, *inc*-Na-tochilinite does not appear to be a superconductor based on the current magnetization data.

We also performed temperature-dependent resistivity measurement down to 2 K on a pressed pellet of *inc*-Na-tochilinite. We did not observe a superconducting transition, but instead semiconducting behaviour (Fig. 6.12). We note, however, that similar temperature-dependent behaviour was observed for pressed pellets of FeS powders,<sup>94</sup> even though our recent studies of of single crystal FeS samples demonstrated that it is

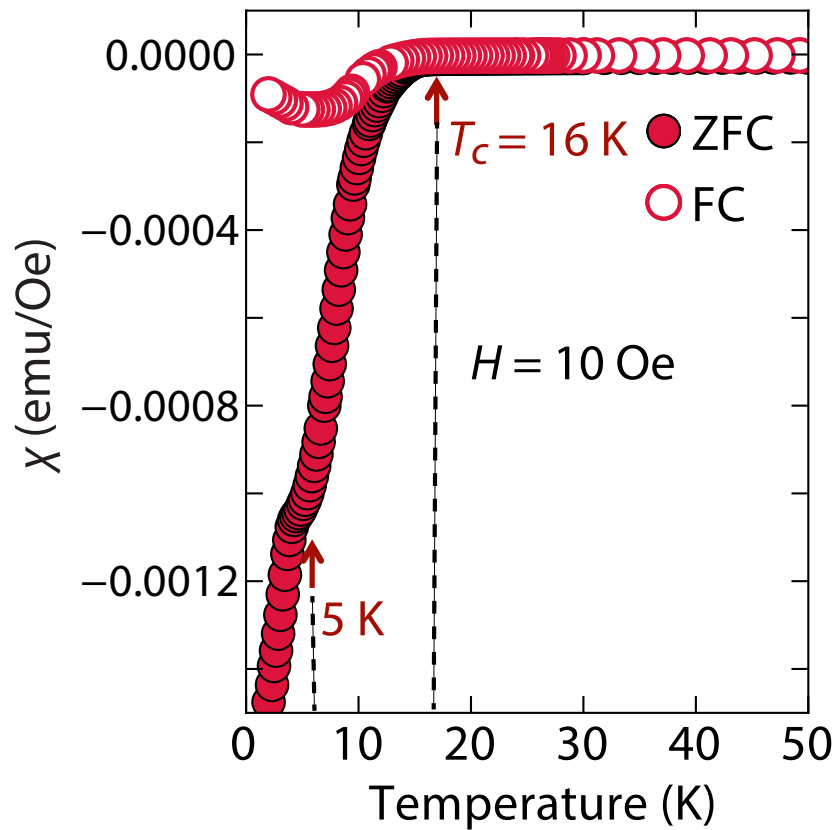


Figure 6.10: Temperature dependent magnetic susceptibility measurement of *inc*-Na-tochilinite with tetragonal FeS as a major phase. Its XRD pattern is shown in Fig. 6.8a

indeed metallic in the normal state.<sup>141</sup> We attribute this disparity between polycrystalline and single crystal transport measurements of FeS to effects from grain boundaries and surface oxidations, typical for pressed pellets of micaceous materials. Therefore, although the current resistivity data of polycrystalline *inc*-Na-tochilinite displays semiconducting behaviour, its true state could be metallic, similar to the Li-intercalated FeS phases in the current study.

Magnetization ( $M$ ) versus applied field ( $H$ ) measurements further clarify the true ground state of *inc*-Na-tochilinite (Fig. 6.11). The  $M$  vs.  $H$  curves suggest ferromagnetic behavior as the isotherm of the field sweep at 5 K (Fig. 6.11b) displayed the typical hys-

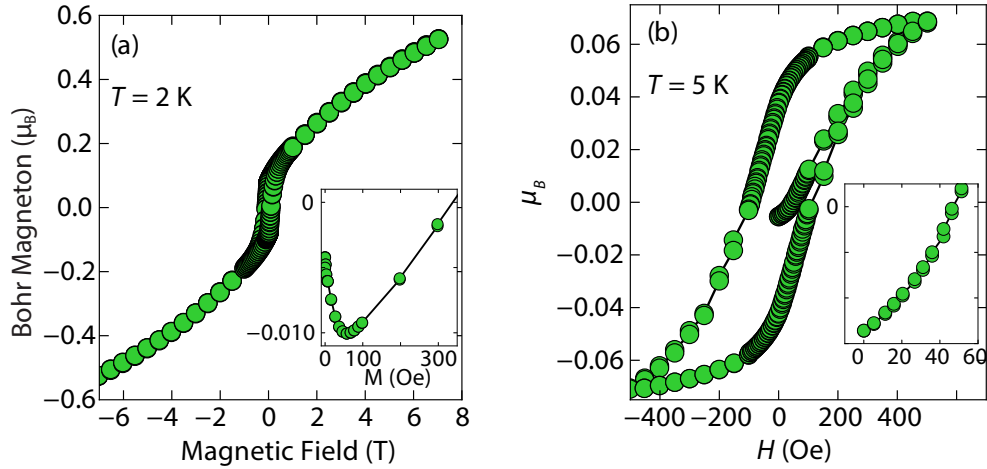


Figure 6.11: Magnetization versus field measurements of *inc*-Na-tochilinite,  $[(\text{Na}_{1-x}\text{Fe}_x)(\text{OH})_2]\text{FeS}$ , at 2 K. Inset shows the small diamagnetic region from the small amount of superconducting FeS present as an impurity phase. (b)  $M$  vs.  $H$  measurement for the same sample at 5 K. Inset indicates that the diamagnetic signal is lost above 5 K, which is above the  $T_c$  of FeS.

teresis loop of ferro- and ferrimagnets. The diamagnetic signal observed for the isotherm at 2 K (Fig. 6.11a inset) was therefore likely due to the superconducting FeS phase present as an impurity, which has a  $T_c$  near 4.5 K.<sup>141</sup> At 5 K, this diamagnetic signal is lost (Fig. 6.11b inset). Although the new *inc*-Na-tochilinite phase is likely to be either ferro- or ferrimagnetic below 15 K, it does exhibit other interesting anomalies. The low temperature transition likely due to long-range magnetic ordering did not appear as a well defined transition in the heat capacity measurements (Fig. 6.4b). Instead, a broad anomaly occurred below 15 K, which was suppressed with a field of 3 T.

By changing the synthesis conditions of the hydrothermal reactions, the NaOH-intercalated FeS system can be stabilized into a quasi-commensurate tochilinite phase (Fig. 6.13a), which we refer to as Na-tochilinite. This quasi-commensurate phase was prepared by utilizing more concentrated solutions of NaOH (5 to 8 M) in the hydrother-

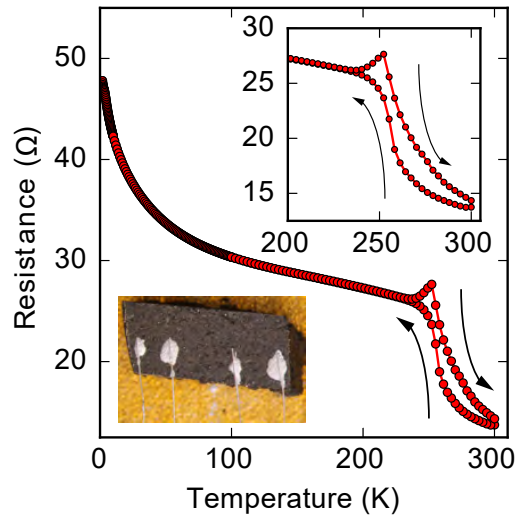


Figure 6.12: Electrical resistance of *inc*-Na-tochilinite as a function of temperature. The measurement was carried out on a pressed pellet from powders.

mal reactions. Significantly less tetragonal FeS was recovered (Fig. 6.13a) with Na-tochilinite, and this phase did not easily revert to FeS by ultrasonication, indicating its stability with respect to *inc*-Na-tochilinite. Using the crystal structure of the naturally occurring mineral known as ferrotochilinite ( $2(\text{Fe}_{1-x}\text{S}) \cdot 1.8[(\text{Mg}, \text{Fe})(\text{OH})_2]$ ),<sup>192</sup> with lattice parameters,  $a = 5.37 \text{ \AA}$ ,  $b = 15.65 \text{ \AA}$ ,  $c = 10.72 \text{ \AA}$ , we extracted by Pawley fits the lattice parameters of our Na-tochilinite (Fig. 6.13a) The lattice parameters after convergence were found to be  $a = 5.18(1) \text{ \AA}$ ,  $b = 15.62(4) \text{ \AA}$ ,  $c = 11.14(4) \text{ \AA}$  and  $\beta = 95.07(10)^\circ$  at room temperature.

Given the difficulty in elucidating the structure of these heterolayered materials by powder XRD, we have also performed electron diffraction (ED). We present two ED patterns with the  $(hk0)$  reflections that were difficult to resolve from powder XRD—one for mackinawite FeS and the other for Na-tochilinite. Along the  $[001]$  zone axis, the ED pattern of FeS (Fig. 6.14a) clearly demonstrates a square lattice corresponding to its

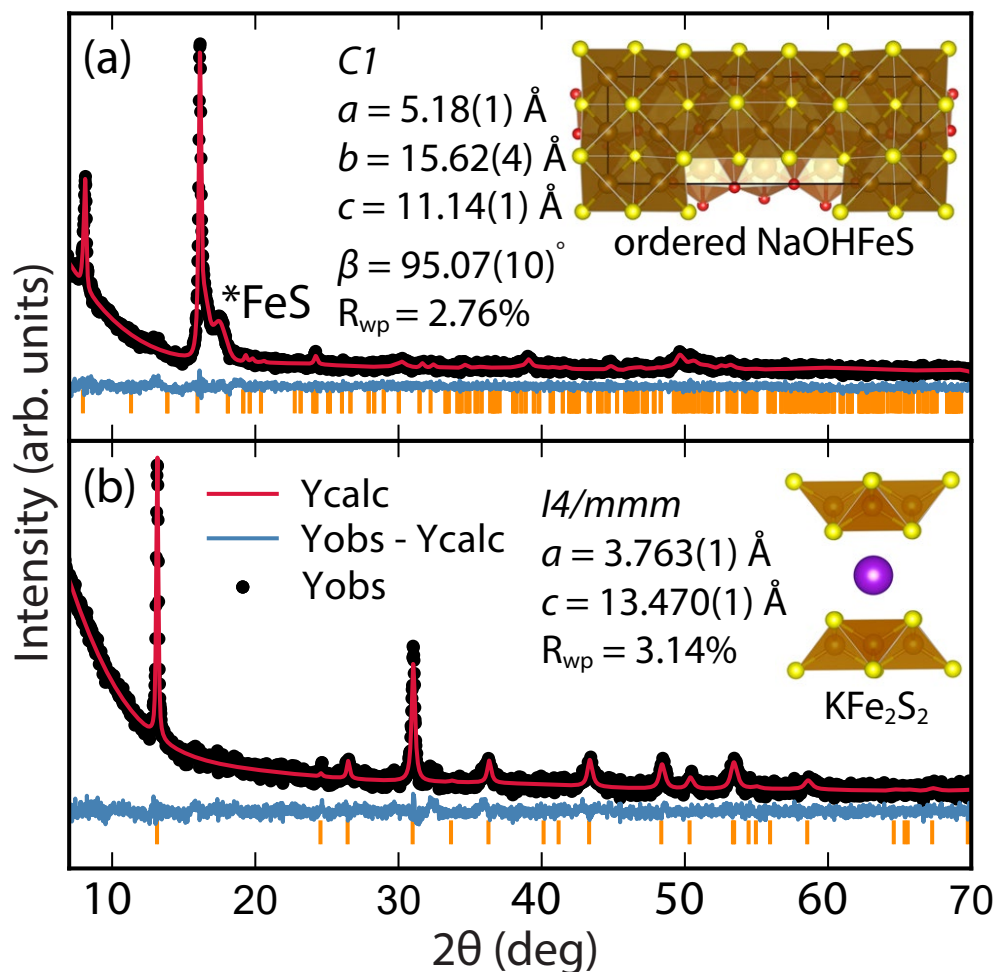


Figure 6.13: (a) Pawley fit to the XRD pattern of hydrothermally prepared Na-tochilinite and (b) Rietveld fit to the XRD data of  $K_xFe_{2-y}S_2$ .

simple primitive tetragonal structure. For Na-tochilinite, additional satellite reflections emerge in addition to the square lattice of FeS (Fig. 6.14b). Upon closer inspection the seemingly 4-fold symmetry of the brighter reflections in Na-tochilinite is actually a 2-fold axis. The angle between the cross-sections connecting the (200) to  $(\bar{2}00)$  and (060) to  $(0\bar{6}0)$  reflections is about  $93^\circ$ , which is close to the monoclinic angle found from XRD ( $\beta = 95.07(10)^\circ$ ). Therefore, the monoclinic distortion of the FeS square lattice in Na-tochilinite is clearly reproduced in the ED along with the satellite reflections indicating

the intercalation of the FeS layers. The lattice constants  $a$  and  $b$  extracted from ED are  $5.2(2) \text{ \AA}$  and  $15.9(2) \text{ \AA}$ , respectively—in good agreement with the XRD analysis.

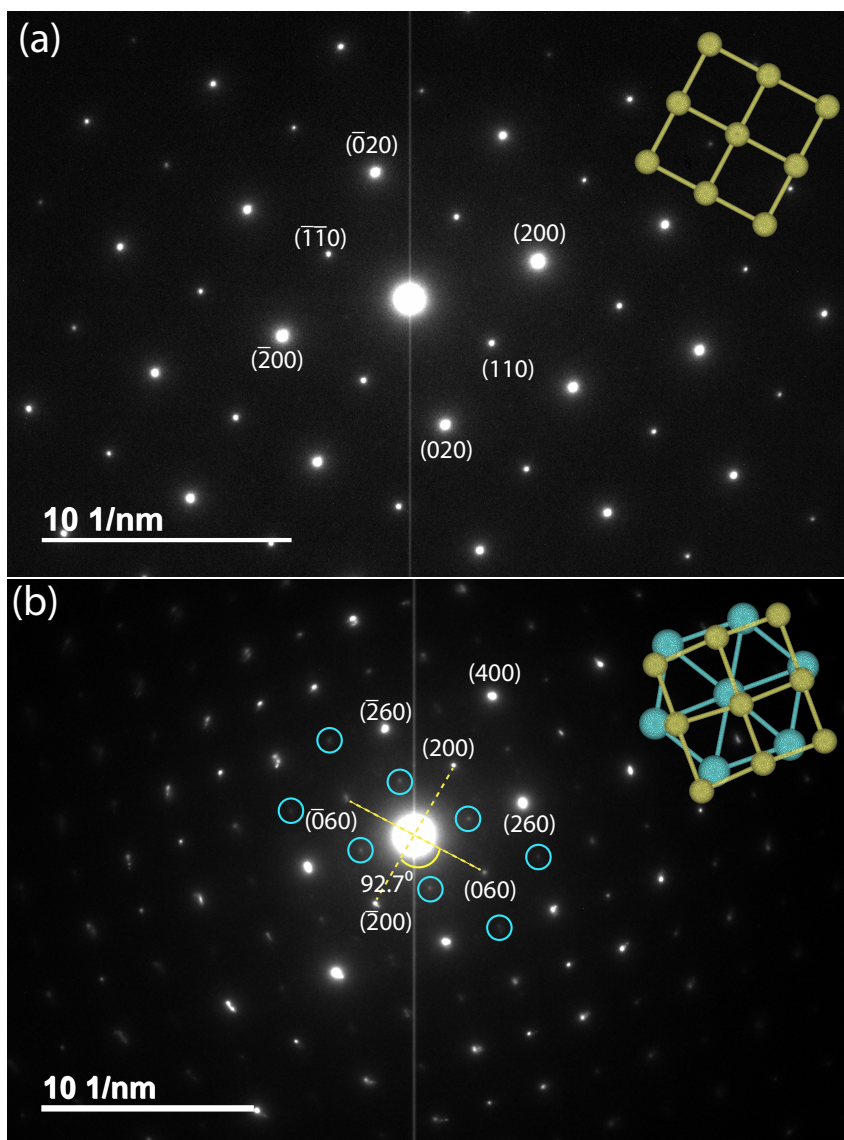


Figure 6.14: Electron diffraction patterns along the zone axis [001] of (a) FeS and (b) Na-tochilinite, respectively. Some weak diffraction spots of Na-Tochilinite are highlighted by blue circles. Projections of tetragonal and hexagonal lattices are shown in yellow and blue, respectively.

Next, we discuss the nature of the chemical composition of Na-tochilinite. As in some natural minerals,<sup>193</sup> we can formulate the stoichiometry as  $[(\text{Na}_{1-x}\text{Fe}_x)(\text{OH})_2]\text{FeS}$ , and ICP-AES analysis provided an Fe/Na ratio of 2.99. Therefore,  $[(\text{Na}_{0.5}\text{Fe}_{0.5})(\text{OH})_2]\text{FeS}$

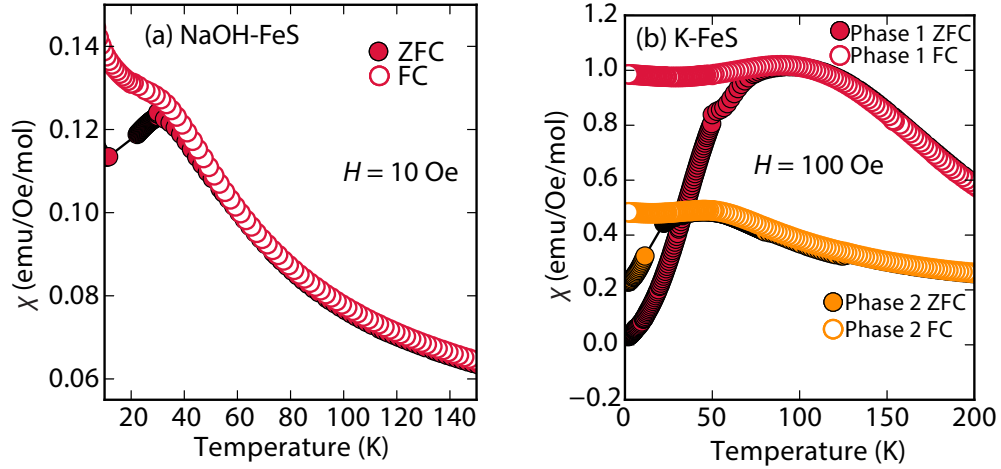


Figure 6.15: Magnetic susceptibility measurements of (a) Na-tochilinite and (b)  $K_xFe_{2-y}S_2$ , respectively. The lattice constant  $c$  for Phase 1 and Phase 2 in (b) is 13.627 and 13.470 Å, respectively.

is the proposed chemical formula since the ratio of Fe to Na in the tochilinite is  $(1 + x)/(1 - x) = 2.99$ . We can modify the formula by considering the number of iron vacancies in the FeS layers,  $y$ , and the phase fraction of mackinawite FeS impurity,  $f$ . The formula is therefore re-written as  $(1 + x - y)/(1 - x) = 2.99 \times (1 - f)$ . If we estimate the limits based on diffraction data as  $y < 0.2$  and  $0.1 < f < 0.2$ , then  $x$  can vary between  $0.41 < x < 0.52$ . This result suggests that approximately half of the cations in the hydroxide layers are filled by iron cations, and in order to charge balance the two  $OH^-$  groups of the hexagonal brucite layer, the nature of that iron site must be in the form of  $Fe^{3+}$ . Whilst ICP-AES could not determine the number of hydroxide groups, crystal chemistry arguments support  $M(OH)_2$  for the spacer layer since this is how the hexagonal brucite is formulated. Furthermore, the highly reactive and pyrophoric mineral known as “white rust” consists of  $Fe(OH)_2$  layers that crystallize in the  $CdI_2$ -type structure.<sup>194</sup> By oxidizing to  $Fe^{3+}$ , such a layer would be stabilized by the presence of either  $Na^+$  or vacancies, and

indeed natural tochilinites exhibit significant amounts of Fe vacancies (up to 20%).<sup>195?</sup>

Rather than displaying superconductivity as in the LiOH-intercalated systems or long-range ferro- or ferrimagnetism as in *inc*-Na-tochilinite, Na-tochilinite displays broad features in the magnetization reminiscent of short-range antiferromagnetic behavior (Fig. 6.15a). The splitting of the ZFC and FC curves likely indicate some degree of spin glassiness. The presence of iron vacancies and distortion of the iron square sublattice are some of the likely reasons that Na-tochilinite does not produce a well-defined transition in the magnetization data. Interestingly, Parise *et al.* found through neutron diffraction that  $\text{Fe}(\text{OH})_2$  exhibits long-range magnetic ordering with each sheet consisting of ferromagnetically coupled iron centers, and each sheet anti-aligned to each other.<sup>194</sup> Future neutron diffraction experiments on both incommensurate and quasi-commensurate Na-tochilinites would reveal the nature of the interesting evolution of long-range magnetic ordering arising from the hydroxide layer.

### 6.3.3 K-intercalated phases

Efforts to incorporate KOH layers into FeS hosts resulted in cationic  $\text{K}^+$  intercalation instead. When hydrothermal reactions of Fe powder with KOH and a sulfide source were undertaken, the XRD pattern revealed a phase pure sample similar to the  $\text{K}_x\text{Fe}_{2-y}\text{S}_2$  prepared using solid-state routes (Fig. 6.13b). In addition, its pattern could be well fit by Rietveld refinement using the crystal structure of  $\text{K}_x\text{Fe}_{2-y}\text{S}_2$  with the space group  $I4/mmm$ . Its layer spacing (lattice constant  $c$ ) is 13.47 Å, which is comparable to the reported 245-type ( $I4/m$ , 13.599 Å)<sup>108</sup> and 122-type ( $I4/mmm$ , 13.546 Å) compounds.<sup>22</sup>

EDS analysis gave a composition of  $K_{1.1}Fe_{1.6}S_2$  and its magnetic susceptibility displayed broad antiferromagnetic features around 45 K ( $c = 13.470 \text{ \AA}$ ) and 96 K ( $c = 13.627 \text{ \AA}$ ) for samples with different layer spacings (Fig. 6.15b). The ZFC and FC curves do not trace each other as well, which raises the possibility that these materials may display some spin glassiness as well. Since the transitions are fairly broad, it is likely that long-range antiferromagnetic ordering is never observed but rather some form of low-dimensional or short-range antiferromagnetic order. Although not superconducting, it is remarkable that we could prepare via hydrothermal routes such ternary phases since these have previously been prepared only by high temperature solid state techniques.

While we did not find superconducting phases containing potassium, we did demonstrate that the synthetic temperature for the preparation of  $K_xFe_{2-y}S_2$  can be lowered from about 1000 °C to 160 °C through hydrothermal methods. Without KOH, single crystals of  $K_xFe_{2-y}S_2$  can be completely converted to mackinawite FeS. Therefore, the conversion between  $K_xFe_{2-y}S_2$  and tetragonal FeS is fully reversible, as traced by the equilibrium reaction between **1** and **2** in Fig. 6.1. With further work on reducing the iron vacancies, the potassium intercalated phases could be made superconducting. To confirm this, we started to apply this route to the selenide system without optimization, and  $K_xFe_{2-y}Se_2$  was prepared despite the presence of tetragonal FeSe. The implication of these results are that this hydrothermal route can lead to pure 122 type of layered compounds or the corresponding deintercalated tetragonal system. In addition, this hydrothermal route can be advantageous over solid-state route to avoid high temperature impurity phases or targeting compounds not thermodynamically stable at low temperature.

## 6.4 Conclusions

In conclusion, we have demonstrated that metal hydroxides can be intercalated into tetragonal mackinawite-type FeS via hydrothermal routes, and that new superconductors can be prepared in this manner. Given that FeS is a metastable phase, it is of paramount importance that we continue to explore novel low temperature routes towards mineral-inspired superconductors. Whilst we have enhanced  $T_c$  to 8 K through these charge-doping hydroxide layers, we have also demonstrated that FeS can serve as a suitable host for various guests species acting as bases. The differences in going from  $\text{Li}^+$  to  $\text{Na}^+$  to  $\text{K}^+$  are remarkable in the vastly different structure types that were stabilized and the physical properties that are manifested. These results point to the exciting possibility of utilizing both size and charge parameters of other guests species, such as amines, to ultimately enhance the superconductivity of sulfide-based materials. Furthermore, the fact that heterostructures could be stabilized points to mackinawite-type FeS as a possible new 2D chalcogenide to be incorporated into other functional 2D materials. The field of vertical 2D heterostructures has exciting possibilities for constructing entirely new functional materials, and mackinawite-type FeS could be a new building block in such structures.

## Chapter 7: Conclusions and Future Work

### 7.1 Conclusions

To summarize the entire dissertation, we have made significant breakthroughs at two fronts: 1) developing a generic synthetic paradigm for metastable TTMCs and 2) fabricating heterolayered iron-chalcogenides using hydrothermal methods.

We demonstrated that metastable layered tetragonal FeS single crystals could be synthesized by topochemical deintercalation of a thermodynamically stable template precursor, such as  $K_xFe_{2-y}S_2$ . The FeS samples prepared using this method is free of Fe vacancy and showed superconductivity below 4.5 K and strong anisotropy. To further demonstrate that our synthetic scheme is not limited to iron chalcogenides, we extended it to other transition metal chalcogenides. We have prepared tetragonal layered CoSe single crystal and CoS powders by topochemical deintercalation of  $K_xCo_2Ch_2$  ( $Ch = Se$  and  $S$ ). This was the first time that the tetragonal FeSe analogue was discovered for other transition metals. By carrying out the reactions at room temperature, the amount of thermal energy was too low for a major structural reconfiguration from the tetragonal structure to the more common hexagonal phase with the NiAs-type structure. Hence, metastable and tetragonal forms of the binary  $CoCh$  phases were stabilized kinetically for the first time. Being analogues to the FeSe and FeS superconductors, the properties of CoSe and CoS

are quite different as they displayed weak itinerant ferromagnetism below about 10 K.

Instead of using a deintercalation approach, heterolayered *FeChs* can be prepared by intercalation or ion-exchange.  $(\text{Li}_{1-x}\text{Fe}_x\text{OH})\text{FeCh}$ , can be prepared by ion-exchange of  $\text{K}^+$  with  $\text{LiOH}$ , or more precisely  $(\text{Li}_{1-x}\text{Fe}_x\text{OH})^+$ , using the  $\text{K}_x\text{Fe}_{2-y}\text{Ch}_2$  precursor or topochemical intercalation of  $\text{LiOH}$  into *in situ* formed *FeCh* formed *in situ* under hydrothermal conditions. Using this method, we discovered a superconducting phase diagram in the  $(\text{Li}_{1-x}\text{Fe}_x\text{OH})\text{FeCh}$  systems. By carrying out the hydrothermal syntheses with  $\text{NaOH}$  instead of  $\text{LiOH}$  as the base, we managed to synthesize a new  $\text{NaOH}$ -intercalated  $\text{FeS}$ . Compared to  $(\text{Li}_{1-x}\text{Fe}_x\text{OH})\text{FeS}$ ,  $[(\text{Na}_{1-x}\text{Fe}_x)(\text{OH})_2]\text{FeS}$  is quite remarkable in that it is truly a layered heterostructure whereas the former contains two compatible square lattices to form an overall tetragonal structure. Furthermore, heterolayers of  $[(\text{Na}_{1-x}\text{Fe}_x)(\text{OH})_2]\text{FeS}$  can be incommensurate or commensurate, and they result in ferromagnetism below 16 K. These results demonstrate that upon intercalation new properties can emerge, and by carefully selecting these adducts, such properties can be controlled.

Throughout this work, the  $\text{ThCr}_2\text{Si}_2$ -type compounds, such as  $\text{KCo}_2\text{Se}_2$  and  $\text{K}_x\text{Fe}_{2-y}\text{S}_2$ , proved to be very effective templates for post-synthetic modifications. The typical  $\text{AM}_2\text{Ch}_2$  compounds held by ionic forces and tend to be thermodynamically stable. Thus, they can be prepared by high temperature solid-state methods. Subsequently, these stable ternary phases can be utilized as template precursors to new metastable phases via deintercalation of or ion-exchange with the *A* cations under basic aqueous conditions. Our method may provide a generic pathway for metastable tetragonal layered chalcogenides, as there are hundreds of the  $\text{ThCr}_2\text{Si}_2$ -type transition metal chalcogenides reported in literature.<sup>196</sup>

## 7.2 Future Work

As the story is about to conclude here, I would like to quote a saying from the film *the Matrix*: "Everything that has a beginning has an end". Indeed all stories need endings, like the Matrix trilogy ending with Neo saving the world. I was so fascinated with the movie that I have been curious about what would happen next, as the ending also revealed a new dawn upon both the machine world and the city of Zion. Like a good film, I hope that the findings of this work will provides inspirations for beginnings of new stories.

### 7.2.1 Mechanisms of the Hydrothermal Process

We proposed a self-assembled template hypothesis in Chapter 2 for the mechanism of the hydrothermal process. It is of great interest to a broader chemistry community to follow up this investigation, as such a method can provide a universal framework for a variety of layered materials, especially heterolayered structures.

To test this hypothesis, the first step is to test if these hydrothermal reactions under non-basic conditions would lead to tetragonal TTMCs, as the  $\text{SH}^-$  ions crucial for forming the cluster shown in Fig. 2.1a are only stable under basic conditions. However, without strong base, Fe will not be dissolved to form  $\text{Fe}^{2+}$ . Therefore we will choose a chalcogenide source with stable  $\text{Fe}^{2+}$  complexes, which slowly gives out  $\text{Fe}^{2+}$  to allow template-forming and crystal growth instead of immediate precipitation of amorphous FeS. Without a base, there will be no  $\text{Fe-HS}^-$  clusters to form the template, and we expect that octahedrally coordinated  $\text{FeCh}$  compounds will be obtained. For initial tests, ferrocene can be used as the  $\text{Fe}^{2+}$  source due to its high stability.

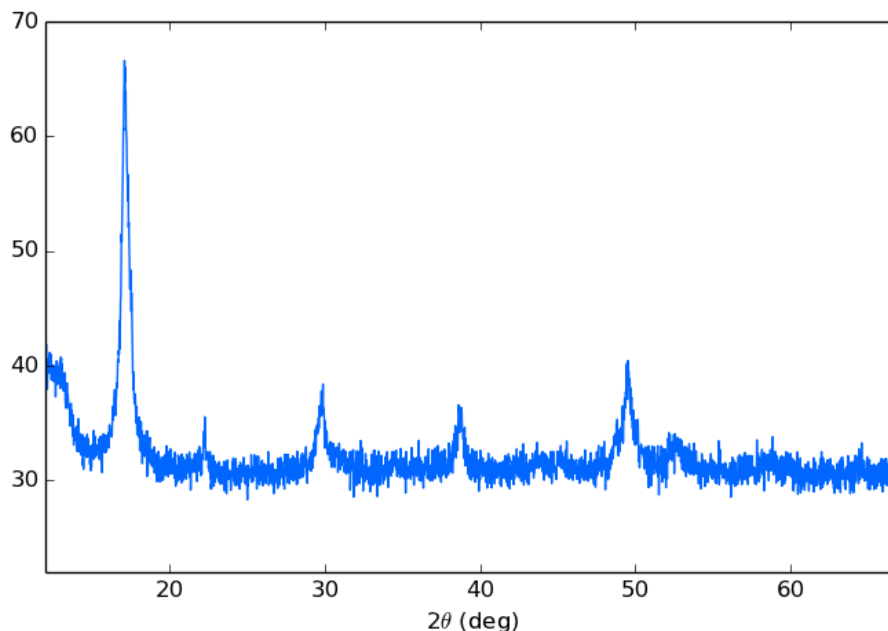


Figure 7.1: XRD pattern of a crystalline tetragonal FeS sample hydrothermally prepared under basic conditions using ferrocene as the Fe source.

A preliminary test with ferrocene was successful. Powder tetragonal FeS (Fig. 7.1) samples have been prepared by reaction of ferrocene and thiourea (or sodium sulfide) in a NaOH aqueous solution (PH = 14 at RT) in an autoclave at 150 °C for 5 d. Interestingly, a similar reaction without the presence of base reported by Luo *et al.* resulted in the thermodynamically stable hexagonal FeS phase.<sup>197</sup> This may indicate that without SH<sup>-</sup> to form tetrahedrally coordinated Fe<sup>2+</sup> clusters, more stable octahedrally coordinated network will form.

This is merely a first step to test this template hypothesis. Further work needs to be carried out on identifying these clusters and condensed Fe<sub>4</sub>S<sub>4</sub> chains or slabs. A possible characterization means to test this is to carry out the reactions under air-free conditions, and aliquots of the supernatant in controlled time intervals. Each of the extracted solutions will be tested on NMR and MS to search for possible clusters and templates.

Another study for the precipitates will require the experiments being carried out *in situ* at a synchrotron XRD source to probe the gradual formation of TTMCs.

## 7.2.2 From the Bulk to Nanosheets

For TMDs the concept of nanosheets is not new, and almost all bulk TMDs can be broken down to the nanoscale by either mechanical or solution-mediated exfoliation.<sup>198–203</sup> However, this synthetic strategy remains rather untapped for TTMCs. Considering both TMDs and binary TTMCs consist of 2D layers held by weak van der Waals forces, fabrication of TTMC nanosheets may be quite feasible utilizing similar techniques. When bulk materials are dimensionally confined, interesting quantum effects can emerge. For example, bulk MoS<sub>2</sub> is an indirect band gap semiconductor, whereas monolayer MoS<sub>2</sub> exhibits a direct band gap and displays orders of magnitude higher photoluminescence.<sup>203</sup> Therefore, it is reasonable to assume that new properties may emerge from TTMC nanosheets. Indeed monolayered FeSe deposited on STO substrate has been reported to show a staggering high  $T_c$  varying from 55 K to 110 K depending on the study.<sup>27,29,204</sup> Its  $T_c$  is increased 10-fold from bulk FeSe and higher than any known bulk Fe-based superconductors. Therefore, TTMC nanosheets are promising new materials yet to be explored. Since other binary TTMCs such as FeS, CoSe and CoS are metastable, synthetic strategies other than those used for FeSe will be required. For example, chemical vapor deposition may be unfeasible due to the requisite higher temperatures. Instead of bottom-up syntheses, a top-down approach such as exfoliation of bulk materials could provide a more practical means to fabricate nanosheets of TTMCs such as CoSe.

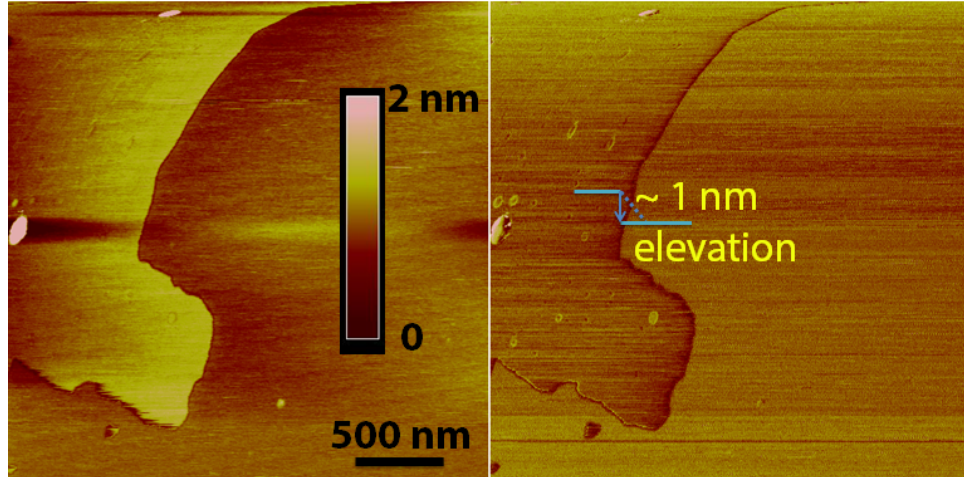


Figure 7.2: Atomic force microscopy image of a thinlayered CoSe sheet deposited on a mica substrate. The height-elevation of about 1 nm suggests a bilayer CoSe sheet.

We have carried out the first step to fabricate ultra-thin layered TTMCs. We applied a generic exfoliation technique to CoSe single crystals. Those crystals were exfoliated with the assistance of ultrasonication in isopropanol. We were able to deposit a two-layer thick CoSe sheet on a mica substrate as shown in Fig. 7.2. We will carry out more tests on CoSe with different conditions and solvents, and once we have an optimal condition we will apply it to other TTMCs.

### 7.2.3 Heterolayered Structures by Design

Another interesting direction for 2D materials, is the building of new heterostructures by stacking them in particular sequences, as has been explored for TMDs.<sup>205</sup> These heterostructures could offer unique functionalities on account of mixing different materials properties from their respective layers on an atomic scale. For example, Coronado *et al.*<sup>30</sup> synthesized heterostructures whereby superconductivity coexists with ferromagnetism. To achieve this unique blend of properties, exfoliated TMDs such as TaS<sub>2</sub> and

exfoliated layered double hydroxides such as  $\text{Ni}_{0.66}\text{Al}_{0.33}(\text{OH})_2$ , were re-stacked and co-precipitated in solution. By applying similar techniques to exfoliated TTMC nanosheets, a great number of new heterolayered TTMCs could be fabricated. Because TTMCs are more robust superconductors compared to TMDs, by stacking them with insulating or magnetic layers, enhanced or magnetic superconductivity could be fabricated by design.

Can the techniques used for TMD heterolayers be applied to TTMCs? Indeed, as discussed in the previous section, bulk heterolayered TTMCs such as Na-tochilinite,  $[(\text{Na}_{1-x}\text{Fe}_x)(\text{OH})_2]\text{FeS}$ , have already been prepared. This Na-tochilinite is metastable and can only be synthesized using a lower temperature route such as hydrothermal synthesis.<sup>142</sup> Finding which specific heterostructures can be synthesized and the conditions under which one achieves either a commensurate or incommensurate structure would be a worthwhile endeavor for materials chemists.

To promote TTMC materials by design, more binary hosts such as FeSe need to be synthesized. The recent discovery of two new anti-PbO type compounds, CoSe and CoS, expands the possibility for new families of intercalated TTMCs.<sup>206</sup> For example, Zhou *et al.* reported a Li-EDA intercalated CoSe, the first new TTMC using CoSe as a host, which was prepared from  $\text{KCo}_2\text{Se}_2$ , a weak itinerant ferromagnet. Even though metastable, CoSe and CoS could be hosts for further intercalation chemistry. This multi-step process in synthesizing Li-EDA-CoSe shows that novel TTMCs with targeted properties could be designed on account of their available chemistry.

## 7.2.4 Pressure Studies

High-pressure techniques may also be applied to TTMCs in two directions: 1) new emergent properties of metastable compounds under pressure and 2) synthesis of novel structures with assistance of pressure.

Pressure has long been used to improve the  $T_c$  of superconductors. For FeSe, its  $T_c$  can be enhanced to 37 K from 8 K by applying a high external pressure.<sup>19</sup> I have been curious about how the physical properties and crystal structures would evolve if pressure is applied to the novel metastable layered chalcogenides. A more intriguing question is how would a heterolayered structure, such as  $[(\text{Na}_{1-x}\text{Fe}_x)(\text{OH})_2]\text{FeS}$ , behave under pressure. An earlier work reported that FeS started to irreversibly transform to a hexagonal structure at 0.4 GPa, and then to an orthorhombic structure at 4.6 GPa.<sup>207</sup> Such structural reconfiguration requires interactions between two adjacent FeS layers. Will the hydroxide layers prevent such transition, or interact with the FeS layers to form a new structure, or both types of layers undergo separate transitions to form a new heterolayered structure?

In addition to observing changes of known compounds under pressure, I have been fascinated with a hypothesized idea to synthesize heterolayered compounds by design. The basic principle is to mix a precursor, which transforms to a layered structure under pressure, with an adduct together. The pressure will then be increased until the precursor compound undergoes a phase transition to the targeted structure. Subsequently, the mixture will be heated so that the adduct can intercalate into the layered structure. Thus, a new metastable layered compound is synthesized by design under pressure. Although the

idea is simple, in reality the synthetic challenge is enormous.

## Bibliography

## Bibliography

- [1] Onnes, H. K. *Commun. Phys. Lab. Univ. Leiden* **1911**, *12*, 1.
- [2] Carrasco, J. M.; Franquelo, L. G.; Bialasiewicz, J. T.; Galván, E.; Guisado, R. C. P.; Prats, M. A. M.; León, J. I.; Moreno-Alfonso, N. *IEEE T. Ind. Electron.* **2006**, *53*, 1002–1016.
- [3] Luongo, C. A. *IEEE T. Magn.* **2002**, *32*, 2214–2223.
- [4] Ribeiro, P. F.; Johnson, B. K.; Crow, M. L.; Arsoy, A.; Liu, Y. P. *IEEE* **2002**, *89*, 1744–1756.
- [5] Larbalestier, D.; Gurevich, A.; Feldmann, D. M.; Polyanskii, A. *Nature* **2001**, *414*, 368–377.
- [6] Bardeen, J.; Cooper, L. N.; Schrieffer, J. R. *Phys. Rev.* **1957**, *106*, 162.
- [7] Bednorz, J. G.; Müller, K. A. *Z. Phys. B.* **1986**, *64*, 189–193.

- [8] Kamihara, Y.; Watanabe, T.; Hirano, M.; Hosono, H. *J. Amer. Chem. Soc.* **2008**, *130*, 3296–3297.
- [9] Takahashi, H.; Igawa, K.; Arii, K.; Kamihara, Y.; Hirano, M.; Hosono, H. *Nature* **2008**, *453*, 376–378.
- [10] Ishida, K.; Nakai, Y.; Hosono, H. *J. Phys. Soc. Jpn.* **2009**, *78*, 062001–062001.
- [11] Johnston, D. C. *Adv. Phys.* **2010**, *59*, 803–1061.
- [12] Wen, H.-H.; Li, S. *Annu. Rev. Condens. Matter Phys.* **2011**, *2*, 121–140.
- [13] Hsu, F.-C.; Luo, J.-Y.; Yeh, K.-W.; Chen, T.-K.; Huang, T.-W.; Wu, P. M.; Lee, Y.-C.; Huang, Y.-L.; Chu, Y.-Y.; Yan, D.-C.; Wu, M.-K. *Proc. Natl. Acad. Sci. USA* **2008**, *105*, 14262–14264.
- [14] Kotegawa, H.; Masaki, S.; Awai, Y.; Tou, H.; Mizuguchi, Y.; Takano, Y. *J. Phys. Soc. Jpn.* **2008**, *77*, 113703.
- [15] McQueen, T. M.; Williams, A. J.; Stephens, P. W.; J., T.; Zhu, Y.; Ksenofontov, V.; Casper, F.; Felser, C.; Cava, R. J. *Phys. Rev. Lett.* **2009**, *103*, 057002.
- [16] McQueen, T. M.; Huang, Q.; Ksenofontov, V.; Felser, C.; Xu, Q.; Zandbergen, H.; Hor, Y. S.; Allred, J.; Williams, A. J.; Qu, D.; Checkelsky, J.; Ong, N. P.; Cava, R. J. *Phys. Rev. B* **2009**, *79*, 014522.
- [17] Margadonna, S.; Takabayashi, Y.; McDonald, M. T.; Kasperkiewicz, K.; Mizuguchi, Y.; Takano, Y.; Fitch, A. N.; Suard, E.; Prassides, K. *Chem. Commun.* **2008**, 5607–5609.

- [18] Imai, T.; Ahilan, K.; Ning, F. L.; McQueen, T. M.; Cava, R. J. *Phys. Rev. Lett.* **2009**, *102*, 177005.
- [19] Medvedev, S.; McQueen, T. M.; Troyan, I. A.; Palasyuk, T.; Eremets, M. I.; Cava, R. J.; Naghavi, S.; Casper, F.; Ksenofontov, V.; Wortmann, G.; Felser, C. *Nat. Mater.* **2009**, *8*, 630–633.
- [20] Burrard-Lucas, M.; Free, D. G.; Sedlmaier, S. J.; Wright, J. D.; Cassidy, S. J.; Hara, Y.; Corkett, A. J.; Lancaster, T.; Baker, P. J.; Blundell, S. J.; Clarke, S. J. *Nat. Mater.* **2013**, *12*, 15–19.
- [21] Guo, J.; Jin, S.; Wang, G.; Wang, S.; Zhu, K.; Zhou, T.; He, M.; Chen, X. *Phys. Rev. B* **2010**, *82*, 180520.
- [22] Ying, T. P.; Chen, X. L.; Wang, G.; Jin, S. F.; Zhou, T. T.; Lai, X. F.; Zhang, H.; Wang, W. Y. *Sci. Rep.* **2012**, *2*, 426.
- [23] Sedlmaier, S. J.; Cassidy, S. J.; Morris, R. G.; Drakopoulos, M.; Reinhard, C.; Moorhouse, S. J.; O'Hare, D.; Manuel, P.; Khalyavin, D.; Clarke, S. J. *J. Amer. Chem. Soc.* **2014**, *136*, 630–633.
- [24] Lu, X. F.; Wang, N. Z.; Zhang, G. H.; Luo, X. G.; Ma, Z. M.; Lei, B.; Huang, F. Q.; Chen, X. H. *Phys. Rev. B* **2014**, *89*, 020507.
- [25] Pachmayr, U.; Nitsche, F.; Luetkens, H.; Kamusella, S.; Brückner, F.; Sarkar, R.; Klauss, H.-H.; Johrendt, D. *Angew. Chem. Int. Ed.* **2015**, *54*, 293–297.
- [26] Sun, H. et al. *Inorg. Chem.* **2015**, *54*, 1958–1964.

- [27] Ge, J.-F.; Liu, Z.-L.; Liu, C.; Gao, C.-L.; Qian, D.; Xue, Q.-K.; Liu, Y.; Jia, J.-F. *Nat. Mater.* **2015**, *14*, 285–289.
- [28] Tan, S. et al. *Nat. Mater.* **2013**, *12*, 634–640.
- [29] Liu, D.; Zhang, W.; Mou, D.; He, J.; Ou, Y.-B.; Wang, Q.-Y.; Li, Z.; Wang, L.; Zhao, L.; He, S. *Nat. Commun.* **2012**, *3*, 931.
- [30] Coronado, E.; Martí-Gastaldo, C.; Navarro-Moratalla, E.; Ribera, A.; Blundell, S. J.; Baker, P. J. *Nat. Chem.* **2010**, *2*, 1031–1036.
- [31] Dresselhaus, M. S.; Dresselhaus, G. *Adv. Phys.* **2002**, *51*, 1–186.
- [32] Usuki, A.; Kawasumi, M.; Kojima, Y.; Okada, A.; Kurauchi, T.; Kamigaito, O. *J. Mater. Res.* **1993**, *8*, 1174–1178.
- [33] Whittingham, M. S. *Science* **1976**, *192*, 1126–1127.
- [34] Gamble, F. R.; DiSalvo, F. J.; Klemm, R. A.; Geballe, T. H. *Science* **1970**, *168*, 568–570.
- [35] Gamble, F. R.; Osiecki, J. H.; Cais, M.; Pisharody, R.; DiSalvo, F. J.; Geballe, T. H. *Science* **1971**, *174*, 493–497.
- [36] Geballe, T. H.; Menth, A.; Di Salvo, F. J.; Gamble, F. R. *Phys. Rev. Lett.* **1971**, *27*, 314–316.
- [37] Murphy, D. W.; Di Salvo, F. J.; Hull, G. W.; Waszczak, J. V.; Meyer, S. F.; Stewart, G. R.; Early, S.; Acrivos, J. V.; Geballe, T. H. *J. Chem. Phys.* **1975**, *62*.

- [38] Shoemaker, D. P.; Chung, D. Y.; Claus, H.; Francisco, M. C.; Avci, S.; Llobet, A.; Kanatzidis, M. G. *Phys. Rev. B* **2012**, *86*, 184511.
- [39] Bacsa, J.; Ganin, A.; Takabayashi, Y.; Christensen, K.; Prassides, K.; Rosseinsky, M.; Claridge, J. *Chem. Sci.* **2011**, *2*, 1054–1058.
- [40] Ying, T.; Chen, X.; Wang, G.; Jin, S.; Lai, X.; Zhou, T.; Zhang, H.; Shen, S.; Wang, W. *J. Amer. Chem. Soc.* **2013**, *135*, 2951–2954.
- [41] Zheng, L.; Izumi, M.; Sakai, Y.; Eguchi, R.; Goto, H.; Takabayashi, Y.; Kambe, T.; Onji, T.; Araki, S.; Kobayashi, T. C.; Kim, J.; Fujiwara, A.; Kubozono, Y. *Phys. Rev. B* **2013**, *88*, 094521.
- [42] Foronda, F. R.; Ghannadzadeh, S.; Sedlmaier, S. J.; Wright, J. D.; Burns, K.; Cassidy, S. J.; Goddard, P. A.; Lancaster, T.; Clarke, S. J.; Blundell, S. J. *Phys. Rev. B* **2015**, *92*, 134517.
- [43] Hayashi, F.; Lei, H.; Guo, J.; Hosono, H. *Inorg. Chem.* **2015**, *54*, 3346–3351.
- [44] Yusenko, K.; Sottmann, J.; Emerich, H.; Crichton, W.; Malavasi, L.; Margadonna, S. *Chem. Commun.* **2015**, *51*, 7112–7115.
- [45] Hatakeda, T.; Noji, T.; Kawamata, T.; Kato, M.; Koike, Y. *J. Phys. Soc. Jpn.* **2013**, *82*, 123705.
- [46] Hosono, S.; Noji, T.; Hatakeda, T.; Kawamata, T.; Kato, M.; Koike, Y. *J. Phys. Soc. Jpn.* **2014**, *83*, 113704.

- [47] Krzton-Maziopa, A.; Pomjakushina, E.; Pomjakushin, V. Y.; Von Rohr, F.; Schilling, A.; Conder, K. *J. Phys. Condens. Matter* **2012**, *24*, 382202.
- [48] Jin, S.; Wu, X.; Huang, Q.; Wu, H.; Ying, T.; Fan, X.; Sun, R.; Zhao, L.; Chen, X. *arXiv preprint arXiv:1607.01103* **2016**,
- [49] Hosono, S.; Noji, T.; Hatakeda, T.; Kawamata, T.; Kato, M.; Koike, Y. *J. Phys. Soc. Jpn.* **2015**, *85*, 013702.
- [50] Vivanco, H. K.; Rodriguez, E. E. *J. Solid State Chem.* **2016**, *242*, 3–21.
- [51] Génin, J.-M. R.; Bourrié, G.; Trolard, F.; Abdelmoula, M.; Jaffrezic, A.; Refait, P.; Maitre, V.; Humbert, B.; Herbillon, A. *Environ. Sci. Technol.* **1998**, *32*, 1058–1068.
- [52] Lu, X. F.; Wang, N. Z.; Wu, H.; Wu, Y. P.; Zhao, D.; Zeng, X. Z.; Luo, X. G.; Wu, T.; Bao, W.; Zhang, G. H.; Huang, F. Q.; Huang, Q. Z.; Chen, X. H. *Nat. Mater.* **2015**, *14*, 325–329.
- [53] Zhou, X.; Borg, C. K. H.; Lynn, J. W.; Saha, S. R.; Paglione, J.; Rodriguez, E. E. *J. Mater. Chem. C* **2016**, *4*, 3934–3941.
- [54] Lynn, J. W.; Zhou, X.; Borg, C. K. H.; Saha, S. R.; Paglione, J.; Rodriguez, E. E. *Phys. Rev. B* **2015**, *92*, 060510.
- [55] Woodruff, D. N.; Schild, F.; Topping, C. V.; Cassidy, S. J.; Blandy, J. N.; Blundell, S. J.; Thompson, A. L.; Clarke, S. J. *Inorg. Chem.* **2016**, *55*, 9886–9891.
- [56] Topping, C.; Kirschner, F.; Blundell, S.; Baker, P.; Woodruff, D.; Schild, F.; Sun, H.; Clarke, S. *arXiv preprint arXiv:1704.01492* **2017**,

- [57] Guo, Z.; Zhou, L.; Jin, S.; Han, B.; Sun, F.; Yuan, W. *RSC Adv.* **2017**, *7*, 17539–17544.
- [58] Lu, X. F.; Wang, N. Z.; Luo, X. G.; Zhang, G. H.; Gong, X. L.; Huang, F. Q.; Chen, X. H. *Phys. Rev. B* **2014**, *90*, 214520.
- [59] Pachmayr, U.; Johrendt, D. *Chem. Commun.* **2015**, *51*, 4689–4692.
- [60] Zhang, X.; Lai, X.; Yi, N.; He, J.; Chen, H.; Zhang, H.; Lin, J.; Huang, F. *RSC Adv.* **2015**, *5*, 38248–38253.
- [61] Rodriguez, E. E.; Zavalij, P.; Hsieh, P.-Y.; Green, M. A. *J. Amer. Chem. Soc.* **2010**, *132*, 10006–10008.
- [62] Rodriguez, E. E.; Stock, C.; Zajdel, P.; Krycka, K. L.; Majkrzak, C. F.; Zavalij, P.; Green, M. A. *Phys. Rev. B* **2011**, *84*, 064403.
- [63] Lai, X.; Zhang, H.; Wang, Y.; Wang, X.; Zhang, X.; Lin, J.; Huang, F. *J. Amer. Chem. Soc.* **2015**, *137*, 10148–10151.
- [64] Ambasta, B. *Chemistry for engineers*; Laxmi Publications, 2008.
- [65] Bonomi, F.; Werth, M. T.; Kurtz Jr, D. M. *Inorg. Chem.* **1985**, *24*, 4331–4335.
- [66] Cheary, R. W.; Coelho, A. *J. Appl. Crystallogr.* **1992**, *25*, 109–121.
- [67] others., et al. *J. Res. NIST* **2012**, *117*, 61.
- [68] Smith, T. F.; Chu, C. W. *Phys. Rev.* **1967**, *159*, 353–358.

- [69] Physical Property Measurement System Heat Capacity Option User's Manual. Quantum Design: 11578 Sorrento Valley Rd., San Diego, CA 92121-1311 USA, 2004.
- [70] Hwang, J. S.; Lin, K. J.; Tien, C. *Rev. Sci. Instrum.* **1997**, *68*, 94–101.
- [71] Bachmann, R.; DiSalvo, F. J.; Geballe, T. H.; Greene, R. L.; Howard, R. E.; King, C. N.; Kirsch, H. C.; Lee, K. N.; Schwall, R. E.; Thomas, H.; Zubeck, R. B. *Rev. Sci. Instrum.* **1972**, *43*, 205–214.
- [72] Hohenberg, P.; Kohn, W. *Phys. Rev.* **1964**, *136*, B864–B871.
- [73] Kohn, W.; Sham, L. J. *Phys. Rev.* **1965**, *137*, A1697–A1705.
- [74] Kresse, G. Title. Ph.D. thesis, Technische Universität Wien, 1993.
- [75] Kresse, G.; Hafner, J. *Phys. Rev. B* **1993**, *47*, 558–561.
- [76] Kresse, G.; Furthmüller, J. *Comput. Mater. Sci.* **1996**, *6*, 15 – 50.
- [77] Kresse, G.; Furthmüller, J. *Phys. Rev. B* **1996**, *54*, 11169–11186.
- [78] Blöchl, P. E. *Phys. Rev. B* **1994**, *50*, 17953–17979.
- [79] Perdew, J. P.; Burke, K.; Ernzerhof, M. *Phys. Rev. Lett.* **1996**, *77*, 3865–3868.
- [80] Monkhorst, H. J.; Pack, J. D. *Phys. Rev. B* **1976**, *13*, 5188–5192.
- [81] Dronskowski, R.; Bloechl, P. E. *J. Phys. Chem. A* **1993**, *97*, 8617–8624.
- [82] Deringer, V. L.; TchougrÃeff, A. L.; Dronskowski, R. *J. Phys. Chem. A* **2011**, *115*, 5461–5466.

- [83] Maintz, S.; Deringer, V. L.; Tchougréeff, A. L.; Dronskowski, R. *J. Comput. Chem.* **2013**, *34*, 2557–2567.
- [84] Maintz, S.; Deringer, V. L.; Tchougréeff, A. L.; Dronskowski, R. *J. Comput. Chem.* **2016**, *37*, 1030–1035.
- [85] Paglione, J.; Greene, R. L. *Nat. Phys.* **2010**, *6*, 645–658.
- [86] Ivanovskii, A. *Physica C* **2011**, *471*, 409–427.
- [87] Takahashi, H. et al. *Nat. Mater.* **2015**, *14*, 1008–1012.
- [88] Drozdov, A. P.; Eremets, M. I.; Troyan, I. A.; Ksenofontov, V.; Shylin, S. I. *Nature* **2015**, *525*, 73–76.
- [89] Kouvo, O.; Long, J.; Vuorelainen, Y. *Am. Mineral.* **1963**, *48*, 511.
- [90] Bertaut, E.; Burlet, P.; Chappert, J. *Solid State Commun.* **1965**, *3*, 335 – 338.
- [91] Evans Jr, H. T.; Milton, C.; Chao, E.; Adler, I.; Mead, C.; Ingram, B.; Berner, R. A. *US Geol. Survey Prof. Paper* **1964**, *475*, 1312 – 1318.
- [92] Lennie, A.; Redfern, S.; Schofield, P.; Vaughan, D. *Mineral. Mag.* **1995**, *59*, 677–684.
- [93] Rickard, D.; Luther, G. W. *Chem. Rev.* **2007**, *107*, 514–562.
- [94] Denholme, S. J.; Demura, S.; Okazaki, H.; Hara, H.; Deguchi, K.; Fujioka, M.; Ozaki, T.; Yamaguchi, T.; Takeya, H.; Takano, Y. *Mater. Chem. Phys.* **2014**, *147*, 50–56.

- [95] Sines, I. T.; Vaughn II, D. D.; Misra, R.; Popczun, E. J.; Schaak, R. E. *J. Solid State Chem.* **2012**, *196*, 17–20.
- [96] Dutta, A. K.; Maji, S. K.; Srivastava, D. N.; Mondal, A.; Biswas, P.; Paul, P.; Adhikary, B. *ACS Appl. Mater. & Interfaces* **2012**, *4*, 1919–1927, PMID: 22448782.
- [97] Lennie, A. R.; England, K. E.; Vaughan, D. J. *Am. Mineral.* **1995**, *80*, 960–967.
- [98] Csakberenyi-Malasics, D.; Rodriguez-Blanco, J. D.; Kis, V. K.; Recnik, A.; Benning, L. G.; Posfai, M. *Chem. Geol.* **2012**, *294 - 295*, 249 – 258.
- [99] Bao, W.; Qui, Y.; Huang, Q.; Zajdel, M. A. G. a. P.; Fitzsimmons, M. R.; Zherenkov, M.; Chang, S.; Fang, M.; Qian, B.; Vehstedt, E. K.; Yang, J.; Pham, H. M.; Spinu, L.; Mao, Z. Q. *Phys. Rev. Lett.* **2009**, *102*, 247001.
- [100] Liu, T. J. et al. *Nat. Mater.* **2010**, *9*, 716–720.
- [101] Bhatia, V.; Rodriguez, E. E.; Butch, N. P.; Paglione, J.; Green, M. A. *Chem. Comm.* **2011**, *47*, 11297.
- [102] Rodriguez, E. E.; Stock, C.; Zajdel, P.; Krycka, K. L.; Majkrzak, C. F.; Zavalij, P.; Green, M. A. *Phys. Rev. B* **2011**, *84*, 064403.
- [103] Stock, C.; Rodriguez, E. E.; Green, M.; Zavalij, P.; Rodriguez-Rivera, J. *Phys. Rev. B* **2011**, *84*, 045124.
- [104] Hara, Y.; Takase, K.; Yamasaki, A.; Sato, H.; Miyakawa, N.; Umeyama, N.; Ikeda, S. I. *Physica C* **2010**, *470, Supplement 1*, S313–S314.

- [105] Böhmer, A. E.; Arai, T.; Hardy, F.; Hattori, T.; Iye, T.; Wolf, T.; Löhneysen, H. v.; Ishida, K.; Meingast, C. *Phys. Rev. Lett.* **2015**, *114*, 027001.
- [106] Hu, R.; Cho, K.; Kim, H.; Hodovanets, H.; Straszheim, W. E.; Tanatar, M. A.; Prozorov, R.; Bud'ko, S. L.; Canfield, P. C. *Supercond. Sci. Tech.* **2011**, *24*, 065006.
- [107] Luo, X. G.; Wang, X. F.; Ying, J. J.; Yan, Y. J.; Li, Z. Y.; Zhang, M.; Wang, A. F.; Cheng, P.; Xiang, Z. J.; Ye, G. J.; Liu, R. H.; Chen, X. H. *New J. Phys.* **2011**, *13*, 053011.
- [108] Lei, H.; Abeykoon, M.; Bozin, E. S.; Petrovic, C. *Phys. Rev. B* **2011**, *83*, 180503.
- [109] Lei, H.; Abeykoon, M.; Bozin, E. S.; Wang, K.; Warren, J. B.; Petrovic, C. *Phys. Rev. Lett.* **2011**, *107*, 137002.
- [110] Neilson, J. R.; McQueen, T. M. *J. Amer. Chem. Soc.* **2012**, *134*, 7750–7757.
- [111] Dong, X.; Jin, K.; Yuan, D.; Zhou, H.; Yuan, J.; Huang, Y.; Hua, W.; Sun, J.; Zheng, P.; Hu, W.; Mao, Y.; Ma, M.; Zhang, G.; Zhou, F.; Zhao, Z. *Phys. Rev. B* **2015**, *92*, 064515.
- [112] Margadonna, S.; Takabayashi, Y.; Ohishi, Y.; Mizuguchi, Y.; Takano, Y.; Kagayama, T.; Nakagawa, T.; Takata, M.; Prassides, K. *Phys. Rev. B* **2009**, *80*, 064506.
- [113] Rodriguez, E. E.; Sokolov, D. A.; Stock, C.; Green, M. A.; Sobolev, O.; Rodriguez-Rivera, J. A.; Cao, H.; Daoud-Aladine, A. *Phys. Rev. B* **2013**, *88*, 165110.

- [114] Lennie, A. R.; Redfern, S. A. T.; Champness, P. E.; Stoddart, C. P.; Schofield, P. F.; Vaughan, D. J. *Am. Mineral.* **1997**, *82*, 302–309.
- [115] Werthamer, N. R.; Helfand, E.; Hohenberg, P. C. *Phys. Rev.* **1966**, *147*, 295–302.
- [116] Tinkham, M. *Phys. Rev.* **1963**, *129*, 2413–2422.
- [117] Ketterson, J.; Song, S. *Superconductivity*; Cambridge University Press, 40 West 20th Street, New York, NY 10011-4211, USA, 1999; pp 45–46.
- [118] Hu, R.; Bozin, E. S.; Warren, J. B.; Petrovic, C. *Phys. Rev. B* **2009**, *80*, 214514.
- [119] Abdel-Hafez, M.; Zhang, Y.-Y.; Cao, Z.-Y.; Duan, C.-G.; Karapetrov, G.; Pudalov, V. M.; Vlasenko, V. A.; Sadakov, A. V.; Knyazev, D. A.; Romanova, T. A.; Chareev, D. A.; Volkova, O. S.; Vasiliev, A. N.; Chen, X.-J. *Phys. Rev. B* **2015**, *91*, 165109.
- [120] Millis, A. J.; Sachdev, S.; Varma, C. M. *Phys. Rev. B.* **1988**, *37*, 4795.
- [121] Vaughan, D. J.; Ridout, M. S. *J. Inorg. Nucl. Chem.* **1971**, *33*, 741–746.
- [122] Subedi, A.; Zhang, L.; Singh, D. J.; Du, M. H. *Phys. Rev. B* **2008**, *78*, 134514.
- [123] Kwon, K. D.; Refson, K.; Bone, S.; Qiao, R.; Yang, W.-l.; Liu, Z.; Sposito, G. *Phys. Rev. B* **2011**, *83*, 064402.
- [124] Devey, A. J.; Grau-Crespo, R.; de Leeuw, N. H. *J. Phys. Chem. C* **2008**, *112*, 10960–10967.
- [125] Brgoch, J.; Miller, G. J. *J. Phys. Chem. A* **2012**, *116*, 2234–2243.

- [126] Greenfield, J. T.; Kamali, S.; Lee, K.; Kovnir, K. *Chem. Mater.* **2015**, *27*, 588–596.
- [127] Lee, C.; Kihou, K.; Iyo, A.; Kito, H.; Shirage, P.; Eisaki, H. *Solid State Commun.* **2012**, *152*, 644 – 648, Special Issue on Iron-based Superconductors.
- [128] Mizuguchi, Y.; Hara, Y.; Deguchi, K.; Tsuda, S.; Yamaguchi, T.; Takeda, K.; Kote-gawa, H.; Tou, H.; Takano, Y. *Supercond. Sci. Tech.* **2010**, *23*, 054013.
- [129] Imai, T.; Ahilan, K.; Ning, F. L.; McQueen, T. M.; Cava, R. J. *Phys. Rev. Lett.* **2009**, *102*, 177005.
- [130] Mizuguchi, Y.; Tomioka, F.; Tsuda, S.; Yamaguchi, T.; Takano, Y. *Appl. Phys. Lett.* **2009**, *94*, 012503.
- [131] Zajdel, P.; Hsieh, P.-Y.; Rodriguez, E. E.; Butch, N. P.; Magill, J. D.; Paglione, J.; Zavalij, P.; Suchomel, M. R.; Green, M. A. *J. Amer. Chem. Soc.* **2010**, *132*, 13000–13007.
- [132] de Pablo, J. J.; Jones, B.; Kovacs, C. L.; Ozolins, V.; Ramirez, A. P. *Curr. Opin. Solid State Mater. Sci.* **2014**, *18*, 99 – 117.
- [133] Jain, A.; Persson, K. A.; Ceder, G. *APL Mater.* **2016**, *4*.
- [134] Schaak, R. E.; Mallouk, T. E. *Chem. Mater.* **2002**, *14*, 1455–1471.
- [135] Tsujimoto, Y.; Tassel, C.; Hayashi, N.; Watanabe, T.; Kageyama, H.; Yoshimura, K.; Takano, M.; Ceretti, M.; Ritter, C.; Paulus, W. *Nature* **2007**, *450*, 1062–1065.

- [136] Tassel, C.; Miguel Pruneda, J.; Hayashi, N.; Watanabe, T.; Kitada, A.; Tsujimoto, Y.; Kageyama, H.; Yoshimura, K.; Takano, M.; Nishi, M.; Ohoyama, K.; Mizumaki, M.; Kawamura, N.; Iniguez, J.; Canadell, E. *J. Am. Chem. Soc.* **2009**, *131*, 221–229.
- [137] Yajima, T.; Kitada, A.; Kobayashi, Y.; Sakaguchi, T.; Bouilly, G.; Kasahara, S.; Terashima, T.; Takano, M.; Kageyama, H. *J. Am. Chem. Soc.* **2012**, *134*, 8782–8785.
- [138] Huan, G.; Greenblatt, M.; Croft, M. *Eur. J. Solid State Inorg. Chem.* **1989**, *26*, 193–220.
- [139] Oledzka, M.; Lee, J.-G.; Ramanujachary, K.; Greenblatt, M. *J. Solid State Chem.* **1996**, *127*, 151 – 160.
- [140] Oledzka, M.; Ramanujachary, K.; Greenblatt, M. *Mater. Res. Bull.* **1998**, *33*, 855 – 866.
- [141] Borg, C. K. H.; Zhou, X.; Eckberg, C.; Campbell, D. J.; Saha, S. R.; Paglione, J.; Rodriguez, E. E. *Phys. Rev. B* **2016**, *93*, 094522.
- [142] Zhou, X.; Eckberg, C.; Wilfong, B.; Liou, S.-C.; Vivanco, H. K.; Paglione, J.; Rodriguez, E. E. *Chem. Sci.* **2017**, *8*, 3781–3788.
- [143] Kovnir, K.; Garlea, V. O.; Thompson, C. M.; Zhou, H.; Reiff, W. M.; Ozarowski, A.; Shatruk, M. *Inorg. Chem.* **2011**, *50*, 10274–10283.

- [144] Kovnir, K.; Reiff, W. M.; Menushenkov, A. P.; Yaroslavtsev, A. A.; Chernikov, R. V.; Shatruk, M. *Chem. Mater.* **2011**, *23*, 3021–3024.
- [145] Thompson, C. M.; Kovnir, K.; Garlea, V. O.; Choi, E. S.; Zhou, H. D.; Shatruk, M. *J. Mater. Chem. C* **2014**, *2*, 7561–7569.
- [146] Menushenkov, A. P.; Yaroslavtsev, A. A.; Geondzhian, A. Y.; Chernikov, R. V.; Zubavichus, Y. V.; Tan, X.; Shatruk, M. *J. Supercond. Nov. Magn.* **2015**, *28*, 995–997.
- [147] Tan, X.; Fabbris, G.; Haskel, D.; Yaroslavtsev, A. A.; Cao, H.; Thompson, C. M.; Kovnir, K.; Menushenkov, A. P.; Chernikov, R. V.; Garlea, V. O.; Shatruk, M. *J. Am. Chem. Soc.* **2016**, *138*, 2724–2731.
- [148] Hoffmann, R.; Zheng, C. *J. Phys. Chem. A* **1985**, *89*, 4175–4181.
- [149] Hoffmann, R. *Angew. Chem. Int. Ed.* **1987**, *26*, 846–878.
- [150] Komarek, K. L.; Wessely, K. *Monatsh. Chem.* **1972**, *103*, 896–906.
- [151] Bøhm, F.; Grøvdold, F.; Haraldsen, H.; Pyrdz, H. *Acta Chem. Scand.* **1955**, *9*.
- [152] Yang, J.; Chen, B.; Wang, H.; Mao, Q.; Imai, M.; Yoshimura, K.; Fang, M. *Phys. Rev. B* **2013**, *88*, 064406.
- [153] Jeitschko, W.; Meisen, U.; Mäüller, M. H.; Reehuis, M. *Z. Anorg. Allg. Chem.* **1985**, *527*, 73–84.
- [154] Kaul, S. N. *J. Phys.: Condens. Matter* **1999**, *11*, 7597.

- [155] Motohashi, T.; Ono, T.; Sugimoto, Y.; Masubuchi, Y.; Kikkawa, S.; Kanno, R.; Karppinen, M.; Yamauchi, H. *Phys. Rev. B* **2009**, *80*, 165114.
- [156] Moriya, T. *J. Magn. Magn. Mater.* **1979**, *14*, 1 – 46.
- [157] Ueda, K.; Moriya, T. *J. Phys. Soc. Jpn.* **1975**, *39*, 605–615.
- [158] Stoner, E. C. *Proc. R. Soc. London, Ser. A* **1938**, *165*, 372–414.
- [159] Ding, Y.; Wang, Y.; Ni, J. *Solid State Commun.* **2009**, *149*, 505–509.
- [160] Scheidt, E.-W.; Hathwar, V.; Schmitz, D.; Dunbar, A.; Scherer, W.; Mayr, F.; Tsurkan, V.; Deisenhofer, J.; Loidl, A. *Eur. Phys. J. B* **2012**, *85*.
- [161] He, S. et al. *Nat. Mater.* **2013**, *12*, 605–610.
- [162] Lu, X. F.; Wang, N. Z.; Luo, X. G.; Zhang, G. H.; Gong, X. L.; Huang, F. Q.; Chen, X. H. *Phys. Rev. B* **2014**, *90*, 214520.
- [163] Dong, X.; Zhou, H.; Yang, H.; Yuan, J.; Jin, K.; Zhou, F.; Yuan, D.; Wei, L.; Li, J.; Wang, X.; Zhang, G.; Zhao, Z. *J. Amer. Chem. Soc.* **2015**, *137*, 66–69.
- [164] others., et al. *Phys. Rev. B* **2011**, *83*, 212502.
- [165] Harrison, P. G. *Chemistry of tin*; Blackie. Chapman and Hall, 1989.
- [166] de La Cruz, C.; Huang, Q.; Lynn, J. W.; Li, J.; Ratcliff, W.; Zarestky, J. L.; Mook, H. A.; Chen, G. F.; Luo, J. L.; Want, N. L.; Dai, P. *Nature* **2008**, *453*, 899.

- [167] Chen, X. H.; Wu, T.; Wu, G.; Liu, R. H.; Chen, H.; Fang, D. F. *Nature* **2008**, *435*, 761–762.
- [168] Walz, F. *J. Phys.: Condens. Matter* **2002**, *14*, R285.
- [169] Zhang, Z.; Satpathy, S. *Phys. Rev. B* **1991**, *44*, 13319.
- [170] others., et al. *J. Solid State Chem.* **1998**, *141*, 554–561.
- [171] Tabuchi, M.; Tsutsui, S.; Masquelier, C.; Kanno, R.; Ado, K.; Matsubara, I.; Nasu, S.; Kageyama, H. *J. Solid State Chem.* **1998**, *140*, 159–167.
- [172] Mizuguchi, Y.; Takano, Y. *Journal of the Physical Society of Japan* **2010**, *79*, 102001.
- [173] Wei, B.; Qing-Zhen, H.; Gen-Fu, C.; Green, M.; Du-Ming, W.; Jun-Bao, H.; Yi-Ming, Q. *Chin. Phys. Lett.* **2011**, *28*, 086104.
- [174] Wang, H.-D.; Dong, C.-H.; Li, Z.-J.; Mao, Q.-H.; Zhu, S.-S.; Feng, C.-M.; Yuan, H.; Fang, M.-H. *Eur. Phys. Lett.* **2011**, *93*, 47004.
- [175] Fang, M.-H.; Wang, H.-D.; Dong, C.-H.; Li, Z.-J.; Feng, C.-M.; Chen, J.; Yuan, H. *Eur. Phys. Lett.* **2011**, *94*, 27009.
- [176] others., et al. *Phys. Rev. B* **2011**, *83*, 060512.
- [177] Pomjakushin, V. Y.; Sheptyakov, D.; Pomjakushina, E.; Krzton-Maziopa, A.; Conder, K.; Chernyshov, D.; Svitlyk, V.; Shermadini, Z. *Physical Review B* **2011**, *83*, 144410.

- [178] Wang, D.; He, J.; Xia, T.-L.; Chen, G. *Phys. Rev.B* **2011**, *83*, 132502.
- [179] others., et al. *Phys. Rev. B* **2011**, *83*, 132509.
- [180] Ding, X.; Fang, D.; Wang, Z.; Yang, H.; Liu, J.; Deng, Q.; Ma, G.; Meng, C.; Hu, Y.; Wen, H.-H. *Nat. Commun.* **2013**, *4*, 1897.
- [181] Guterding, D.; Jeschke, H. O.; Hirschfeld, P.; Valentí, R. *Phys.Rev.B* **2015**, *91*, 041112.
- [182] Bos, J.; Penny, G.; Rodgers, J.; Sokolov, D.; Huxley, A.; Attfield, J. P. *Chem. Commun.* **2008**, 3634–3635.
- [183] Luetkens, H. et al. *Nat. Mater.* **2009**, *8*, 305.
- [184] Hanaguri, T.; Niitaka, S.; Kuroki, K.; Takagi, H. *Science* **2010**, *328*, 474–476.
- [185] Attfield, J. P. *J. Mater. Chem.* **2011**, *21*, 4756–4764.
- [186] Ozawa, T. C.; Kauzlarich, S. M. *Sci. Tech. Adv. Mater.* **2008**, *9*, 033003.
- [187] Kittel, C. *Introduction to Solid State Physics*, 8th ed.; Wiley, 2005.
- [188] Levin, K.; Kim, J. H.; Lu, J.; Si, Q. *Physica C: Supercond.* **1991**, *175*, 449 – 522.
- [189] Manako, T.; Kubo, Y.; Shimakawa, Y. *Phys. Rev. B* **1992**, *46*, 11019–11024.
- [190] Cooper, R. A.; Wang, Y.; Vignolle, B.; Lipscombe, O. J.; Hayden, S. M.; Tanabe, Y.; Adachi, T.; Koike, Y.; Nohara, M.; Takagi, H.; Proust, C.; Hussey, N. E. *Science* **2009**, *323*, 603–607.

- [191] Yonezawa, S.; Maeno, Y. *Phys. Rev. B* **2013**, *88*, 205143.
- [192] Organova, N.; Drits, V.; Dmitrik, A. *Sov. Phys., Crystallogr.* **1972**, *17*, 667.
- [193] Pekov, I. V.; Sereda, E. V.; Polekhovsky, Y. S.; Britvin, S. N.; Chukanov, N. V.; Yapaskurt, V. O.; Bryzgalov, I. A. *Geol. Ore Deposits* **2013**, *55*, 567–574.
- [194] Parise, J. B.; Marshall, W. G.; Smith, R. I.; Lutz, H. D.; Möller, H. *Am. Mineral.* **2000**, *85*, 189–193.
- [195] Peng, Y.; Xi, G.; Zhong, C.; Wang, L.; Lu, J.; Sun, X.; Zhu, L.; Han, Q.; Chen, L.; Shi, L.; Sun, M.; Li, Q.; Yu, M.; Yin, M. *Geochim. Cosmochim. Acta* **2009**, *73*, 4862 – 4878.
- [196] Zhou, X.; Rodriguez, E. E. *Chem. Mater.* **2017**, *29*, 5737–5752.
- [197] Luo, T.; Chen, L.; Bao, K.; Yu, W.; Qian, Y. *Carbon* **2006**, *44*, 2844–2848.
- [198] Li, H.; Yin, Z.; He, Q.; Li, H.; Huang, X.; Lu, G.; Fam, D. W. H.; Tok, A. I. Y.; Zhang, Q.; Zhang, H. *Small* **2012**, *8*, 63–67.
- [199] Wang, Q. H.; Kalantar-Zadeh, K.; Kis, A.; Coleman, J. N.; Strano, M. S. *Nat. Nanotechnol.* **2012**, *7*, 699–712.
- [200] Coleman, J. N. et al. *Science* **2011**, *331*, 568–571.
- [201] Zeng, Z.; Sun, T.; Zhu, J.; Huang, X.; Yin, Z.; Lu, G.; Fan, Z.; Yan, Q.; Hng, H. H.; Zhang, H. *Angew. Chem. Int. Ed.* **2012**, *51*, 9052–9056.

- [202] Zhao, W.; Ghorannevis, Z.; Chu, L.; Toh, M.; Kloc, C.; Tan, P.; Eda, G. *ACS Nano* **2013**, *7*, 791–797.
- [203] Splendiani, A.; Sun, L.; Zhang, Y.; Li, T.; Kim, J.; Chim, C.-Y.; Galli, G.; Wang, F. *Nano Lett.* **2010**, *10*, 1271–1275.
- [204] Wang, Q.-Y. et al. *Chin. Phys. Lett.* **2012**, *29*, 037402.
- [205] Heising, J.; Kanatzidis, M. G. *J. Amer. Chem. Soc.* **1999**, *121*, 638–643.
- [206] Zhou, X.; Wilfong, B.; Vivanco, H.; Paglione, J.; Brown, C. M.; Rodriguez, E. E. *J. Amer. Chem. Soc.* **2016**, *138*, 16432–16442.
- [207] Lai, X.; Liu, Y.; Lü, X.; Zhang, S.; Bu, K.; Jin, C.; Zhang, H.; Lin, J.; Huang, F. *Sci. Rep.* **2016**, *6*, 31077.